Development of a Tunable Electromechanical Acoustic Liner for Engine Nacelles

Final Report

NASA-LaRC Grant # NNL04AA13A

(March 4, 2004 – February 28, 2007)

Michael G. Jones
Mail Stop 463, 2 North Dryden Street
NASA Langley Research Center
Hampton, VA 23681-2199
Building 1208, Room 203
Structural Acoustics Branch
Fluid Mechanics and Acoustics Division

Prepared by:

Fei Liu
Mark Sheplak
Louis N. Cattafesta III

Interdisciplinary Microsystems Group
Department of Mechanical and Aerospace Engineering
University of Florida
P.O. Box 116250
231 MAE-A Building
Gainesville, FL 32611-6250
sheplak@ ufl.edu
(352) 392-3983
(352) 392-7303 fax

TABLE OF CONTENTS

LIST OF APPENDICES

Appendix A. Parameters Estimation for LEM of the Piezoelectric Composite Diaphragm

Appendix B. Capacitive and Inductive-Tuning Strategy of the EMHR

Appendix C. Development of Transfer Matrix of the EMHR

Appendix D. Comparison Between TM and LEM

Appendix E. Summary on NASA 2DOF Liner Mimic

Appendix F. Impedance Prediction Code – ZKTL

LIST OF FIGURES

LIST OF TABLES

1 Executive Summary

This report describes the development of a tunable electromechanical Helmholtz resonator (EMHR) for engine nacelles using smart materials technology. This effort addresses both near-term and long-term goals for tunable electromechanical acoustic liner technology for the Quiet Aircraft Technology (QAT) Program. Analytical models, i.e. lumped element model (LEM) and transfer matrix (TM) representation of the EMHR, have been developed to predict the acoustic behavior of the EMHR. The models have been implemented in a MATLAB program and used to compare with measurement results. Moreover, the prediction performance of models is further improved with the aid of parameter extraction of the piezoelectric backplate. The EMHR has been experimentally investigated using standard two-microphone method (TMM). The measurement results validated both the LEM and TM models of the EMHR. Good agreement between predicted and measured impedance is obtained. Short- and open-circuit loads define the limits of the tuning range using resistive and capacitive loads. There is approximately a 9% tuning limit under these conditions for the non-optimized resonator configuration studied. Inductive shunt loads result in a 3 degree-of-freedom (DOF) system and an enhanced tuning range of over 20% that is not restricted by the short- and open-circuit limits. Damping coefficient measurements for piezoelectric backplates in a vacuum chamber are also performed and indicate that the damping is dominated by the structural damping losses, such as compliant boundaries, and other intrinsic loss mechanisms. Based on models of the EMHR, a Pareto optimization design of the EMHR has been performed for the EMHR with non-inductive loads. The EMHR with non-inductive loads is a 2DOF system with two resonant frequencies. The tuning ranges of the two resonant frequencies of the EMHR with non-inductive loads cannot be optimized simultaneously; a trade-off (i.e., a Pareto solution) must be reached. The Pareto solution provides the information for a designer that shows how design trade-offs can be used to satisfy specific design requirements. The optimization design of the EMHR with inductive loads aims at optimal tuning of these three resonant frequencies. The results indicate that it is possible to keep the acoustic reactance of the resonator close to a constant over a given frequency range. An effort to mimic the second layer of the

NASA 2DOF liner using a piezoelectric composite diaphragm has been made. The optimal acoustic reactance of the second layer of the NASA 2DOF liner is achieved using a thin PVDF composite diaphragm, but matching the acoustic resistance requires further investigation. Acoustic energy harvesting is achieved by connecting the EMHR to an energy reclamation circuit that converts the ac voltage signal across the piezoceramic to a conditioned dc signal. Energy harvesting experiment yields 16 mW continuous power for an incident SPL of 153 dB. Such a level is sufficient to power a variety of low power electronic devices. Finally, technology transfer has been achieved by converting the original NASA ZKTL FORTRAN code to a MATLAB code while incorporating the models of the EMHR.

Initial studies indicate that the EMHR is a promising technology that may enable low-power, light weight, tunable engine nacelle liners. This technology, however, is very immature, and additional developments are required. Recommendations for future work include testing of sample EMHR liner designs in NASA Langley's normal incidence dual-waveguide and the grazing-incidence flow facility to evaluating both the impedance characteristics as well as the energy reclamation abilities. Additional design work is required for more complex tuning circuits with greater performance. Poor electromechanical coupling limited the electromechanical tuning capabilities of the proof of concept EMHR. Different materials than those studies and perhaps novel composite material systems may dramatically improve the electromechanical coupling. Such improvements are essential to improved mimicking of existing double layer liners.

2 Objectives

The objective of this study is to develop electromechanical acoustic liner technology for future tunable systems using smart materials technology. Specifically, to achieve this objective, the following tasks are required:

- Develop a physics-based impedance prediction model to convert the selected electromechanical inputs into acoustic impedance
- Experimentally verify the performance of the EMHR and validate the modeling
- Develop the architecture to enable optimization studies to aid in the design of liners to achieve a target impedance range

- Design a single cell of an electromechanical liner with the goal achieving a NASA-specified impedance range
- Incorporate the impedance prediction model into the existing NASA-LaRC Zwikker-Kosten Transmission Line Code (ZKTL)

3 Background Information

Equation Section 1Originating from the operation of military and commercial airplanes, aircraft noise exposure can extend many miles beyond the boundaries of an airport. Aircraft noise is potentially dangerous for humans, i.e., aircrew and passengers, ground crews and mechanics, and people working or living in the vicinity of the airport. With more and more people suffering adverse effects due to aircraft noise, public awareness of and concerns for noise emitted from aircraft have increased tremendously. As a consequence, worldwide policies and laws have been enacted to restrict the noise emission from aircraft.[1] Hence, modern aircraft must reduce their noise emissions to satisfy new government regulations.

Aircraft noise is mainly generated from the airframe and propulsion systems.[2] Propulsion noise dominates during take-off (with or without cutback in thrust) and the cruise phases of the flight. Airframe noise, on the other hand, is dominant during approach. To suppress the propulsion noise, acoustic liners are used to line the wall of the turbofan engines. Acoustic liners provide a complex impedance boundary condition for noise propagating with the engine duct.[3] The liners can either be passive or active in terms of their noise suppression characteristics. A typical passive single degree of freedom (SDOF) acoustic liner cell is essentially a Helmholtz resonator that consists of a solid backplate, perforated face sheet and honeycomb core. The conventional passive SDOF liners are most effective over a narrow frequency range.[3] Multiple DOF liners have additional perforated septum sheets and offer a wider suppression bandwidth but represent a tradeoff in terms of size, weight, and cost.[4] The greatest limitation of passive liners is the constraint of fixed impedance for a given geometry. For a given aircraft propulsion system, there may be different optimum liner impedance distributions for the differing mean-flow and acoustic source conditions associated with take-off, cut-back, and approach conditions.[4]

Active/adaptive liners have attracted more attention from researchers recently because of their promise in suppressing the engine noise under different operating conditions. The typical operating conditions of the engine include take-off/cutback, cruise, and approach. When operated at different conditions, the characteristics of the aircraft noise may be significantly different. Potential ways in which active/adaptive liners can modify acoustic liner performance in-situ include changing the geometry characteristics of the liner and using bias flow through the liner resistive elements. Little et al. tuned their resonator by changing the neck-sectional area.[5] De Bedout et al. developed a Helmholtz resonator with a cavity that allows a continuously variable volume.[6] The variable volume actuation of the cavity is realized by rotating an internal radial wall based on a tuning (control) algorithm. Both methods above mechanically modify the geometry of the resonator-like acoustic liner. Generally, there is an obvious need for an additional actuator, controller, and power supply. Thus, it is difficult to apply these methods to the acoustic liner in an engine.

Earlier in 1957, Thurston et al. indicated that steady air flow through a orifice will change its impedance.[7] In the 1970s, Howe developed a model of the Rayleigh conductivity of an aperture, which a high Reynolds number flow passed through.[8] The interaction between the incident sound wave and the mean bias flow results in the periodic shedding of vorticity. Consequently, a portion of the acoustic energy was dissipated into heat. Howe's work indicates that it is possible to enhance the sound absorption using a bias flow through the orifice of the acoustic liner. Hughes and Dowling further studied the vortex shedding mechanism for slits and circular perforations.[9, 10] The perforated liner was experimentally investigated by Sun and Jing.[11] They found that a bias flow can enhance sound absorption and extend the effective bandwidth of the perforated liner.

In essence, the techniques described above seek to enhance the noise absorption by modifying the impedance boundary conditions of the liner system. Furthermore, it is worth noting that all adaptive/active systems discussed above, whether by modifying the geometry of the acoustic liner or introducing a bias flow to the liner, may require actuators, sensors, and controllers. Consequently, such a system is often complex in comparison with a passive liner system. Ideally, an acoustic treatment system should be robust and lightweight, have wide noise suppression bandwidth, and have the ability to modify the performance of the system in-situ.

Another type of acoustic treatment using a Herschel-Quincke tube merits some discussion here. A Herschel-Quincke (HQ) tube is essentially a hollow side-tube that travels along the axis of a main duct (but not necessarily parallel to) and attaches to the main-duct at each of the two ends of the tube.[12] In essence, the HQ tube is a simple implementation of the interference principle to attenuate sound. The potential of HQ tube to attenuate noise for turbo-fan engine was recently investigated by Smith et al.[13, 14] They found that HQ tube can be used to attenuate low-frequency broadband noise, "buzz-saw" noise, and blade passage frequency (BPF) tones. The HQ tube can be designed to work together with passive liners, which is most effective in attenuating high-frequency noise. They also presented an adaptive HQ tube, whose resonant frequency can be tuned by an internal throttle-plate flap. Again, additional controller, sensor, and actuator hardware are needed.

A novel method to tune the impedance of the liner system is presented in this project. The primary element of this liner is a Helmholtz resonator with the standard rigid backing replaced by a compliant piezoelectric composite diaphragm.[15] The electromechanical Helmholtz resonator (EMHR) is shown in Figure 1. The acoustic impedance of the resonator is adjusted and additional degrees of freedom added via electromechanical coupling of the piezoelectric composite diaphragm to a passive electrical shunt network.

4 Lumped Element Model and Transfer Matrix of the EMHR

4.1 Description of the LEM of the EMHR

At low frequencies where, for example, the acoustic wavelength is much larger than the largest physical dimension of the device, a distributed system can be lumped into idealized discrete circuit elements.[16] Under this approximation, the linearized continuity and Euler equations may be replaced by equivalent Kirchoff's laws for volume velocity and pressure drop.

From a lumped element modeling perspective, the EMHR shown in Figure 1 is very similar to the compliant isotropic backplate Helmholtz resonator presented in Horowitz et al.[17] The primary difference is that the isotropic backplate impedance is replaced by a two-port network representing the electromechanical transduction of the piezoelectric composite backplate.[18] The EMHR is similar in nature to a synthetic jet actuator presented in Gallas et al.[19] However, the piezoelectric backplate is actively driven in the latter case, while the EMHR is a passive device whose acoustic impedance is adjusted by changing the passive loads.

The equivalent circuit representation for the EMHR is shown in Figure 2, where P and P' represent the incident and diaphragm acoustic pressures, respectively. Similarly, Q and Q' are incident and diaphragm volumetric flow rates, respectively. In the notation below, the first subscript denotes the domain (e.g., "a" for acoustic), while the second subscript describes the element (e.g., "D" for diaphragm). Hence, R_{aN} and M_{aN} are the acoustic resistance and acoustic mass of the fluid in the neck, respectively. The term C_{aC} is the acoustic compliance of the cavity, while C_{aD} and M_{aD} represent the short-circuit acoustic compliance and the acoustic mass of the piezoelectric compliant diaphragm, respectively. For the diaphragm, M_{aDrad} is the acoustic radiation mass, R_{aD} is the acoustic resistance which includes the acoustic radiation resistance and other structural damping losses. Finally, C_{eB} is the electrical blocked capacitance of the piezoelectric diaphragm (i.e., when the diaphragm does not move so that its volumetric flow rate is zero), ϕ is the effective acoustic piezoelectric transduction ratio (in Pa/V), Z_{eL} is the electrical load impedance across the piezoelectric backplate, and V is the voltage output generated across the piezoelectric backplate under the excitation of an incident acoustic wave. From the equivalent circuit representation of the EMHR, shown in Figure 2, the acoustic input impedance of the EMHR is given by

$$Z_{aIN} = \frac{P}{Q} = R_{aN} + sM_{aN} + \frac{\dfrac{1}{sC_{aC}}\left(\dfrac{1}{sC_{aD}} + R_{aD} + s\left(M_{aD} + M_{aDrad}\right) + \dfrac{\phi^2 Z_{eL}}{1 + sC_{eB}Z_{eL}}\right)}{\dfrac{1}{sC_{aC}} + \dfrac{1}{sC_{aD}} + R_{aD} + s\left(M_{aD} + M_{aDrad}\right) + \dfrac{\phi^2 Z_{eL}}{1 + sC_{eB}Z_{eL}}}. \quad (1)$$

The parameters of the LEM of the EMHR are listed in Table 1. Appendix A presents the extraction of the model parameters for the piezoelectric backplate. The analysis of the tuning behavior of the EMHR based on the LEM is given in Appendix B. An experimental study of the tuning capabilities of the EMHR is presented in Section 8.

Table 1. LEM parameter estimation for the neck and cavity of the EMHR [17, 18, 20-23]

	Acoustic impedance	Description
Neck[20, 21]	R_{aN}	$R_{aN} = \frac{t}{r}\frac{\sqrt{2\mu\rho_0\omega}}{\pi r^2} + 2\frac{\sqrt{2\mu\rho_0\omega}}{\pi r^2} + \frac{\rho_0 c_0}{\pi r^2}\left[1-\frac{2J_1(2kr)}{2kr}\right]$, where J_1 is the Bessel function of the first kind, $k = \omega/c_0$ is the wave number
	M_{aN}	$M_{aN} = \frac{\rho_0\left(t+\Delta t\right)}{\pi r^2}$, where $\Delta t = 0.85r\left(1-0.7\frac{r}{R}\right)+0.85r$
Cavity[22, 23]	C_{aC}	$C_{aC} = \frac{\forall}{\rho_0 c_0^2}$, where $\forall$ is volume of the cavity
Piezoelectric backplate[18]	C_{aD}	$C_{aD} = \int_0^{R_2} 2\pi r w(r) dr \Big/ P \Big\vert_{V=0}$
	M_{aD}	$M_{aD} = \frac{2\pi}{\left(\Delta\forall\right)^2}\int_0^{R_2} \rho_A \left(w(r)\right)^2 r dr \Big\vert_{V=0}$
	M_{aDrad}	$M_{aDrad} = \frac{8\rho_0}{3\pi^2 R_2}$ [22]
	R_{aD}	$R_{aD} = 2\zeta\sqrt{\frac{M_{aD}+M_{aDrad}}{C_{aD}}}$ where ζ is the experimentally determined damping factor [24]
	ϕ	$\phi = \frac{-d_a}{C_{aD}} = \frac{-\int_0^{R_2} 2\pi r w(r) dr \Big/ V \Big\vert_{P=0}}{C_{aD}}$
	C_{eB}	$C_{eB} = C_{eF}\left(1-\kappa^2\right) = \frac{\varepsilon_r \varepsilon_0 \pi R_1^2}{h_p}\left(1-\kappa^2\right)$ where ε_r is the relative dielectric constant of the piezoelectric material, ε_0 is the permittivity of free space, and $\kappa^2 = d_a^2 / C_{EF} C_{aD}$ is the electroacoustic coupling factor

4.2 Development of the transfer matrix of the EMHR

The transfer matrix (also called the transmission matrix or the four-pole parameter representation) method has been widely used in acoustic engineering.[25] The analysis of complicated systems is greatly simplified by the use of the transfer matrix method. A complicated system can be simply regarded as a "black box" with one input port and one output port. Matrix algebra can then be applied to the general treatment of such networks.

The interconnection of parallel, series-parallel, and parallel-series network combinations can then be handled by simple linear addition or multiplication of the four-pole parameter matrix.[26]

The transfer matrix for an EMHR mounted at the end of plane wave tube (PWT) has been developed. As shown in Figure 3, the EMHR mounted at the end of the PWT composes of the following four components:

- area contraction
- area expansion
- duct element
- piezoelectric backplate with shunt network

Hence, it is convenient to develop the transfer matrix for all these elements, and then multiply these matrices sequentially to obtain the transfer matrix of the EMHR as

$$\begin{bmatrix} P_5 \\ \rho_0 c_0 U_5 \end{bmatrix} = \underbrace{\begin{bmatrix} 1 & \zeta_4 \\ 0 & A_4/A_5 \end{bmatrix}}_{\substack{\text{Transfer matrix for} \\ \text{area contraction}}} \underbrace{\begin{bmatrix} \cosh\left(\Gamma_N kt\right) & \sinh\left(\Gamma_N kt\right) G_N^{-1} \\ G_N \sinh\left(\Gamma_N kt\right) & \cosh\left(\Gamma_N kt\right) \end{bmatrix}}_{\text{Transfer matrix for neck of the EMHR}} \underbrace{\begin{bmatrix} 1 & \left(A_2/A_3\right)\zeta_3 \\ 0 & A_2/A_3 \end{bmatrix}}_{\substack{\text{Transfer matrix for} \\ \text{area expansion}}}$$

$$\underbrace{\begin{bmatrix} \cosh\left(\Gamma_C kL\right) & \sinh\left(\Gamma_C kL\right) G_C^{-1} \\ G_C \sinh\left(\Gamma_C kL\right) & \cosh\left(\Gamma_C kL\right) \end{bmatrix}}_{\text{Transfer matrix for cavity of the EMHR}} \underbrace{\begin{bmatrix} \dfrac{j\omega C_{eB} Z_{aD} + \phi^2}{\phi} & -\dfrac{Z_{aD}}{\phi} \\ \dfrac{j\omega \rho_0 c_0 C_{eB}}{A_D \phi} & -\dfrac{\rho_0 c_0}{A_D \phi} \end{bmatrix}}_{\substack{\text{Transfer matrix for} \\ \text{PZT-backplate}}} \begin{bmatrix} V \\ I \end{bmatrix}. \qquad (2)$$

Notations in the equation above, the transfer matrix development details are presented in Appendix C.

5 Optimization of the EMHR

5.1 Objective of the optimization

The synthesis of the optimization design problem for the EMHR aims at providing the architecture to enable optimization studies to aid in the design of liners to achieve a desired impedance range. The optimization design studies of the EMHR follow two paths. The first path is to maximize the tuning range of the EMHR with non-inductive loads. The EMHR with non-inductive loads is 2DOF and has two resonant frequencies.

Both resonant frequencies can be tuned by adjusting the electrical impedance of the non-inductive shunts. The difference between the open-circuit resonant frequency and its respective short-circuit counterpart is defined as the tuning range. The optimal design of the 2DOF EMHR consequently aims to maximize the tuning ranges of both resonant frequencies of the EMHR. The second path is to maximize the tuning range of the EMHR with inductive loads. The EMHR with inductive loads is 3DOF and has three resonant frequencies.

5.2 Optimizing single tuning range of EMHR with non-inductive loads

The EMHR with non-inductive loads has two resonant frequency ω_1 and ω_2, and thus has two tuning ranges $\Delta\omega_1$ and $\Delta\omega_2$. The single objective design optimization problem seeks to maximize either tuning range, $\Delta\omega_1$ or $\Delta\omega_2$, which are functions of the geometric parameters listed in Table 2. To simplify the problem, it is assumed that the material properties of the piezoelectric composite diaphragm, i.e. Lead Zirconate Titanate (PZT) composite diaphragm, listed in Table 3 are constant. The optimization is formulated as follows:

- Minimize the Objective function: $-\Delta\omega_1$ or $-\Delta\omega_2$
- Design variables: r, t, R, L, R_1, h_p, R_2 and h_s
- Constraints:
  1) Geometry constraints that impose physical limitations on the design variables. The constraints are based on the size of the test apparatus, available commercial piezoelectric benders, and size restrictions on the EMHR.
  2) Frequency constraint that confines the first short-circuit resonant frequency f_{1s} of the EMHR to a particular range (1200 Hz to 1900 Hz) where noise suppression is preferred, while also prescribing an upper limit of 3500 Hz for f_{2s}
  3) Lower bounds (LB) and upper bounds (UB): $LB \le \left\{r, t, R, L, R_1, h_p, R_2, h_s\right\} \le UB$, where LB and UB of each design variable are listed in Table 2.

Clearly, both the objective function and the frequency constraint are nonlinear; thus the optimal design of the EMHR is classified as a constrained nonlinear optimization problem. Mathematically, the single objective optimization of the EMHR is

Minimize $-\Delta\omega_1(\mathbf{x})$ or $-\Delta\omega_2(\mathbf{x})$, where $\mathbf{x}$ is the design variable vector

Subject to

$$\begin{aligned}
&R - R_2 \le 0; \quad R_1 - R_2 < 0; \\
&-h_p - h_s + 10^{-4} \le 0; \quad h_p + h_s - 10^{-3} \le 0; \\
&1200 - \omega_{1s}/2\pi \le 0; \quad \omega_{1s}/2\pi - 1900 \le 0; \quad \omega_{2s}/2\pi - 3500 \le 0 \\
&LB_i/x_i - 1 \le 0; \quad x_i/UB_i - 1 \le 0;
\end{aligned} \tag{3}$$

where $\{x_i\} = \{r, t, R, L, R_1, h_p, R_2, h_s\}\ i = 1,2...8$.

Table 2. Design optimization variables of the EMHR (Unit: mm).

Description	Symbol	Lower Bound (LB)	Upper Bound (UB)
Neck radius	r	0.5	3.5
Neck thickness	t	1	4.5
Cavity depth	R	5	15
Cavity radius	L	10	20
Piezoceramic radius	R_1	1	25
Piezoceramic thickness	h_p	0.05	1
Shim radius	R_2	5	25
Shim thickness	h_s	0.05	1

The optimization defined above was first implemented using the *fmincon* command in the Matlab Optimization Toolbox and then verified using a Genetic Algorithm provided by Matlab Genetic Algorithm Direct Search (GADS) toolbox. One set of the optimization results are listed in Table 4. The initial values of the design variables are chosen based on the prototype of the EMHR discussed in Liu *et al.*[27] The initial design vector satisfies all constraints and thus is a feasible initial condition. Different initial design vectors are explored next. The result of the optimization depends strongly on the initial values. However, the collective optimal results show that any improvement in one tuning range ($\Delta\omega_1$ or $\Delta\omega_2$) can only occur by compromising the other tuning range. Both tuning ranges $\Delta\omega_1$ and $\Delta\omega_2$ cannot maximized simultaneously, as shown in Table 4.

Table 3. Material properties of piezoelectric composite diaphragm

Piezoelectric composite diaphragm	Piezoceramic (APC 850)	Young's Modules (Gpa)	63
		Density (kg/m^3)	7700
		Relative dielectric constant	1750
		Poisson's ratio	0.31
	Shim (260 half Brass)	Young's Modules (GPa)	110
		Density (kg/m^3)	8530
		Poisson's ratio	0.37

Table 4. Single objective optimization results of the EMHR (dimension units in mm).

	Initial value	Optimizing $\Delta\omega_1$	Optimizing $\Delta\omega_2$
r	2.39	3.50	3.50
t	2.18	1.0	1.0
R	6.35	5.96	15.0
L	15.2	12.6	16.2
R_1	10.1	21.8	16.2
h_p	0.12	0.75	0.74
R_2	12.4	23.2	17.2
h_s	0.17	0.30	0.23
$\Delta\omega_1$ *(rad)*	211.7	1085.3	1.60
$\Delta\omega_1/\omega_{1s}$	1.86%	9.09%	0.02%
$\Delta\omega_2$ *(rad)*	607.5	44.4	2042.6
$\Delta\omega_2/\omega_{2s}$	4.14%	0.2%	9.29%

5.3 Pareto optimization of the EMHR with non-inductive loads

It is impossible to simultaneously maximize both $\Delta\omega_1$ and $\Delta\omega_2$ for the EMHR with non-inductive loads. Therefore, a trade-off approach is pursued. Pareto optimization is thus explored to optimize both tuning rages at the time to achieve a Pareto solution. The Pareto solution (also called a Pareto optimal) is one where any improvement of one objective degrades at least one other objective. Three methods have been explored to obtain a Pareto solution for multiple-objective optimization of the EMHR: the ε -

constraints method,[28] the traditional weighted sum method,[29] and the adaptive weighted sum (AWS) method.[30] Mathematically, the ε-constraints method is

Minimize $-\Delta\omega_2(\mathbf{x})$, where $\mathbf{x}$ is the design variable vector

Subject to

$$\begin{array}{l} -\Delta\omega_1 \le \varepsilon; \\ R - R_2 \le 0; \quad R_1 - R_2 < 0; \\ -h_p - h_s + 10^{-4} \le 0; \quad h_p + h_s - 10^{-3} \le 0; \\ 1200 - \omega_{1s}/2\pi \le 0; \quad \omega_{1s}/2\pi - 1900 \le 0; \quad \omega_{2s}/2\pi - 3500 \le 0 \\ LB_i/x_i - 1 \le 0; \quad x_i/UB_i - 1 \le 0; \end{array} , \tag{4}$$

where $\{x_i\} = \{r, t, R, L, R_1, h_p, R_2, h_s\}\ i = 1,2...8$. The tuning range $\Delta\omega_2$ is chosen to be the primary objective function which is subject to the original constraints and an additional constraint limiting the tuning range $\Delta\omega_1$. The advantage of the ε-constraint method is that it is able to achieve the optimal solution even for a non-convex boundary of the Pareto front. The problem with this method is that it is generally difficult to choose a suitable ε.

The traditional weighted sum method is used to convert the multi-objective optimization to a single objective problem by using a weighted sum of the original multiple objectives

Minimize $-\left(\alpha_1\Delta\omega_1(\mathbf{x}) + (1-\alpha_1)\Delta\omega_2(\mathbf{x})\right)$, where $\mathbf{x}$ is the design variable vector

Subject to

$$\begin{array}{l} R - R_2 \le 0; \quad R_1 - R_2 < 0; \\ -h_p - h_s + 10^{-4} \le 0; \quad h_p + h_s - 10^{-3} \le 0; \\ 1200 - \omega_{1s}/2\pi \le 0; \quad \omega_{1s}/2\pi - 1900 \le 0; \quad \omega_{2s}/2\pi - 3500 \le 0 \\ LB_i/x_i - 1 \le 0; \quad x_i/UB_i - 1 \le 0; \end{array} , \tag{5}$$

where $0 \le \alpha_1 \le 1$ is the weighting coefficient. This method is easy to implement, but it has two drawbacks. One is that an even distribution of the weighting factors does not always achieve an even distribution of the Pareto front. The other is the weighted sum method cannot find the Pareto solution on non-convex parts of the Pareto front. Furthermore, the traditional weighted sum method can produce non-Pareto points occasionally. However, the AWS method is able to produce well-distributed Pareto solutions. For the region unexplored by the traditional weighted sum method, the AWS involves changing the weighting factor adaptively rather than by using a priori weight selections and by specifying additional inequality constraints.[30]

The Pareto solution obtained using these three methods are shown in Figure 4. Clearly, optimal solutions obtained using the weighted sum method tends to cluster together, as mentioned above. A large portion of the Pareto front is obtained using the ε-constraints method, which is simply ignored by the weighted sum method. This is due to the non-convex properties of the Pareto front. Figure 4 also shows the result of the AWS. The results indicate that the AWS addresses the drawback of the conventional weighted sum method, and produces the Pareto optimum with a good distribution. The result from the AWS method matches the result using the ε-constraint method very well.

5.4 Optimization of the EMHR with inductive loads

The EMHR with inductive loads has 3DOF and thus has three resonant frequencies. However, for the EMHR studied, there are two resonant frequencies located within the frequency range of interest, as shown in Figure 5. One possible goal of the optimization is to find an optimal EMHR in which all resonant frequencies are within the frequency range of interest and the frequency shift between the maximum and minimum resonant frequency is minimized. Thus, within a wide frequency range, the variation of the reactance of the EMHR is relative small. Mathematically, the task is described as

Minimize $\Delta\omega$

Subject to

$$\begin{aligned}
&R - R_2 \le 0; \quad R_1 - R_2 < 0; \\
&-h_p - h_s + 10^{-4} \le 0; \quad h_p + h_s - 10^{-3} \le 0; \\
&1200 - \omega_{1s}/2\pi \le 0; \quad \omega_{3s}/2\pi - 3000 \le 0 \\
&LB_i/x_i - 1 \le 0; \quad x_i/UB_i - 1 \le 0;
\end{aligned} \tag{6}$$

where $\{x_i\} = \{r, t, R, L, R_1, h_p, R_2, h_s, Z_{eL}\}\ i = 1, 2 ... 8$, and the objective function is defined as

$$\Delta\omega = \max(\omega_i) - \min(\omega_i)\ \ i = 1, 2, 3 \tag{7}$$

Note that the design variables include inductive shunt impedance. Moreover, because the optimization goal is to limit three resonant frequencies within a given frequency range, the objective function is thus set to be constant, i.e. a given negative real number. Due to highly nonlinearity of constraints, Genetic Algorithm provided by Matlab Genetic Algorithm Direct Search (GADS) toolbox is thus explored. One set of optimal results is listed in Table 5. A comparison of the acoustic impedance between the initial and optimal EMHR is shown in Figure 6. It is clear that the reactance of the optimal EMHR varies much less than the initial one.

Table 5. Optimal result for optimization of the EMHR with inductive loads (dimension units in mm)

	Initial value	Optimizing $\omega_1, \omega_2, \omega_3$
r	2.4	3.0
t	3.2	1.0
R	6.3	6.5
L	16.4	37.4
R_1	10.1	13.8
h_p	0.1	0.1
R_2	12.4	14.8
h_s	0.2	0.2
Z_{eL} (mH)	50	108.8
ω_1 *(rad)*	11422.8	9424.8
ω_2 *(rad)*	14903.7	10386.1
ω_3 *(rad)*	24045.8	12604.1

6 Mimicking the NASA 2DOF Liner

One potential application for an EMHR is to achieve the performance of an ideal 2-layer liner while possessing a smaller depth. If achieved, this could potentially result in significant cost savings due to weight and size reductions. To explore this possibility, we conducted a study to mimic an ideal NASA 2DOF liner design provided by Mr. Jones. Specifically, the goal was to replace the second layer of the liner using a piezoelectric composite diaphragm. The nominal specific acoustic impedance of NASA 2DOF liner is shown in Figure E-1.

The second-layer of a liner can be modeled as a second order system. In an attempt to achieve the desired reactance, a curve-fitting method is adopted to obtain the specific acoustic mass and compliance that satisfy the NASA DDOF requirements, as shown in Figure E-2 and Figure E-3 in Appendix E, which presents how to mimic the NASA 2DOF liner step by step. It becomes clear that the composite diaphragm should be light and compliant to achieve the goal. The PZT backplate, which is used in the EMHR under study, thus cannot satisfy such requirement due to its large density and stiffness. Moreover, the shim of the PZT backplate is made of half-hard 260 brass which further makes it difficult to mimic the NASA 2DOF liner. A possible choice is to use Polyvinylidene fluoride (PVDF) instead of the PZT and substitute a light, compliant metal shim for brass shim. In comparison with PZT, PVDF is more flexible and has lower density but provides relatively weak electromechanical transduction, see Table 6. Thus, a trade-off must be reached to design an EMHR, whether to satisfy a given impedance requirement or to obtain a satisfactory tuning range. Except for lower density and more compliance, some factors must be taken into account to choose the metal shim, such as fatigue, operation temperature and cost. One choice is to use a Titanium alloy (Ti90/Al6/V4); material properties are listed in Table 7. Figure 7 shows a possible design using Titanium alloy shim attached with PVDF film, where the damping loss is estimated using Eq.(A-9) with $\zeta = 0.02$. Note that the actual damping coefficient may differ from this and should be determined via measurement, as presented in Section 8.2. The results show good agreement between the design and the nominal requirement for the acoustic reactance, while there is a discrepancy for the acoustic resistance. The dimensions of this PVDF composite diaphragm are listed in Table 8. With the modeling tools in place, improved designs can be obtained in a more systematic study.

Table 6. Material properties of PVDF and PZT

	Density (kg/m^3)	Young's Modulus (GPa)	Poisson's Ratio	Piezo Strain Constant d_{31} (pC/N)	Relative Dielectric Constant
PVDF	1780	8.3	0.18	-22	10-12
PZT (APC850)	7700	63	0.31	-175	1700

Table 7. Material properties of the Titanium alloy

	Density (kg/m^3)	Young's Modulus (GPa)	Yield Modulus (MPa)	Melting Point (ºC)
Titanium Alloy (Ti90/Al6/V4)	4420	106-114	1035-1410	1600-1650

Table 8. Dimensions of the PVDF diaphragm

	Radius of the shim	Thickness of the shim	Radius of the PVDF	Thickness of the PVDF
PVDF Composite Diaphragm	10	0.045	7	0.09

7 Energy Harvesting Using EMHR

The acoustic energy harvester is comprised of two components, the EMHR and the energy harvester circuit, as shown in Figure 8a. The EMHR transforms incident acoustic energy into time-varying electrical energy across the high-impedance piezoceramic. This high impedance ac output voltage requires the addition of a power converter to transform the power generated into a form that is suitable for an electrical load. Figure 8b shows the model of the electromechanical Helmholtz resonator connected to a rectifier bridge, large filter capacitor C_{rect} and resistive load R_{Load}. Maximum power is delivered to the load when the magnitude of the EMHR output impedance is matched to the load resistance. Shown in Figure 8c is the electromechanical Helmholtz resonator connected to a fly-back converter. The converter provides an electronically controllable input impedance and transforms the ac voltage output of the Helmholtz resonator into a dc voltage delivered to the load. The experimental study of the energy harvesting is presented in Section 8.

8 Experimental Setup and Results

8.1 Impedance measurement for the EMHR

The experimental setup implements the standard two-microphone method for measuring acoustic impedance,[31] shown in Figure 9. The plane wave tube (PWT) consists of a 965 mm long, 25.4 mm by 25.4 mm square duct that permits a plane wave acoustic field at frequencies up to 6.7 kHz.

Four Brüel and Kjær (B&K) type 4138 microphones were used for simultaneous acoustic pressure measurements. Two microphones, labeled as Mic. 1 and Mic. 2, were flush mounted in a rotating plug to the side of the impedance tube, as shown in Figure 9. The rotating plug is used to correct for calibration errors of the microphones by repeating the measurements with the microphones in switched positions. The other two microphones were used to measure the pressure amplification frequency response function in this experiment. One microphone was flush mounted in the sidewall of the resonator cavity to measure the cavity pressure. The second was flush mounted to the end face of the impedance tube to measure the total acoustic pressure at the entrance of the resonator. This microphone also served as a reference to monitor SPL at the neck of the resonator. In the experiment, the SPL is set to be low enough (<100dB) for nonlinear behavior of the EMHR to be neglected.

All microphones are calibrated with a B&K 4228 Pistonphone when connected to a B&K PULSE Multi-Analyzer System Type 3560. The PULSE system served as the power supply and data acquisition and processing system for the microphones as well as the signal source. A pseudo-random waveform generated from the PULSE system was fed through a Techron Model 7540 power supply amplifier to drive a BMS H4590P compression driver. The driver, which can produce acoustic waves between 200 Hz and 22 kHz, was connected to one end of the PWT via a transition piece. The pseudo random waveform was bandpass filtered from 300 Hz to 6.7 kHz. Meanwhile, a zoom FFT with 1500 ensemble averages was performed on each incoming microphone signal.

The specimen used in the acoustic impedance measurement using TMM is an EMHR, as shown in Figure 1. The piezoelectric backplate is a commercially available piezoceramic circular bender disk from APC International, Ltd. The piezoceramic material employed in this bender disk is APC850 lead zirconate titanate (PZT). The material properties and dimensions of the piezoelectric backplate Helmholtz resonator are listed in Table 3 and Table 9, respectively. A variety of loads were used in the experiment to investigate the tuning ability of the resonator. Table 10 lists the different loads used in the experiment.

Table 9. Dimensions of the EMHRs (Unit: mm)

			Case I	Case II
Neck		Radius r	2.42	2.42
		Length t	3.16	3.16
Cavity		Radius R	6.34	6.34
		Depth L	16.4	9.4
Piezoelectric backplate	piezoceramic	Radius R_1	10.1	10.1
		Thickness h_p	0.13	0.13
	shim	Radius R_2	12.4	12.4
		Thickness h_s	0.19	0.19

8.2 Damping coefficient measurement

It is difficult to accurately model damping of the EMHR. The damping may arise from acoustic radiation, thermo-elastic dissipation, compliant boundaries, and other intrinsic loss mechanisms.[32] Generally, the present model employed in this study only accounts for the acoustic radiation loss. The damping loss measurement thus provides a way to check if the acoustic radiation loss represents the damping of the system. The schematic of the experimental setup for the damping coefficient measurement is shown in Figure 10. The piezoelectric backplate is placed within a vacuum chamber capable of producing a low pressure around 10 Torr (1300 Pa). A LK-G32 high accuracy laser displacement sensor is used to measure the vibration response of the plate. The repeatability of the sensor is 0.05 μm, and the measurement range is 5 mm. A rectangular waveform (1 Hz, 10Vp-p) generated from the Agilent 33120A Waveform Generator is used to excite the piezoelectric plate. This signal is also used to be the external trigger of the Tek TDS5104B oscilloscope which acquires data from the laser displacement sensor. In addition, 1024 ensemble averages are performed.

Table 10. Selected loads matrix used in the experiment to tune the EMHR

Resistive loads (Ω)		Capacitive loads (nF)		Inductive loads (mH)	
nominal	measured	nominal	measured	nominal	measured
Short	Short	Short	Short	Short	Short
200	199	10	10.3	33	31.9 (70)
2k	1.98k	47	37.8	60	57.2 (130)
7.5k	7.44k	100	89.7	100	101 (65)
Open	Open	Open	Open	Open	Open

8.3 Parameter extraction of the piezoelectric backplate

As discussed in Section 4, it is very important for both LEM and TM to accurately model the piezoelectric backplate. The parameter extraction provides a way to validate the model of the piezoelectric plate. The experimental setup for parameter extraction of the piezoelectric backplate is similar to the damping measurement setup described above with two exceptions. The piezoelectric backplate is not placed within the vacuum chamber and the transverse displacements along the radius of the backplate are measured to reconstruct the deformation of the plate due to the application of the voltage. When the deformation of the plate is measured, the effective acoustic piezoelectric coefficient, d_a , and the impedance transformer factor, ϕ , and the blocked electrical capacitance, C_{eB} , of the piezoelectric backplate can then be deduced and compared with the model.

8.4 Energy harvesting experiment

The experimental setup for acoustic energy harvesting is similar to the tunable liner experimental setup mentioned above, shown in Figure 9, with one exception. The electrical terminals of the EMHR are connected to a power energy harvesting circuit via a 1:1 isolation transformer which is used to prevent ground loops.

8.4 Experimental results and discussion

8.4.1 Acoustic impedance measurement results

Figure 11 shows the acoustic impedance measurement results for the resonator (Case I) with a variety of capacitive loads. The EMHR with capacitive loads has two resonant frequencies, located where the reactance of the EMHR crosses zero with positive slope. There is also an anti-resonant frequency where the reactance of the EMHR crosses the zero with negative slope. As the capacitance is increased, the second resonant frequency shifts towards the short-circuit case from the open-circuit case, while the first resonant frequency barely changes for the EMHR (Case I). This is because of the weak coupling between the Helmholtz resonator and the PZT backplate for the tested EMHR. There is an approximately 9% capacitive tuning range for Case I resonator under the conditions and geometry listed in Table 9.

Figure 12 shows the measured acoustic impedance for different resistive loads across the resonator (Case I). The EMHR with resistive loads has 2DOF. A trend similar to the capacitive tuning can be observed for the resistive tuning, in which the tuning range is also defined by the short- and open-circuit limits. When the resistance is increased, the resonant frequency shifts toward the open-circuit case from the short-circuit case. Moreover, resistive loads increase the system damping and thus reduce the amplitude of the impedance peaks. Maximum damping occurs when resistive loads match the magnitude of the output resistance of the EMHR.

Figure 13 shows the measurement results for inductive tuning of the EMHR (Case I). Unlike capacitive and resistive tuning, EMHR with inductive loads has 3DOF and thus has three resonant frequencies. However, the third resonant frequency of the EMHR (Case I) with inductive loads is out of the frequency range of interest and is not shown in Figure 13. The third resonant frequency shifts close to the open-circuit case as the inductance is increased. Moreover, inductive tuning is not limited by the short- and open-circuit cases. The second resonant frequency shifts to lower frequencies away from the short-circuit case as the inductance is increased. For EMHR (Case I), the first resonant frequency rarely changes due to weak coupling between the piezoelectric backplate and the Helmholtz resonator. Furthermore, a real inductor has resistance as well. Thus, the peak values of the acoustic resistance and reactance of the EMHR with inductive loads has been reduced.

The experimental results of the EMHR (Case II) with short- and open-circuits are shown in Figure 14. It indicates that the first resonant frequency of the EMHR shifts due to coupling between the piezoelectric backplate and the Helmholtz resonator is not as weakly coupled as in Case I. This is because the depth of the cavity of the EMHR (Case II) is reduced. The acoustic compliance of the cavity consequently decreases. Hence, the coupling between Helmholtz resonator and piezoelectric composite backplate increases; see Appendix B for details.

The comparison between measurement data and LEM and TM is shown in Figure 15–Figure 18 . Clearly, using the measured damping loss of the PZT backplate, both LEM and TM predictions match the experimental results pretty well for the short-circuit EMHR. The TM provides a better prediction for the acoustic resistance than LEM does. This is because the TM includes the viscous loss effect on the wave propagation within the cavity. There are some other factors, as presented in Appendix D, which determines when the TM coincides with the LEM.

The predictions for the normalized specific acoustic impedance do not match the experimental data very well for the open-circuit case. One possible explanation for the observed discrepancy is that, for the short-circuit case, the piezoelectric backplate is electrically shorted and thus ϕ and C_{eB} do not affect the acoustic impedance of EMHR, as they do for the open-circuit case. Hence, any inaccuracies in either ϕ or C_{eB} will impact the predicted results. Some factors do impact the piezoelectric backplate model, such as the bond layer between the piezoceramic patch and the brass shim (the model assumes a negligible bond layer), any asymmetry in the piezoceramic patch geometry, and imperfect clamped boundary condition.[18] Figure 15 – Figure 18 also indicate that modeling damping loss of the backplate as acoustic radiation resistance severely underestimate the actual damping loss.

8.4.2 Damping coefficient measurement results

Figure 19 shows the damping coefficient measurement results for piezoelectric composite backplate in air and in a vacuum chamber. Using logarithm decrement method, and if the first two peaks are chosen, the damping coefficient is calculated

$$\zeta_{air} = 0.026 \tag{8}$$

for piezoelectric backplate in air, and

$$\zeta_{vacuum} = 0.024 \tag{9}$$

for piezoelectric backplate in a vacuum chamber. However, no measurements are exact, and the calculation of the damping factor on first two peaks may lead to errors. Hence, it is perhaps more accurate to estimate the damping coefficient by measuring the displacement at two different times separated by a given number of periods. For example, let x_1 and x_{i+1} be the peak displacements corresponding to the times t_1 and t_{i+1}, where $t_{i+1} = t_1 + iT\left(i = 1,2,3...\right)$ and T is the period of the system. Moreover,[24]

$$\frac{x_1}{x_{i+1}} = e^{i2\pi\zeta/\sqrt{1-\zeta^2}}, \tag{10}$$

from which one has the logarithmic decrement

$$\delta = \frac{2\pi\zeta}{\sqrt{1-\zeta^2}} = \frac{1}{i}\ln\frac{x_1}{x_{i+1}}, \tag{11}$$

from which one has

$$\ln x_i = \ln x_1 - \delta\left(i-1\right). \tag{12}$$

The plot $\ln x_i$ versus i should has the form of a straight line with the slope $-\delta$ if the measurement is exact. Hence, the accuracy of the estimation for the damping coefficient can be improved using Eq. (12). In particular, N peak displacements ($x_i, i=1,2,3...$) are chosen. $\ln x_i$ and $y_i = i-1$ are calculated. Then a strait line in the form

$$z_i = ay_i + b \tag{13}$$

is to be determined to minimize

$$\sum_{i=1}^{N}\left(\ln x_i - z_i\right)^2 = \sum_{i=1}^{N}\left(\ln x_i - ay_i - b\right)^2 . \tag{14}$$

Note that a corresponds to $-\delta$ in Eq. (12). The damping coefficient is thus calculated

$$\zeta = \frac{-a}{\sqrt{\left(2\pi\right)^2 + \left(-a\right)^2}} . \tag{15}$$

Twelve peak displacements are chosen from the damping measurement results of the piezoelectric plate in air and using method above obtains the damping coefficient of the piezoelectric plate in air

$$\zeta_{air} = 0.015 \tag{16}$$

which differs from the estimation in Eq. (8). The illustration of the determination of damping coefficient using the method above and the comparison between numeric fittings and measurement results are shown in Figure 20.

Following similar procedure, one has the damping coefficient of the piezoelectric plate in the vacuum chamber

$$\zeta_{air} = 0.01 \tag{17}$$

The illustration of the determination of damping coefficient in vacuum chamber and the comparison between numeric fittings and measurement results are shown in Figure 21.

8.4.3 Parameter extraction of the piezoelectric backplate

As discussed above, there is a large discrepancy between the measurement results and the predictions of both LEM and TM for open-circuited EMHRs. One possible reason for the discrepancy is that any inaccuracies in either ϕ or C_{eB} will impact the predicted results for open-circuited EMHR. Parameter extraction provides such way to check if LEM parameters of the piezoelectric plate are accurate or not. Figure 22 shows the measured displacement of the piezoelectric backplate due to the application of voltages. The results indicated that, when applying the voltage on the plate, the measured transverse displacement of the plate is larger than one calculated by the model. Consequently, the deduced parameters such as d_A and ϕ and C_{eB} differ from ones from the model, as listed in Table 11. Applying the deduced ϕ and C_{eB} to the LEM and TM results in good predictions of open-circuited EMHRs, as shown in Figure 23. However, the reasons for the discrepancy between the predicted and deduced results from the measurement data for the LEM parameters of the piezoelectric plate still require further investigations.

Table 11. Comparison between predicted and deduced LEM parameters of the Piezoelectric backplate

	d_A	ϕ	C_{eB}
Predicted	48.3e-12	82.4	45.7e-9
Deduced	71.4e-12	122.0	41.2e-9

8.4.4 Energy harvesting experiment results

To ensure maximum power transfer, it is first necessary to determine the optimal resistive load for the EMHR. A bridge rectifier, filter capacitor and load resistor are connected to the Helmholtz resonator output. The sound pressure level at the entrance of the EMHR is held constant at 140 dB, while the load resistor is swept from 1 $k\Omega$ to 100 $k\Omega$. The incident acoustic power is measured using the two microphone method. The electrical power is measured by finding the voltage across the load resistor and the current flowing through it. Figure 24a shows the output power of the EMHR versus load resistance. The experimental results show that the optimal load for the EMHR is ~18 $k\Omega$. Based on this result, the input impedance of the flyback circuit was set to 18 $k\Omega$. The flyback converter was also compared to the direct charging method, where the EMHR is connected to a rectifier bridge and large capacitor with the rechargeable battery placed in parallel with the capacitor. The power flowing into the battery is measured and this serves as a baseline for comparison. Figure 24b presents comparisons between the flyback converter, the direct charging method. The data indicate that for SPL above 140 dB the flyback converter circuit is superior to the counterpart method. Specifically, at an incident SPL of 153 dB the flyback converter harvests 139% more power than the direct charging method.

9 Conclusions and Recommendations

The EMHR is a promising technology that may enable low-power, light weight, tunable engine nacelle liners. Lumped element model (LEM) and transfer matrix (TM) of the EMHR have been developed to predict the acoustic behavior of the EMHR. The models have been implemented in a MATLAB code and incorporated into the NASA ZKTL code, which is converted to a MATLAB code from the original FORTRAN code. In this study, LEM and TM match each other pretty well within the frequency range of interest. The difference in the results is due to whether the viscous loss is taken into account when modeling the cavity of the EMHR. Moreover, the LEM coincides with the TM when some conditions are satisfied, which are listed in Appendix D. The analysis of the tuning behavior of the EMHR based on the LEM validates the experiment observation.

An experimental investigation of the EMHR has been implemented using the standard two-microphone method (TMM). The measurement results verify both LEM and TM of the EMHR. Good agreement between predicted and measured impedance was obtained. Short- and open-circuit loads define the limits of the tuning range using resistive and capacitive loads. There is approximately a 9% non-inductive tuning limit for the second resonant frequency under these conditions for the non-optimized EMHR configuration studied. Inductive shunt loads result in a 3DOF system and an enhanced tuning range of over 20% that is not restricted by the short- and open-circuit limits. The damping coefficient measurement for the piezoelectric backplate in the vacuum chamber is also performed. The results show that the acoustic radiation damping loss is relatively small. **Moreover, parameter extraction of the piezoelectric backplate is implemented to improve LEM and TM prediction performance, i.e. when EMHR is not short-circuited.**

Based on models of the EMHR, the Pareto optimization design of the EMHR has been performed for the EMHR with non-inductive loads. The EMHR with non-inductive loads is 2DOF and have two resonant frequencies. Either of them can be optimally tuned by approximately 9%. However, the results show that it is impossible to maximize both tuning ranges simultaneously. The improvement of one tuning range degrades the other. Consequently, a trade-off must be reached. In other words, a generally accepted Pareto solution should be achieved. Three methods are explored to obtain the Pareto optimal set of the bi-objective optimization design of the EMHR: the ε-constraint method, the traditional weighted sum method, and the adaptive weighted sum method. Both the ε-constraint method and the adaptive weighted sum method obtain the same Pareto front for the optimization problem, while the weighted sum method clusters the Pareto solutions around the two single-objective design points of the Pareto front. The Pareto solution provides the information for a designer that shows how design trade-offs can be used to satisfy specific design requirements. The EMHR with inductive-loads is 3DOF and has three resonant frequencies. The optimization design of the EMHR with inductive loads aims at optimal tuning of these three resonant frequencies, i.e. to constrain three resonant frequencies within a given range.

An effort to mimic the second layer of the NASA 2DOF liner using piezoelectric composite diaphragm has been made. The optimal acoustic reactance of the second layer of the NASA 2DOF liner is repeated using a thin PVDF composite diaphragm while the acoustic resistance of the mimic requires further investigation. The PVDF composite diaphragm is more flexible than the PZT composite diaphragm but possesses relatively weaker electromechanical transduction. Hence, the EMHR with a PVDF composite diaphragm has a small tuning range. Clearly, this is an area in which novel composite structures may be able to achieve improved performance whether it be in terms of increasing damping or tuning range.

Acoustic energy harvesting is achieved by connecting the EMHR to an energy reclamation circuit that converts the ac voltage signal across the piezoceramic to a conditioned dc signal. Energy harvesting experiments yield 16 mW continuous power for an incident SPL of 153 dB. Such levels are sufficient to power a variety of low power electronic devices.

Future work should include the testing of sample EMHR liner designs in NASA Langley's dual-incidence and grazing-incidence flow facilities to evaluating both the impedance characteristics as well as the energy reclamation abilities. Inductive tuning offers the capability of an increased tuning range, but further work is needed regarding the design of such liners. Specifically, system goals are required to drive the formulation of the optimal design problem. Poor electromechanical coupling limits the electromechanical tuning capabilities of the EMHR. Novel composite material systems, like an interdigitated piezoelectric composite may dramatically improve the electromechanical coupling.[33] Such improvements are essential to mimic both resistance and reactance of existing double layer liners. Furthermore, enhanced electromechanical tuning will also enable the use of more complex passive ladder circuits for impedance spectra shaping.

10 Publications

Schultz, T., Sheplak, M., and Cattafesta, L., "Application of multivariate uncertainty analysis to frequency response function estimates," revision submitted to J. Sound Vib.

Schultz, T., Sheplak, M., and Cattafesta, L., "Uncertainty analysis of the two-microphone method," accepted J. Sound Vib.

Schultz, T., Cattafesta, L., and Sheplak, M., "Modal decomposition method for acoustic impedance testing in square ducts," J. Acoust. Soc. Am. Vol. 120, No. 6, pp. 3750-3758, December 2006.

Liu, F., Horowitz, S., Nishida, T., Cattafesta, L., and Sheplak, M., "A multiple degree of freedom electromechanical Helmholtz resonator," revision submitted to J. Acoust. Soc. Am.

Liu, F., Horowitz, S., Kim, N.H., Cattafesta, L., and Sheplak, M., "Pareto optimization design of electromechanical Helmholtz resonator," In preparation.

Liu, F., Horowitz, S., Nishida, T., Cattafesta, L., and Sheplak, M., "Energy harvesting using electromechanical Helmholtz resonator," In preparation.

Chandrasekharan, V., Sheplak, M., and Cattafesta, L., "Experimental study of acoustic impedance of MEMS-based micro-Perforated Liners," AIAA 2006-2401, 12th AIAA/CEAS Aeroacoustics Conference, Cambridge, MA, May 2006.

Kadirvel, S., Liu, F., Horowitz, S., Nishida, T., Ngo, K., Cattafesta, L., and Sheplak, M., "A self-powered wireless active acoustic liner," AIAA-2006-2400, 12th AIAA/CEAS Aeroacoustics Conference, Cambridge, MA, May 2006.

Liu, F., Horowitz, S., Cattafesta, L., and Sheplak, M., "Optimization of an electromechanical Helmholtz resonator," AIAA-2006-2524, 12th AIAA/CEAS Aeroacoustics Conference, Cambridge, MA, May 2006.

Schultz, T, Cattafesta, L, and Sheplak, M, "Comparison of the two microphone method and the modal decomposition method for acoustic impedance testing," AIAA 2006-2695, 12th AIAA/CEAS Aeroacoustics Conference, Cambridge, MA, May 2006.

Schultz, T, Cattafesta, L, and Sheplak, M, "Modal decomposition method for acoustic impedance testing in rectangular ducts," AIAA 2006-1014, 44th AIAA Aerospace Sciences Meeting and Exhibit, Reno, NV, January 2006.

References

[1] Federal Aviation Administration (U. S. Department of Transportation), *Noise levels for U.S. certificated and foreign aircraft*. (2001).

[2] Smith, M.J.T., *Aircraft noise*. (Cambridge University Press, Cambridge, United Kingdom, 1989).

[3] Motsinger, R.E. and Kraft, R.E., "Design and performance of duct acoustic treatment," in Aeroacoustics of Flight Vehicles: Theory and Practice Volume 2: Noise Control, edited by H.H. Hubbard, (Acoustical Society of America, New York, 1995), Chap.14, pp. 165-206.

[4] Bielak, G.W. and Premo, J.W. and Hersh, A.S., "Advanced turbofan duct liner concepts," NASA/CR-1999-209002, (National Aeronautics and Space Administration, 1999).

[5] Little, E., Kashani, R., Kohler, J., and Morrison, F., "Tuning of an Electro-rheological Fluid-based Helmholtz Resonator as Applied to Hydraulic Engine Mounts," ASME DSC Transp. Sys. **54**, 43-51 (1994).

[6] De Bedout, J.M., Franchek, M.A., Bernhard, R.J., and Mongeau, L., "Adaptive -passive noise control with self-tuning Helmholtz resonators," J. Sound Vib. **202**, 109-123 (1997).

[7] Thurston, G.B., Hargrove, L.E. Jr., and Cook, B.D., "Nonlinear properties of circular orifices" J. Acoust. Soc. Am., **29**, 992-1001 (1967).

[8] Howe, M.S., "On the theory of unsteady high Reynolds number flow through a circular cylinder," J. Fluid Mech. **61**, 109-127 (1979).

[9] Hughes, I.J. and Dowling, A.P., "The absorption of sound by perforated linings," J. Fluid Mech. **218**, 299-355 (1990).

[10] Dowling, A.P. and Hughes, I.J., "Sound absorption by a screen with a regular array of slits," J. Sound Vib. **156**, 387-405 (1992).

[11] Jing, X.D. and Sun, X.F., "Experimental investigations of perforated liner with bias flow," J. Acoust. Soc. Am. **106**, 2436-2441 (1999).

[12] Stewart, G.W., "The theory of the Herschel-Quincke tube," Phys. Rev. **31**, 696-698 (1928).

[13] Smith, J.P. and Burdisso, R.A., "Experimental investigation of the Herschel-Quincke tube concept on the Honeywell TFE731-60," NASA/CR-2002-211430, (National Aeronautics and Space Administration, 2002).

[14] Smith, J.P. and Burdisso, R.A., "Experiments with fixed and adaptive Herschel-Quincke waveguides on the Pratt and Whitney JT15D engine," NASA/CR-2002-211430, (National Aeronautics and Space Administration, 2002).

[15] Sheplak, M., Cattafesta, L., Nishida, T., and Horowitz, S.B., "Electromechanical acoustic liner," U.S. Patent No. 6,782,109 (2004).

[16] Rossi, M., *Acoustics and Electroacoustics* (Artech House, Norwood, MA, 1988), pp. 245-373.

[17] Horowitz, S.B., Nishida, T., Cattafesta, L., and Sheplak, M., "Characterization of a compliant-backplate Helmholtz resonator for an electromechanical acoustic liner," Int. J. Aeroacoust. **1**, 183-205 (2002).

[18] Prasad, S., Gallas, Q., Horowitz, S. ,Homeijer, B. Sankar, B., Cattafesta, L., and Sheplak, M., “An Analytical Electroacoustic Model of a Piezoelectric Composite Circular Plate,” AIAA J. **44**(10), 2311-2318 (2006).

[19]Gallas, Q., Holman, R., Nishida, T., Carrol, B., Sheplak, M., and Cattafesta, L., "Lumped element modeling of piezoelectric-driven synthetic jet actuators," AIAA J. **41**, 240-247 (2003).
[20]Crandall, I.B., *Theory of Vibrating Systems and Sound* (D. Van Nostrand Company, New York, 1926), pp. 229-241.
[21]Ingard, U., "On the theory and design of acoustic resonators," J. Acoust. Soc. Am. **25**, 1037-1061 (1953).
[22]Blackstock, D.T., *Fundamental of Physical Acoustics* (John Wiley & Sons, New York, 2000).
[23] Kinsler, L.E., *Fundamentals of Acoustics* (John Wiley & Sons, New York, 2000), pp. 272-274.
[24]Meirovitch, L., *Fundamentals Of Vibrations* (McGraw-Hill, New York, 2001), pp. 94-98.
[25]Munjal, M.L., *Acoustics of Ducts and Mufflers* (John Wiley & Sons, Inc, New York, 1987), pp.75.
[26]Van Valkenburg, M.E., *Network analysis* (Prentice-Hall, Englewood Cliffs, 1964), Chapter 3 and 9.
[27]Liu, F., Horowitz, S.B., Nishida, T., Cattafesta, L., and Sheplak, M., "A tunable electromechanical Helmholtz resonator," AIAA Paper 2003-3145, in *9th AIAA/CEAS Aeroacoustics Conference and Exhibit* (Hilton Head, South Carolina, 2003)
[28]Marglin, S.A., *PublicInvestment Criteria* (M.I.T. Press, Cambridge, MA, 1967).
[29]Koski, J., "Multicriteria truss optimization," in Multicriteria Optimization in Engineering and in the Sciences, edited by W. Stadler, (Plenum Press, New York, 1988).
[30]Kim, I.Y. and de Weck, O.L., "Adaptive weighted-sum method for bi-objective optimization Pareto front generation," Struct. Multidisc. Opt. **29**, 149-158 (2005).
[31]ASTM-E1050-98, "Impedance and absorption of acoustical materials using a tube, two microphones, and a digital frequency analysis system," ASTM International.
[32]Tilmans, H.A.C., Elwenspoek, M., and Fluitman, J.H.J., "Micro Resonant Force Gauges," Sensors and Actuators A-Physical, 30, 35-53 (1992).
[33]Hong, E., Trolier-McKinstry, S. Smith, R.L. Krishnaswamy, S.V. and Freidhoff, C.B.. "Design of MEMS PZT circular diaphragm actuators to generate large deflections," J. Microelectromech. Syst. **15**(4), 832-839 (2006).
[34]Fischer, F.A., *Fundamentals of Electroacoustics* (Interscience Publishers, Inc., New York, 1955), pp.1-51.
[35]Karal, F.C., "The Analogous Acoustical Impedance for Discontinuities and Constrictions of Circular Cross Section," J. Acoust. Soc. Am. **25**(2), 327-334 (1953).
[36]Ingard, U., *Notes On Duct Attenuators (N4)*. (Self-published, Kittery Point, NE, 1999).
[37]Tijdeman, H., "On The Propagation Of Sound Waves In Cylindrical Tubes," J. Sound Vib. **39**(1), 1-33 (1973).
[38]Zwikker, C. and Kosten, C.W., *Sound Absorbing Materials* (Elsevier, Amsterdam, NY, 1949).

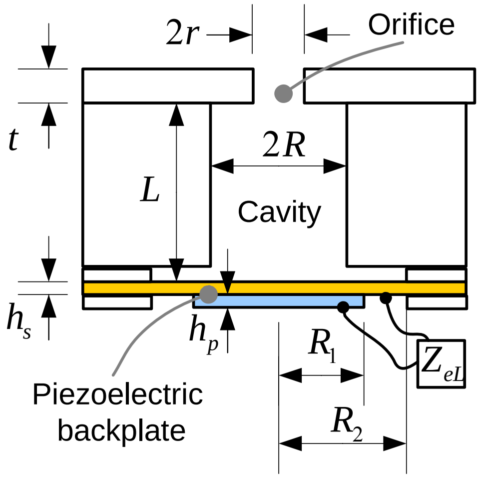

Figure 1. Schematic of the EMHR

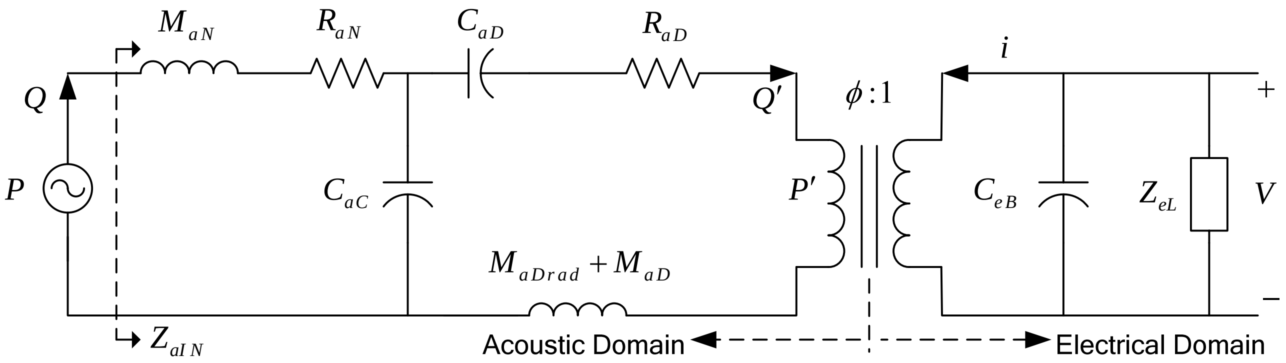

Figure 2. Equivalent circuit representation of the EMHR

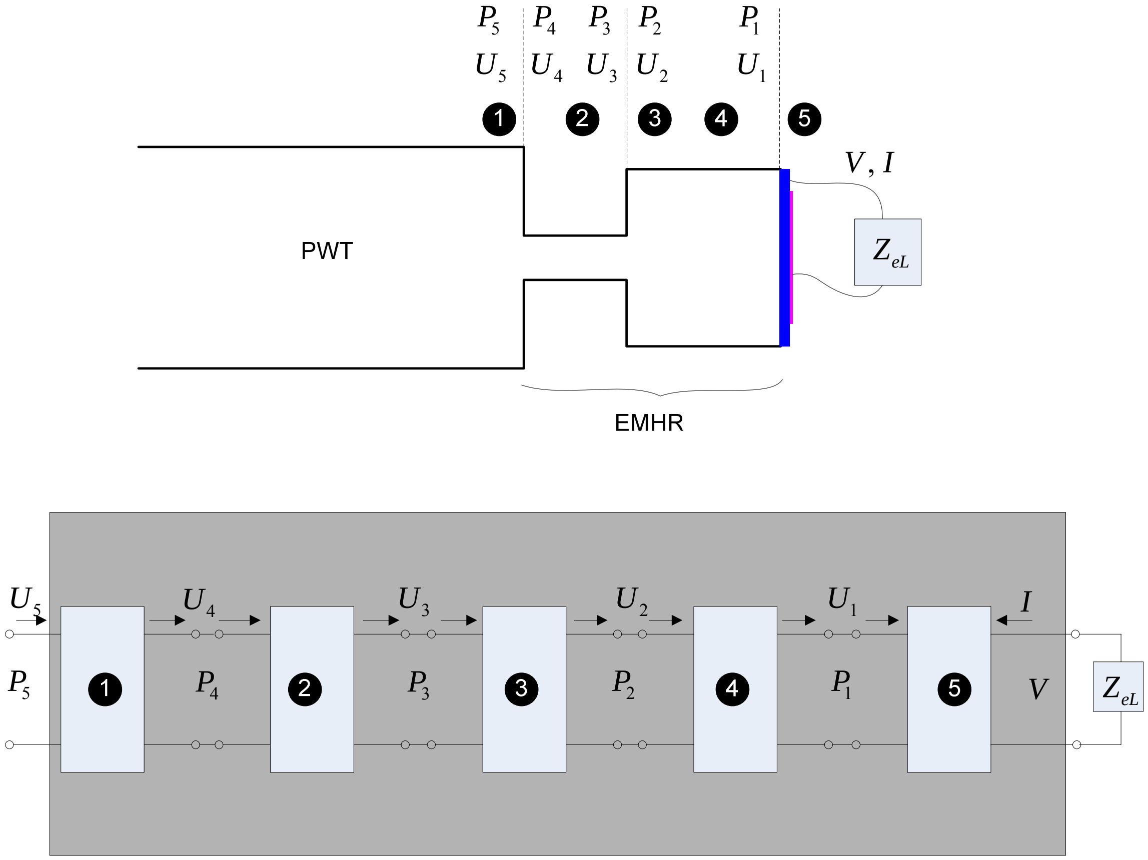

Figure 3. **Illustration of the modeling EMHR using the transfer matrix method, where each subsystem is denoted as: 1-area contraction; 2-duct element; 3-area expansion; 4-duct element; 5-piezoelectric backplate.**

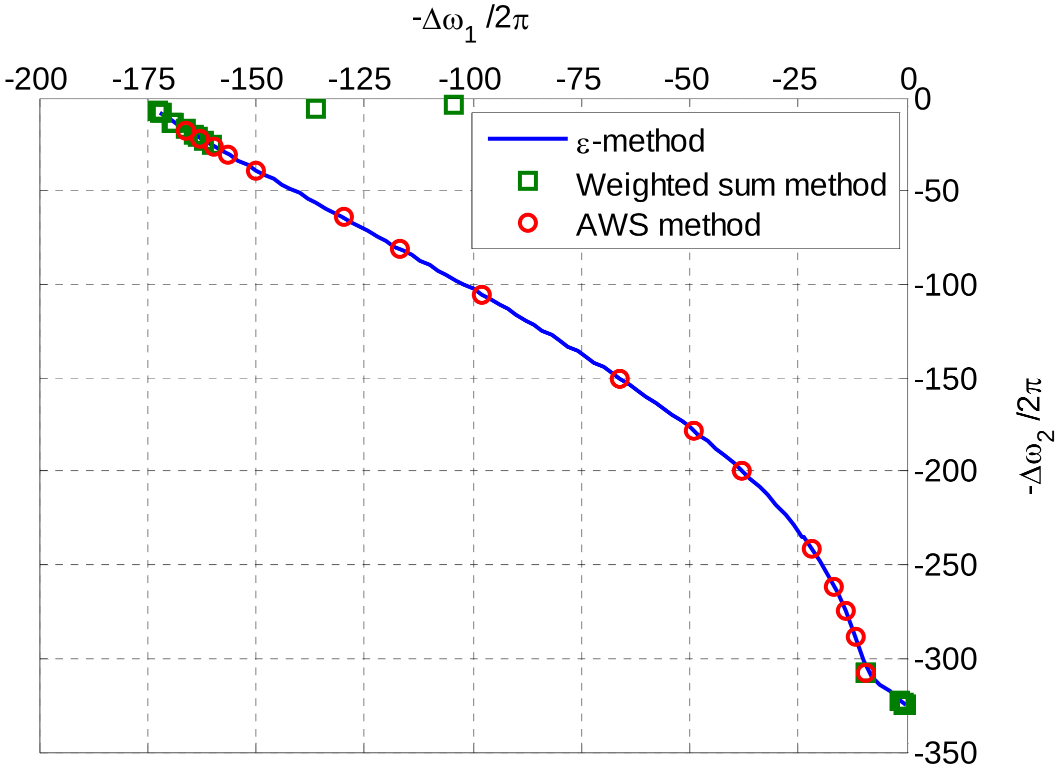

Figure 4. The Pareto front obtained via the ε-constraint, traditional weighted sum, and adaptive weighted sum methods.

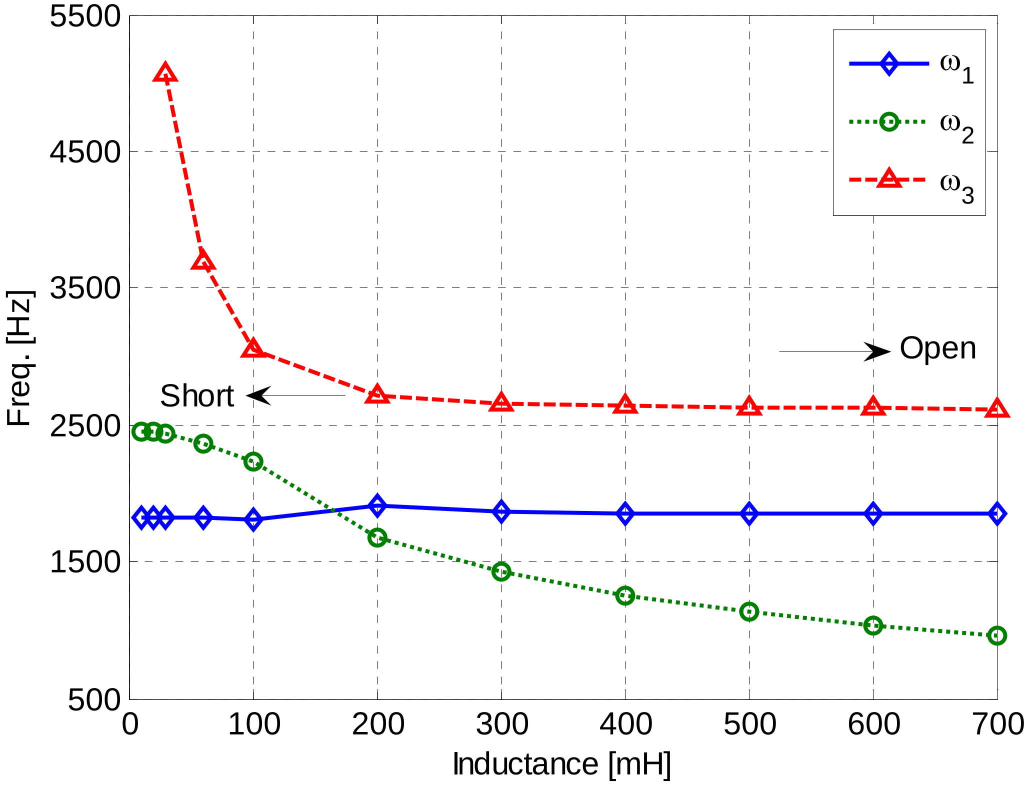

Figure 5. Three resonant frequencies of the EMHR with inductive as function of the inductive loads

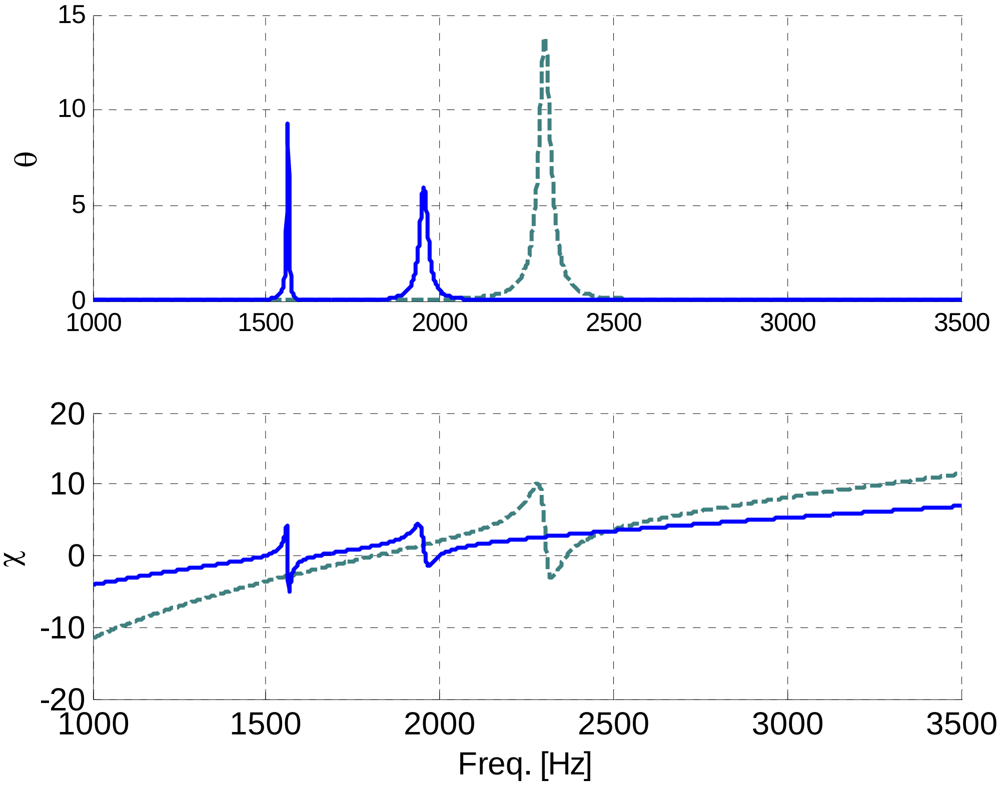

Figure 6. Comparison between initial and optimal acoustic impedance of the EMHR with inductive loads

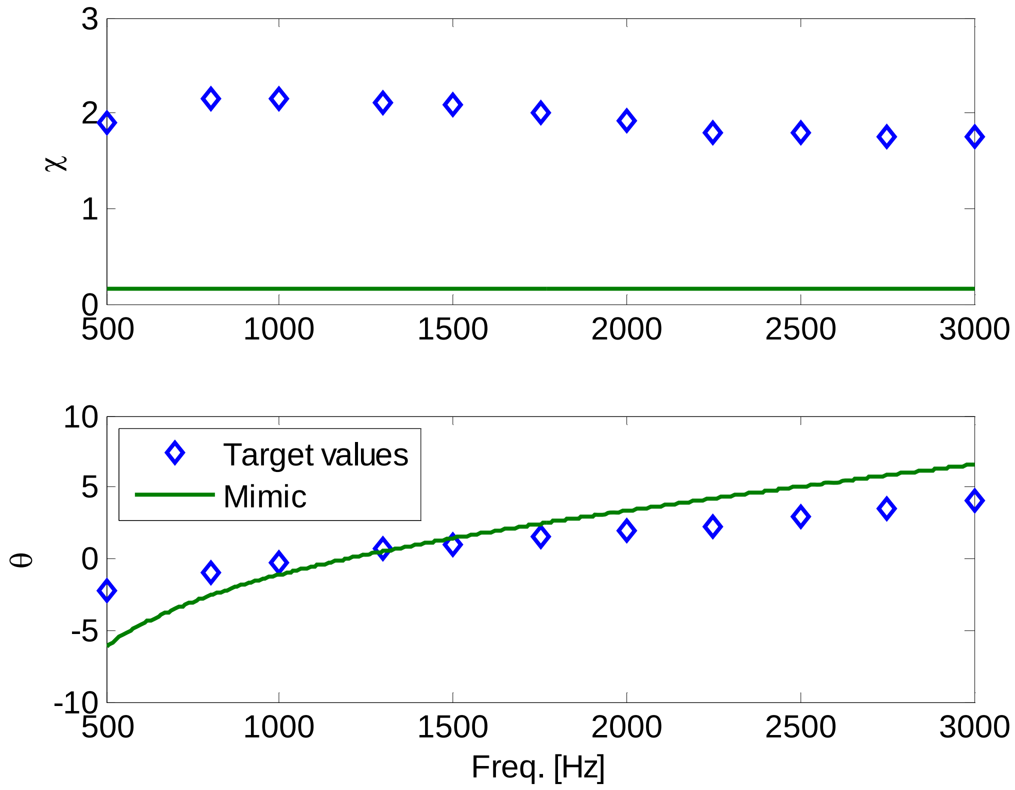

Figure 7. Mimic NASA 2DOF liner

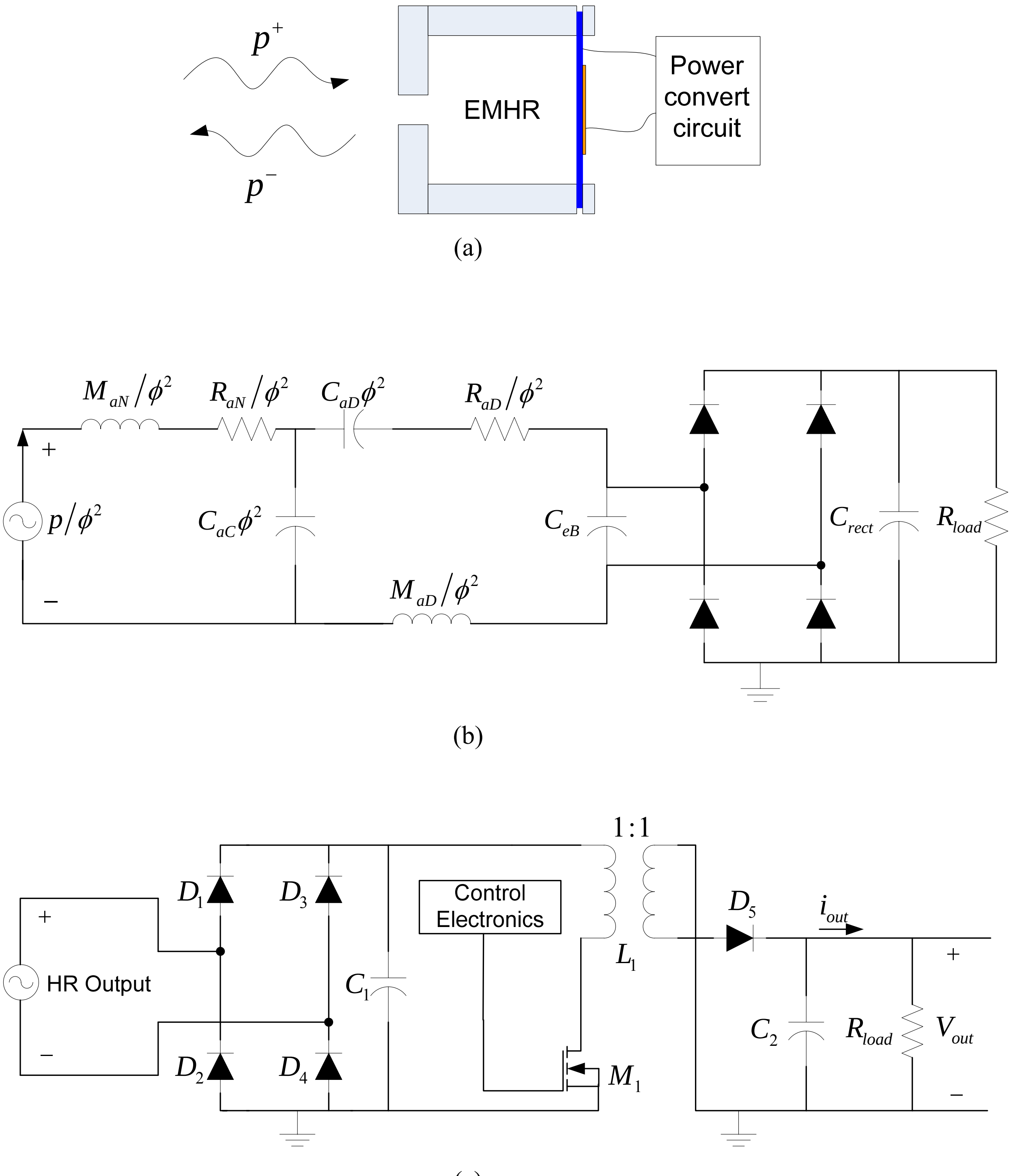

Figure 8. (a) Schematic of energy harvesting using EMHR. (b) Converter type I . (c) Fly-back converter

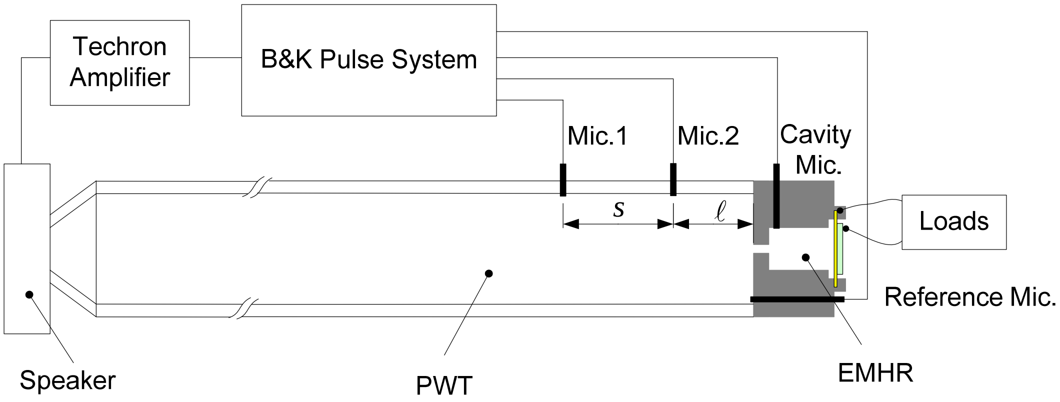

Figure 9. Schematic of the acoustic impedance measurement for the EMHR.

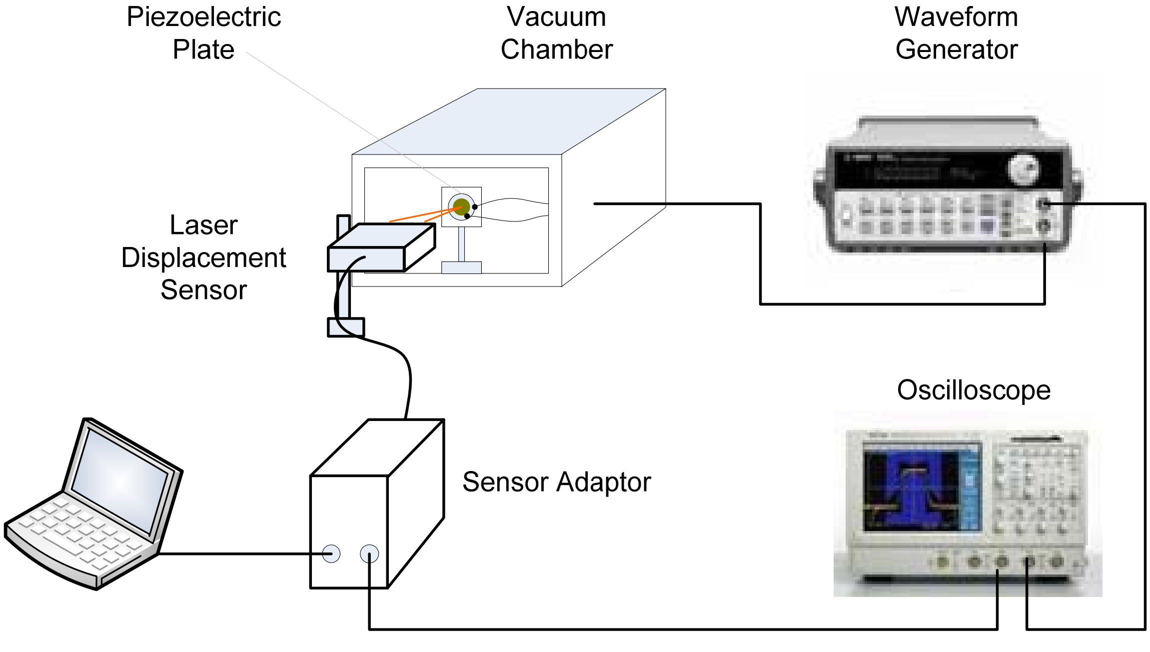

Figure 10. Schematic of the damping measurement

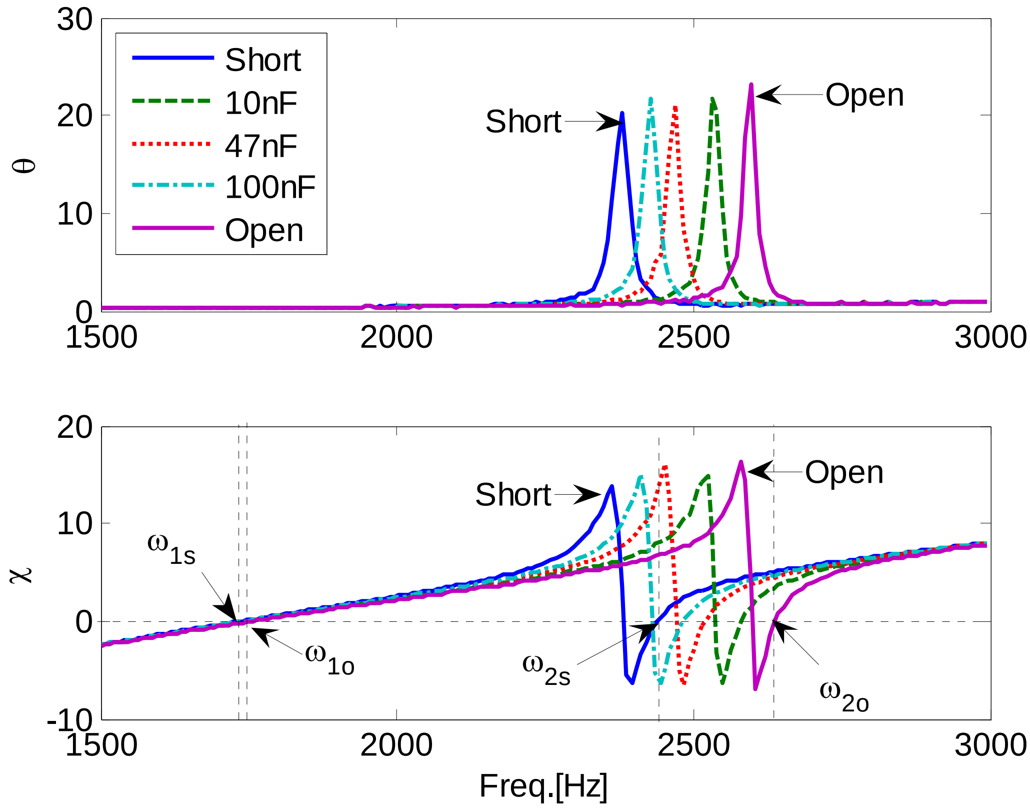

Figure 11. Experimental results for the normalized specific acoustic impedance of the EMHR (Case I) as function of the capacitive loads.

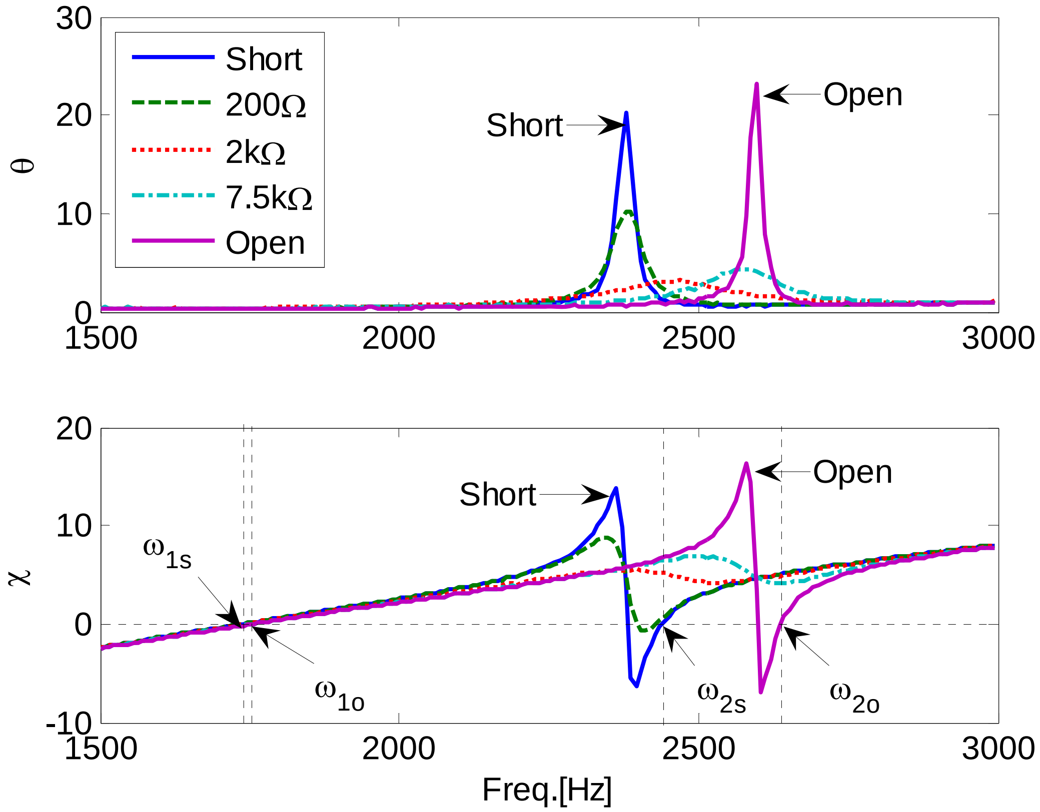

Figure 12. Experimental results for the normalized specific acoustic impedance of the EMHR (Case I) as function of the resistive loads.

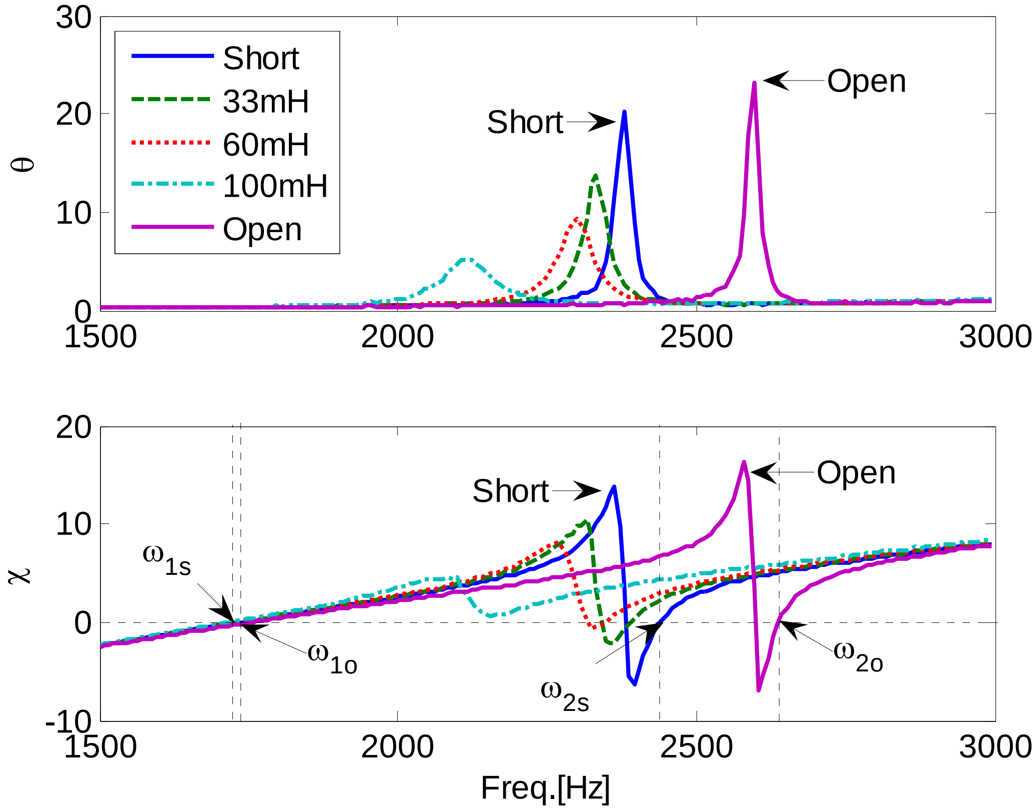

Figure 13. Experimental results for the normalized specific acoustic impedance of the EMHR (Case I) as function of the inductive loads.

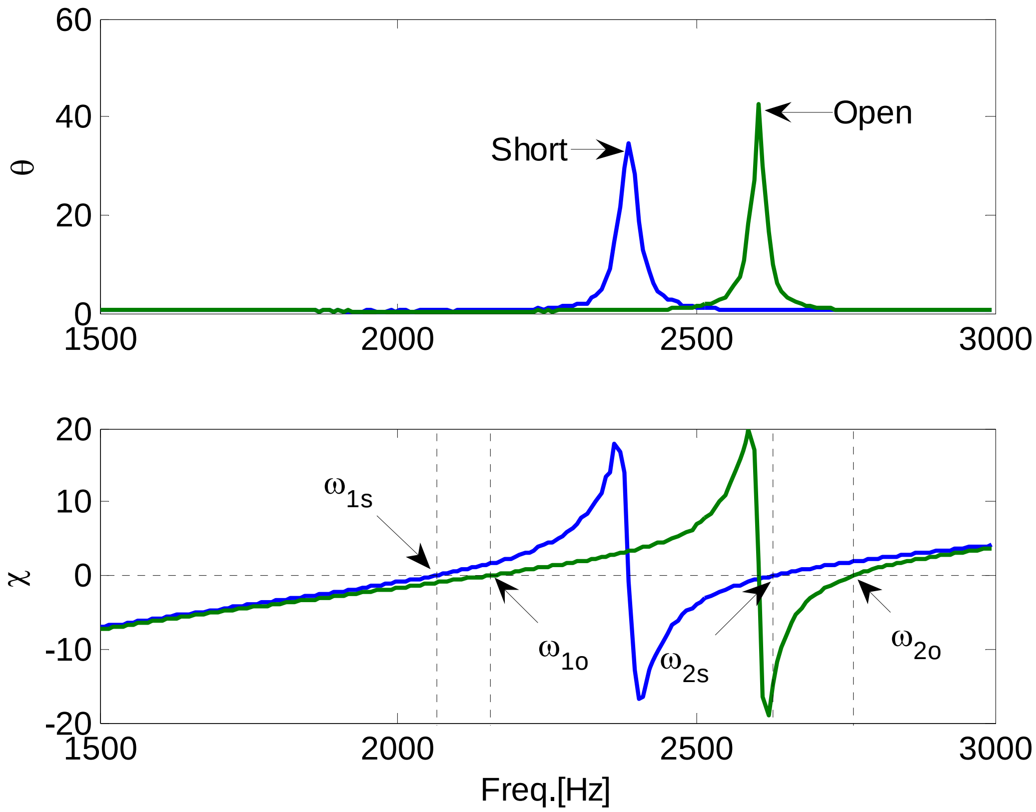

Figure 14. Experimental results of the normalized acoustic impedance of the EMHR (Case II) for the short- and open-circuit.

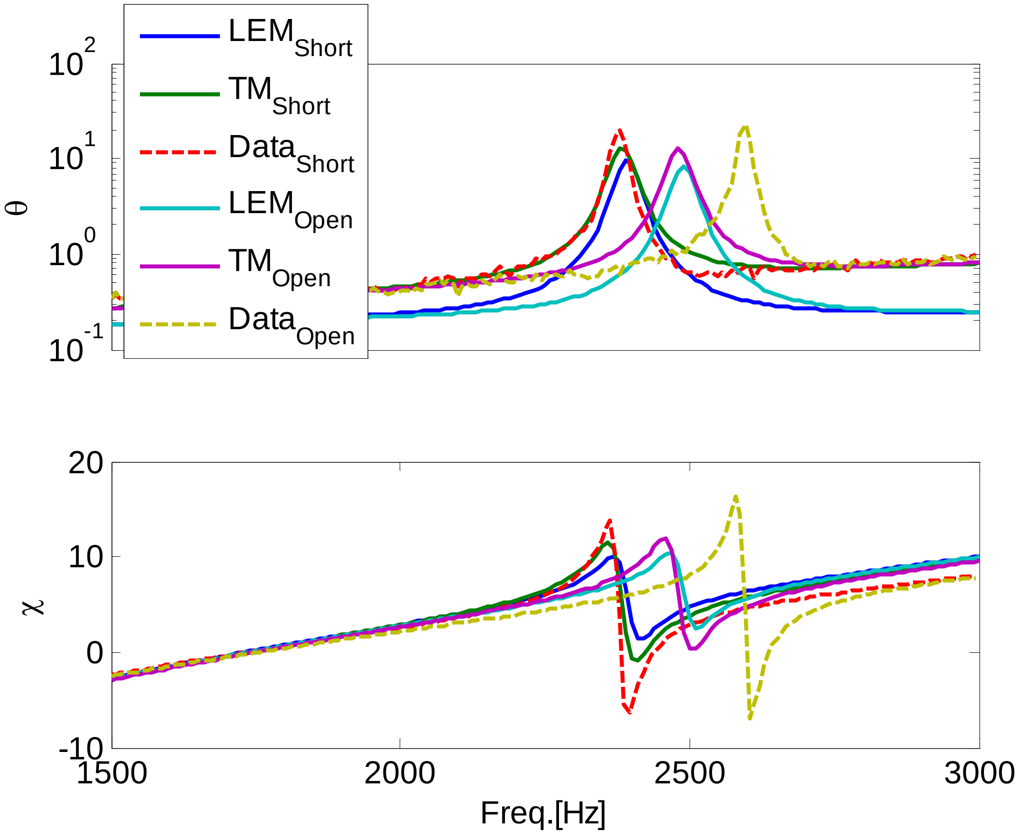

Figure 15. Comparison LEM, TR and measurement results for a short- and open-circuited EMHR (CASE I), the damping loss of the backplate is determined using logarithm decrement method ($\zeta = 0.015$)

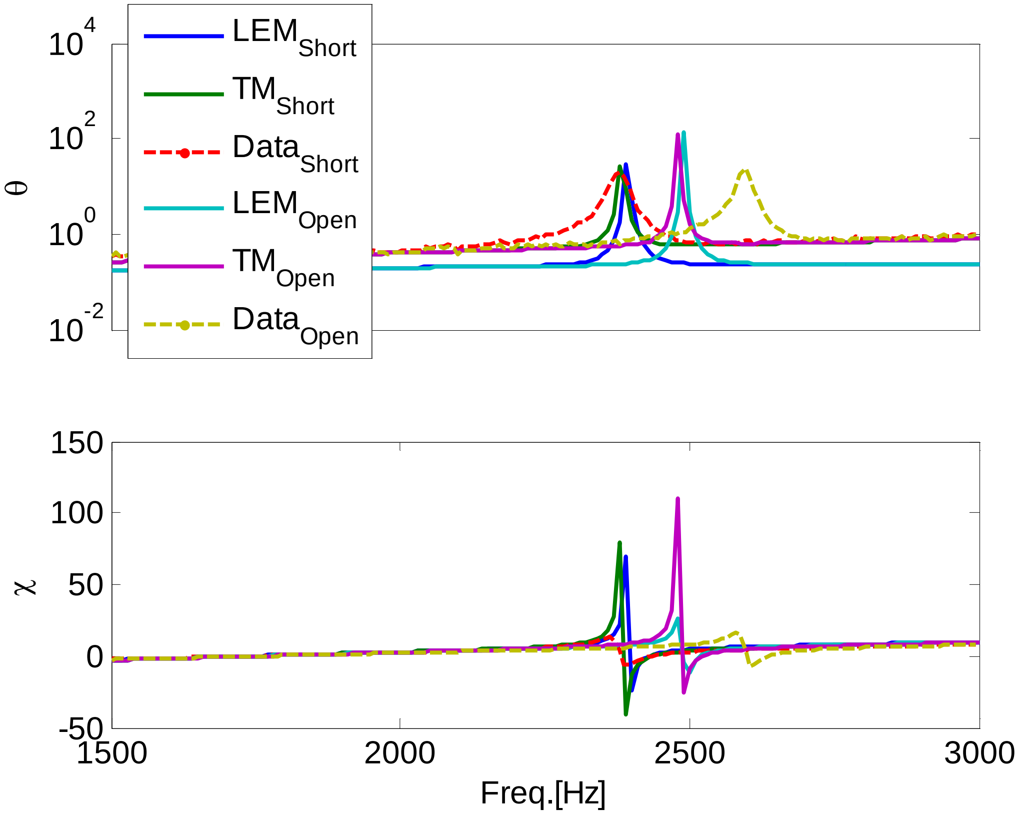

Figure 16. Comparison LEM, TR and measurement results for a short- and open-circuited EMHR (CASE I), the damping loss of the backplate is assumed to be acoustic radiation resistance

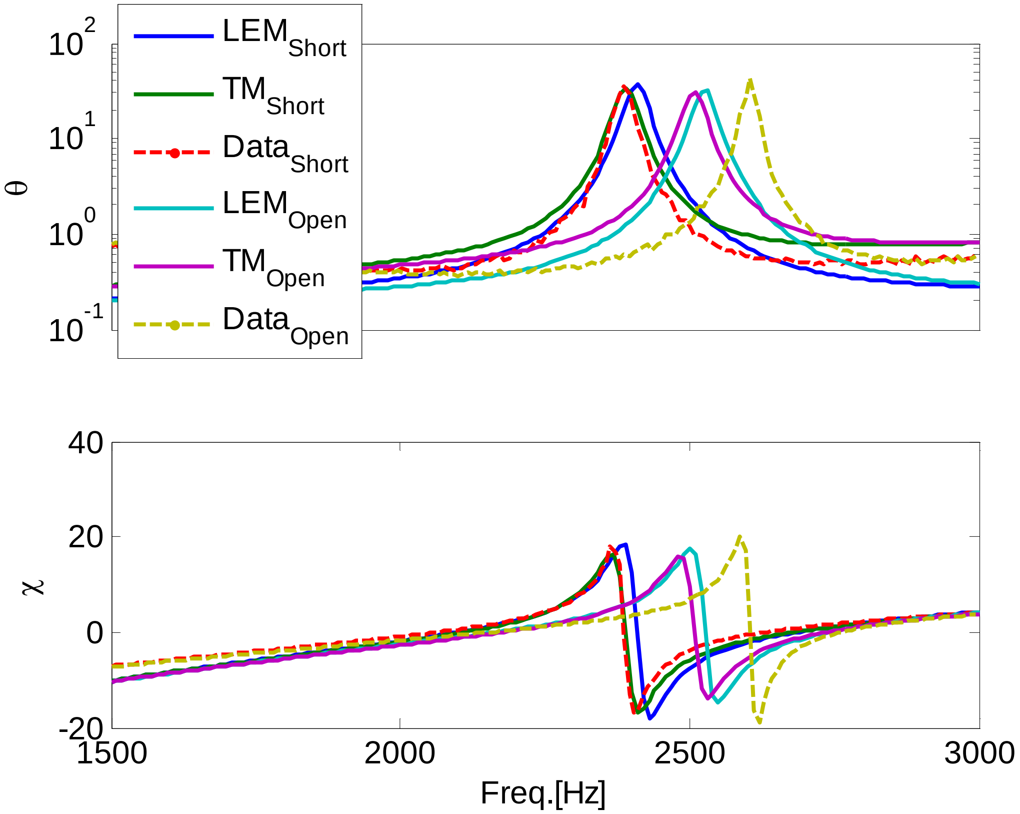

Figure 17. Comparison LEM, TR and measurement results for a short- and open-circuited EMHR (CASE II), the damping loss of the backplate is determined using logarithm decrement method ($\zeta = 0.015$).

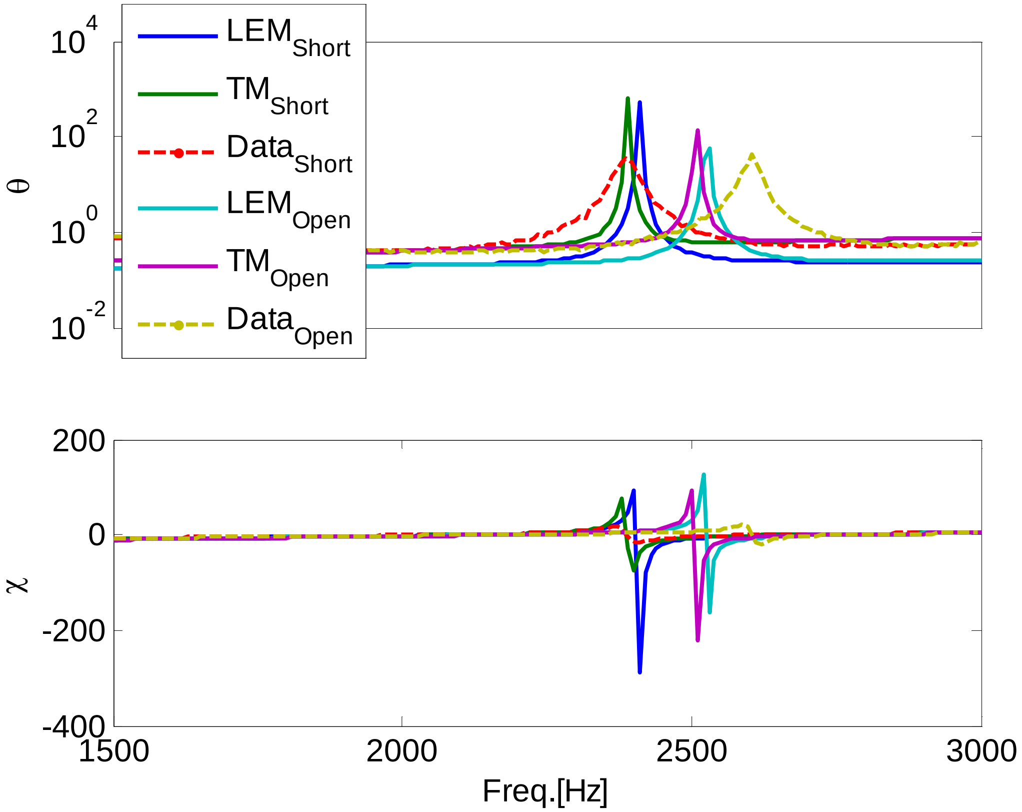

Figure 18. Comparison LEM, TR and measurement results for a short- and open-circuited EMHR (CASE II), the damping loss of the backplate is assumed to be acoustic radiation resistance.

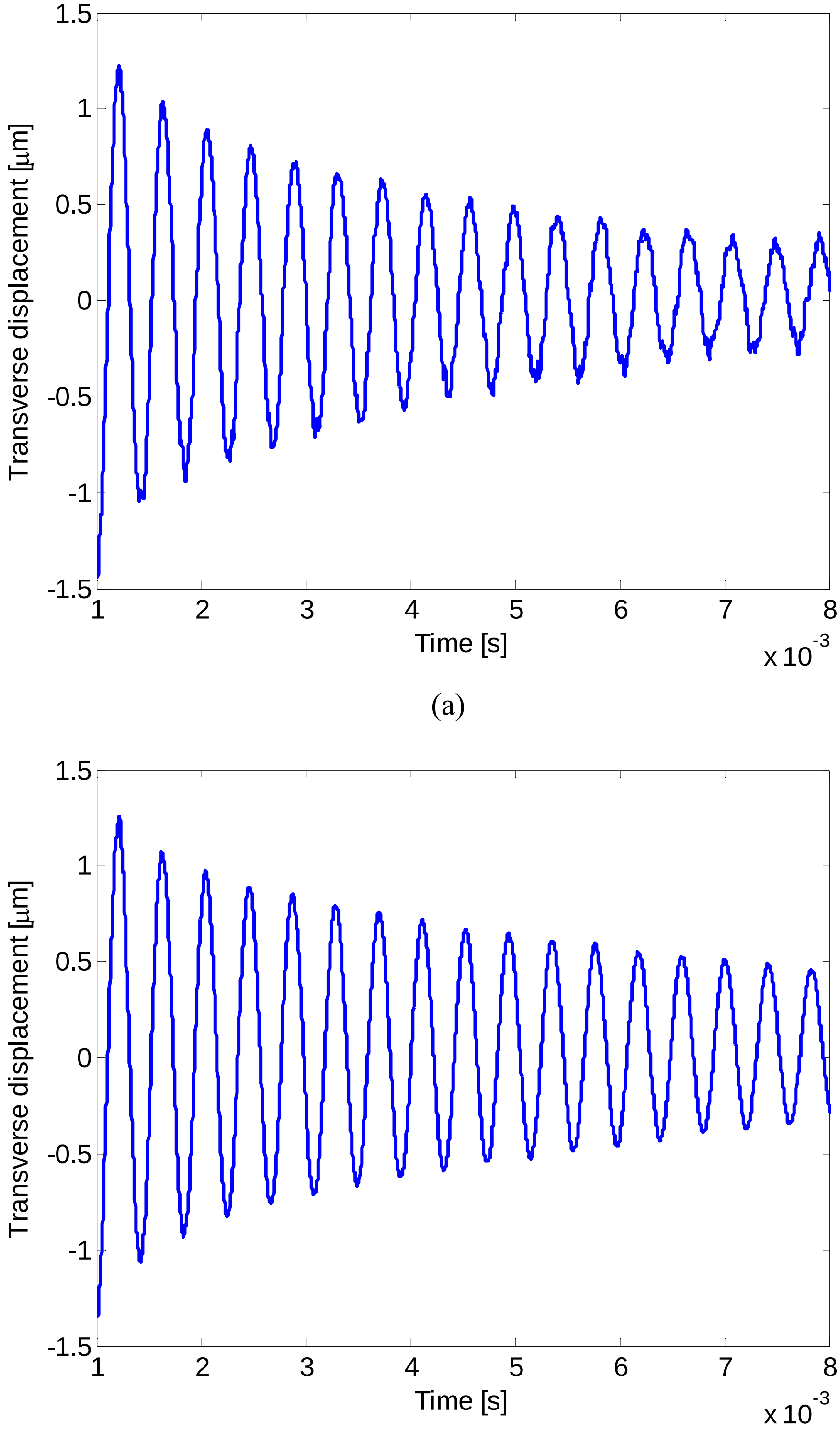

(a)

(b)

Figure 19. Damping coefficient measurement for piezoelectric composite backplate (Case I) (a) in air (b) in vacuum chamber

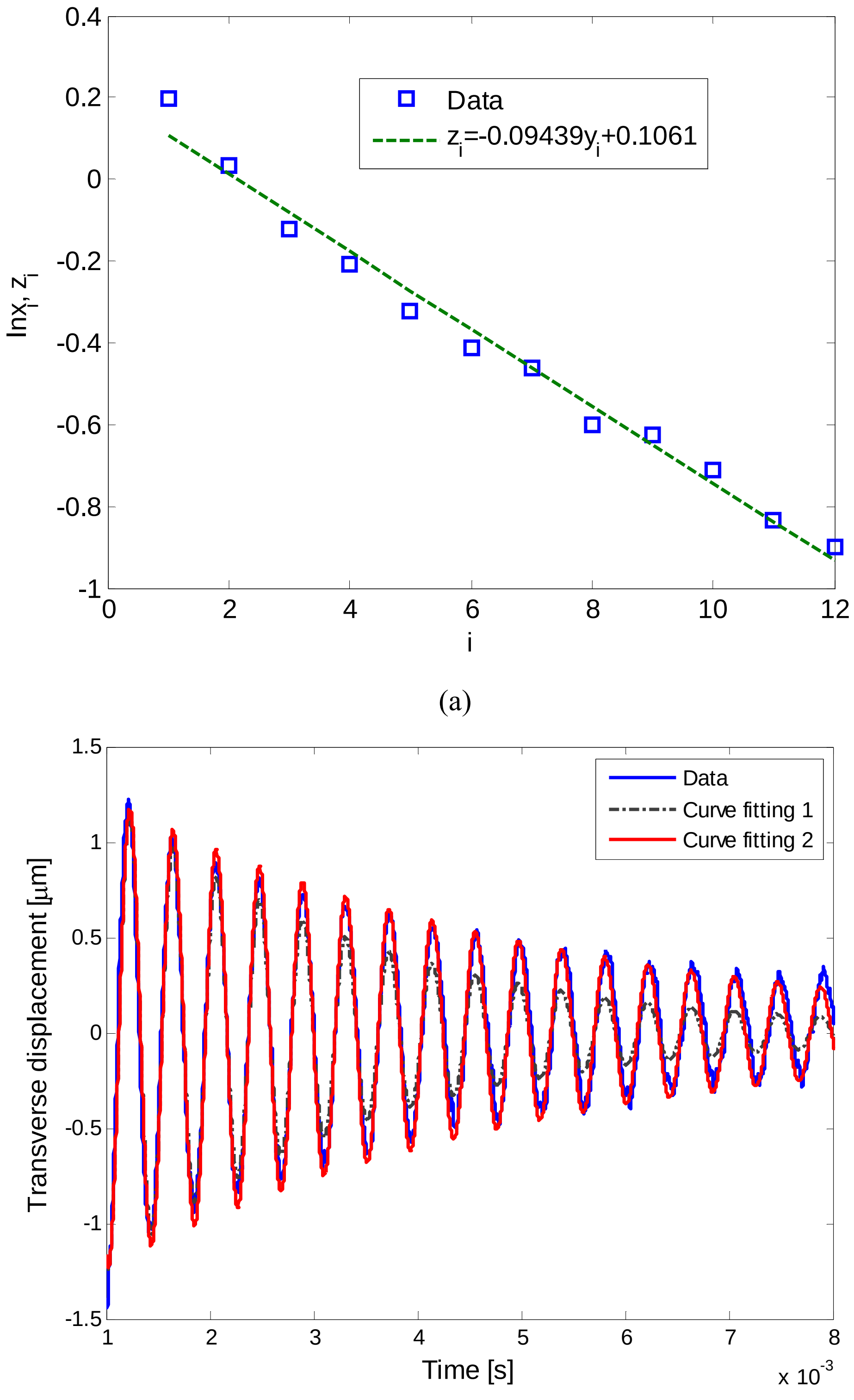

(a)

(b)

Figure 20. (a) Curve fitting the measurement data (in air) using a 2nd-order system, fitting 1- $\zeta = 0.026$, fitting 2- $\zeta = 0.015$. (b) Determination of damping coefficient of the PZT plate in air

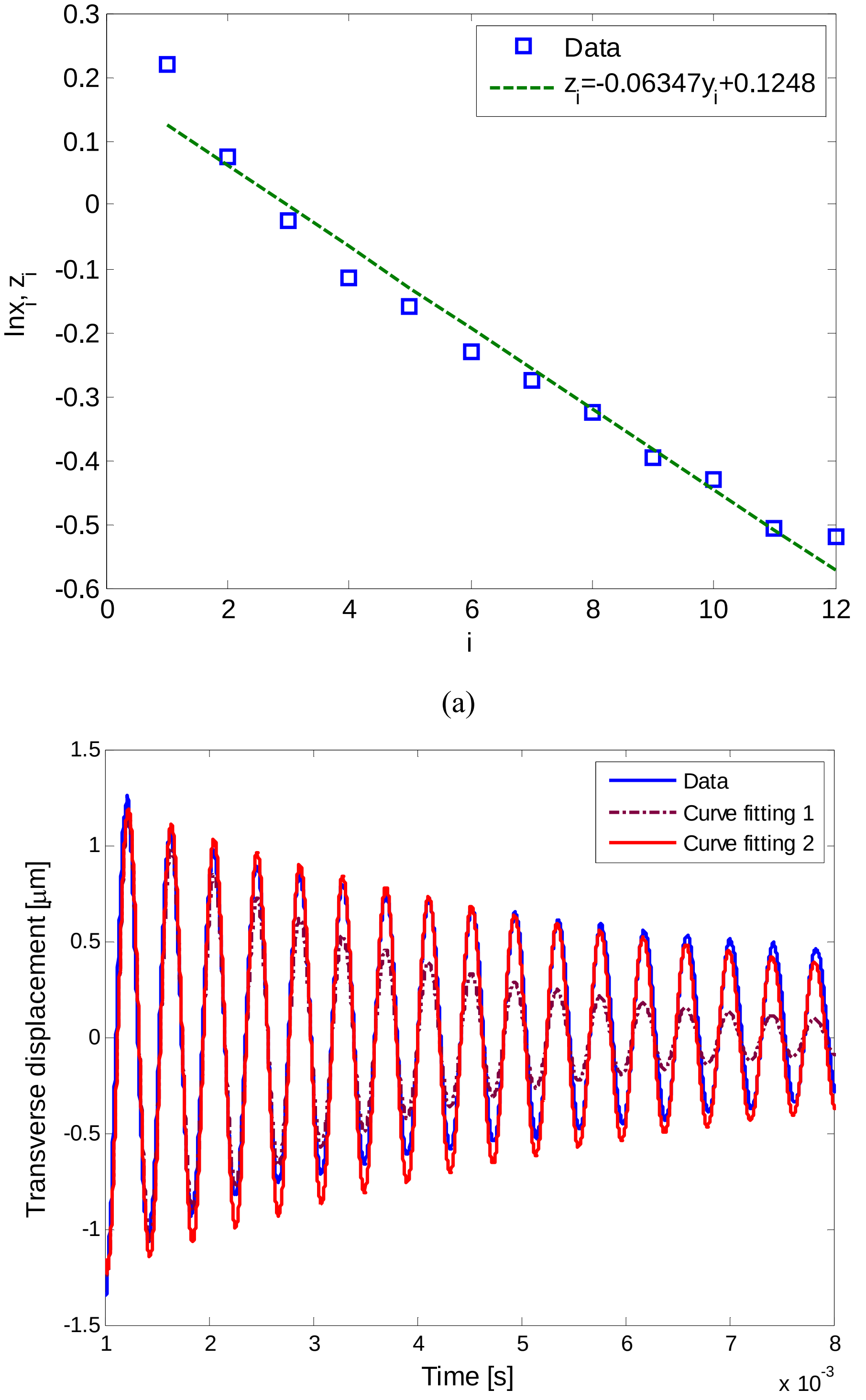

(a)

(b)

Figure 21. (a) Curve fitting the measurement data (in air) using a 2nd-order system, fitting 1- $\zeta = 0.024$, fitting 2- $\zeta = 0.01$. (b) Determination of damping coefficient of the PZT plate in air

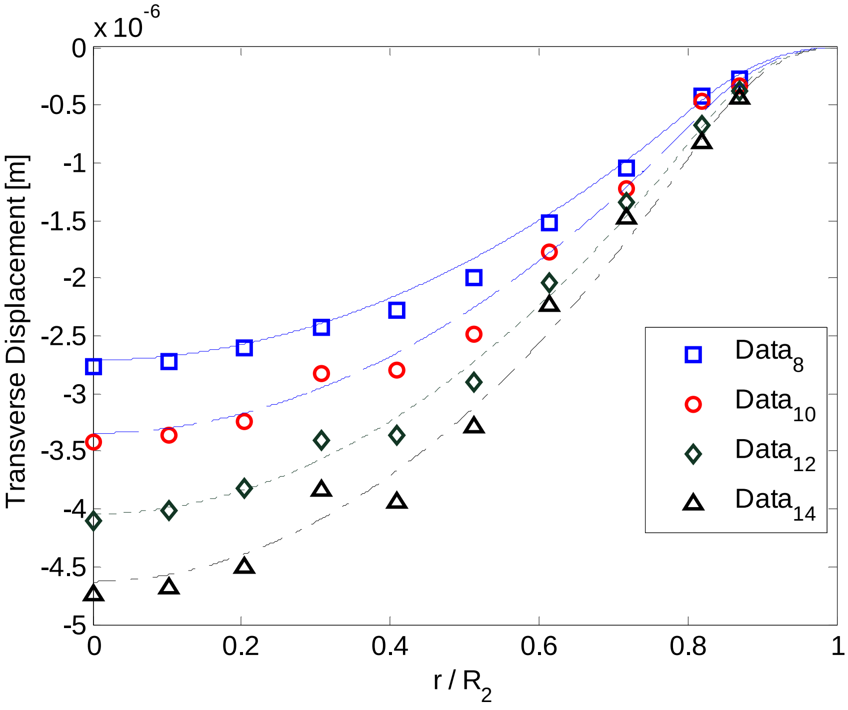

(a)

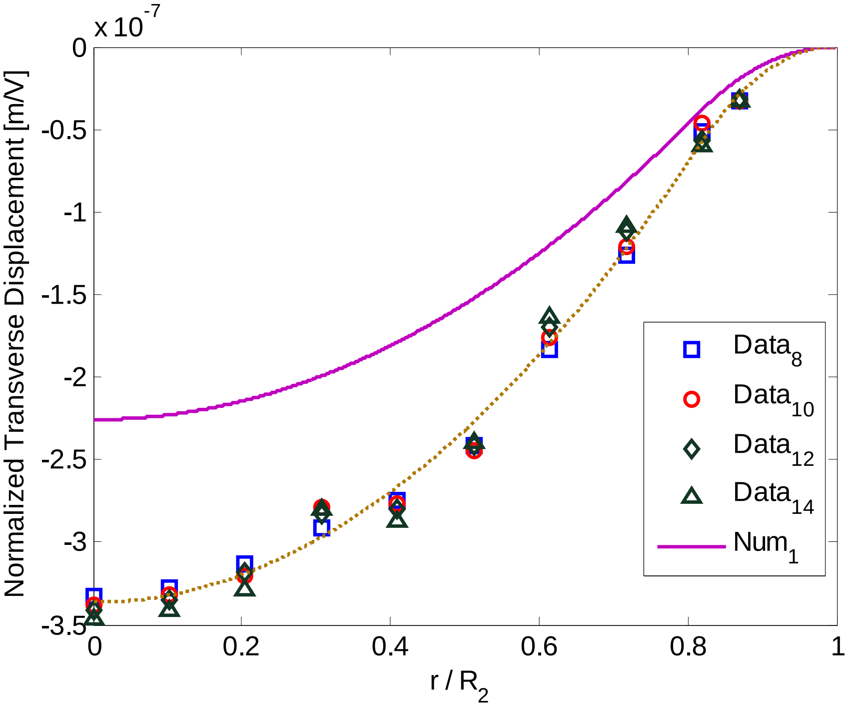

(b)

Figure 22. Measured transverse displacement of the piezoelectric backplate due to the application of various voltages.

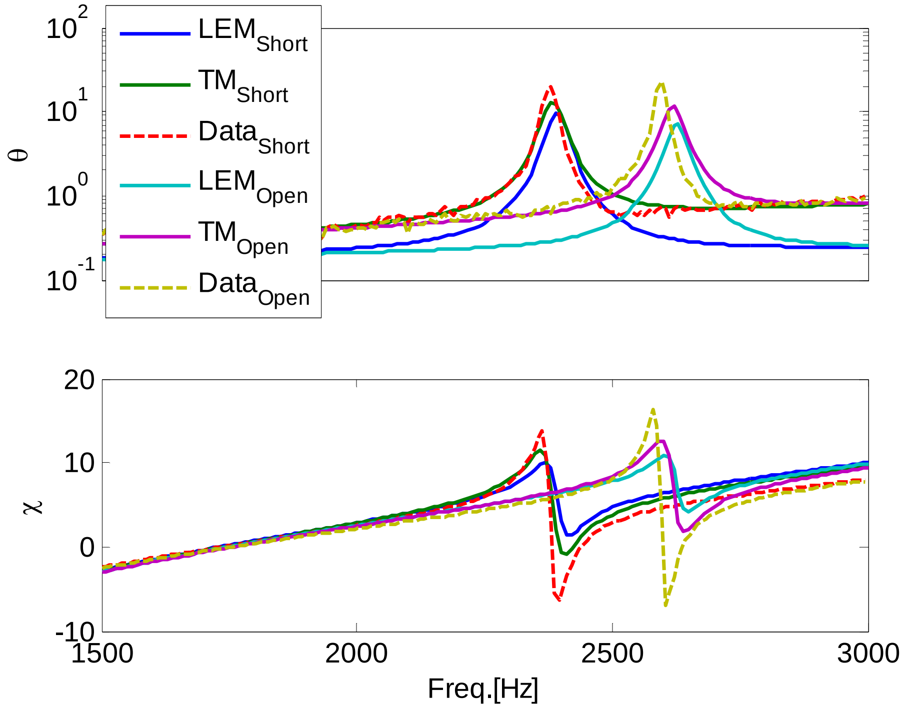

(a)

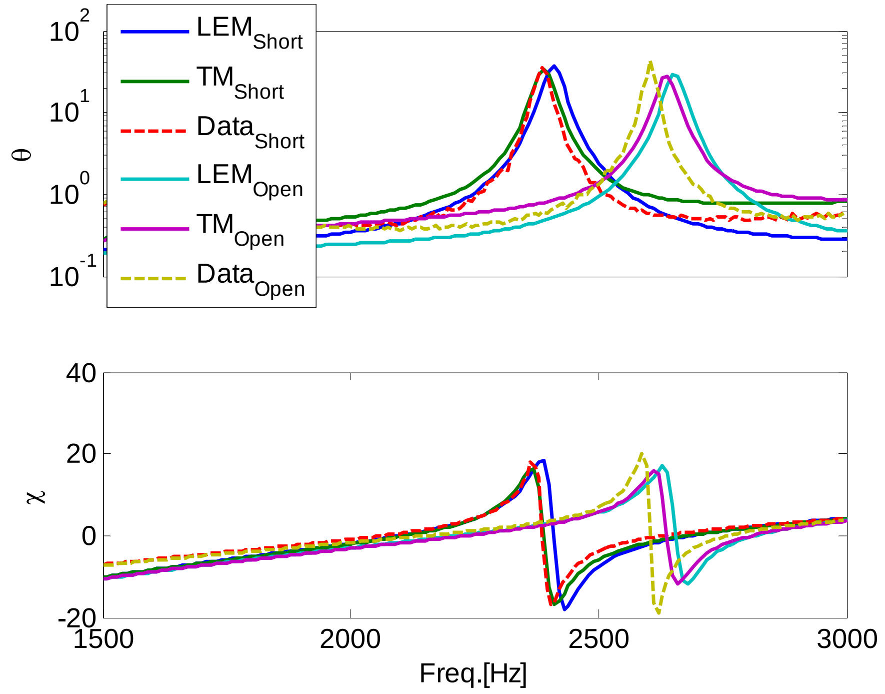

(b)

Figure 23. Predictions of the LEM and TM for short- and open-circuited EMHRs. (a) EMHR (Case I). (b) EMHR (Case II).

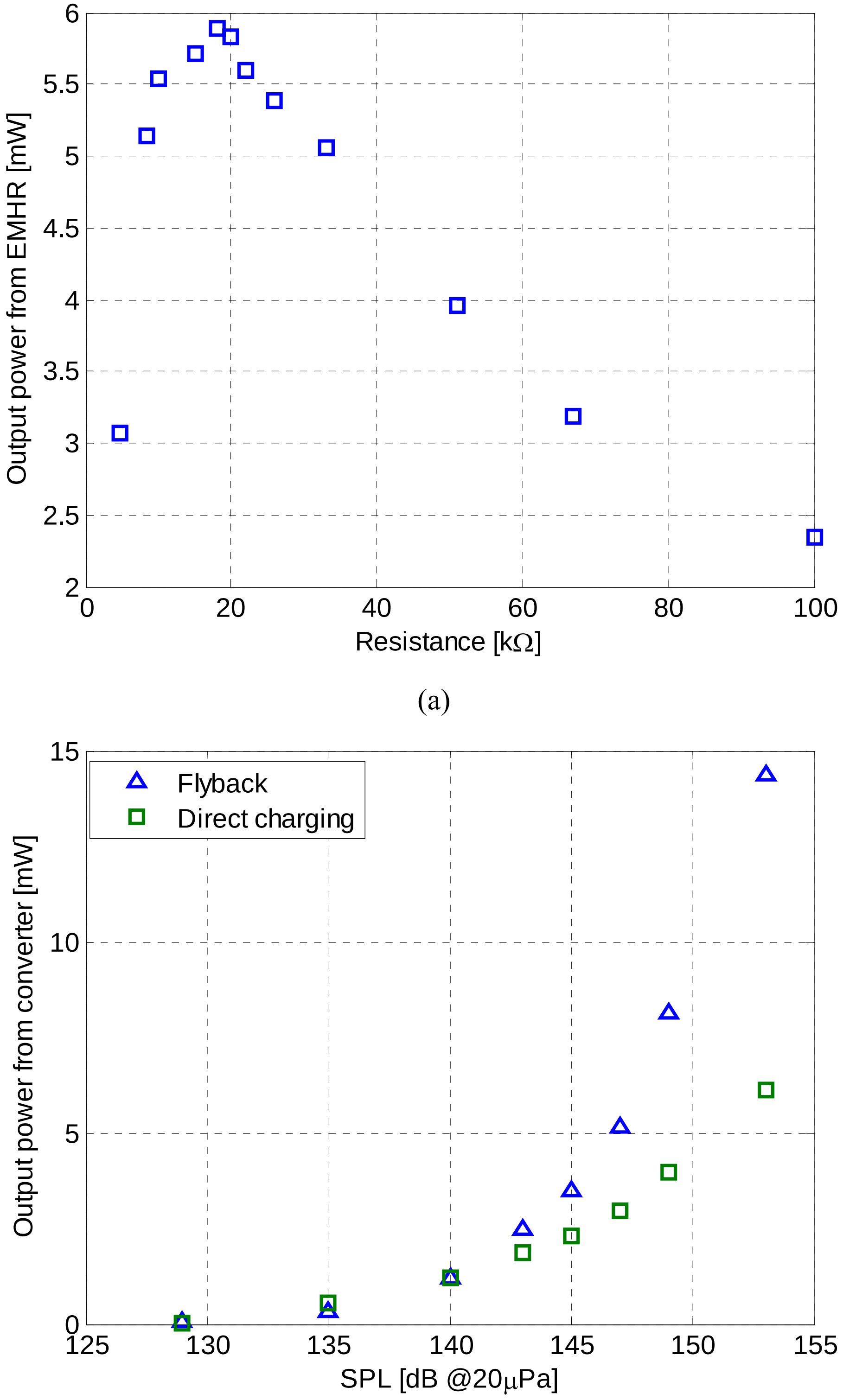

(a)

(b)

Figure 24. (a) Power delivered by the Helmholtz resonator to a resistive load. (b) Output power versus incident pressure for the flyback circuit and direct charging method.

Appendix A. Parameters Estimation for LEM of the Piezoelectric Composite Diaphragm

Equation Chapter (Next) Section 1

The extraction of the model parameters for the piezoelectric backplate is more complex due to composite plate mechanics. The piezoelectric backplate consists of an axisymmetric piezoceramic of radius R_1 and thickness h_p bonded in the center of a metal shim of radius R_2 and thickness h_s. Up to and just beyond the first resonant mode, the one-dimensional piezoelectric electroacoustic coupling is given by [18]

$$\begin{Bmatrix} \Delta\forall \\ q \end{Bmatrix} = \begin{Bmatrix} C_{aD} & d_a \\ d_a & C_{eF} \end{Bmatrix} \begin{Bmatrix} P \\ V \end{Bmatrix}, \tag{A-1}$$

where $\Delta\forall$ is the volume displacement of the piezoelectric backplate due to the application of the pressure P and voltage V. Additionally, q is the charge stored on the piezoelectric electrodes, d_a is the effective acoustic piezoelectric coefficient, and C_{eF} is the electrical free capacitance of the piezoelectric material. The volume displacement is calculated by integrating the transverse displacement, $w(r)$, over the whole plate

$$\Delta\forall = \int_0^{R_2} 2\pi r w(r) dr . \tag{A-2}$$

Thus, the short-circuit acoustic compliance of the backplate, C_{aD}, is determined by

$$C_{aD} = \left.\frac{\Delta V}{P}\right|_{V=0} = \left.\frac{\int_0^{R_2} 2\pi r w(r) dr}{P}\right|_{V=0} . \tag{A-3}$$

Similarly, the effective acoustic piezoelectric coefficient, d_A, is determined by application of voltage to the free piezoelectric plate

$$d_A = \left.\frac{\Delta V}{V}\right|_{P=0} = \left.\frac{\int_0^{R_2} 2\pi r w(r) dr}{V}\right|_{P=0} . \tag{A-4}$$

The impedance transformer factor, ϕ, is

$$\phi = \frac{-d_A}{C_{aD}}. \tag{A-5}$$

The effective acoustic mass of the piezoelectric backplate, M_{aD}, is found by equating the total distributed kinetic energy stored in the velocity of the plate to a lumped mass as[18]

$$M_{aD} = \frac{2\pi}{\Delta V} \int_0^{R_2} \rho_A \left(w(r) \right)^2 r dr \Bigg|_{V=0} , \tag{A-6}$$

where ρ_A is the area density of the piezoelectric backplate. The blocked electrical capacitance, C_{eB} , is related to the free electrical capacitance of the piezoelectric backplate, C_{EF} , as

$$C_{eB} = C_{EF} \left(1-\kappa^2\right) = \frac{\varepsilon_r \varepsilon_0 \pi R_1^2}{h_p} \left(1-\kappa^2\right), \tag{A-7}$$

where ε_r is the relative dielectric constant of the piezoelectric material, ε_0 is the permittivity of free space, R_1 is the radius of the piezoceramic, and h_p is the thickness of the piezoceramic, and κ^2 is the electroacoustic coupling factor and given by

$$\kappa^2 = \frac{d_A^2}{C_{EF} C_{aD}} . \tag{A-8}$$

The acoustic resistance, R_{aD}, of the PZT backplate models acoustic resistance and structural damping in the backplate. The damping may arise from thermo-elastic dissipation, compliant boundaries, and other intrinsic loss mechanisms. The acoustic resistance is given by

$$R_{aD} = 2\zeta \sqrt{\frac{M_{aD} + M_{aDrad}}{C_{aD}}} \tag{A-9}$$

where ζ is an experimentally determined damping factor determined using, for example, the logarithmic decrement method.[24]

Appendix B. Capacitive and Inductive-Tuning Strategy of the EMHR

Equation Chapter 2 Section 1 Equation Section 2

Capacitive tuning of the EMHR

The EMHR with capacitive shunts is analogous to a 2DOF system with two resonant frequencies, as shown in Figure B-1. To simplify the problem without loss of generality, it is assumed that the EMHR with capacitive shunts has negligible damping.

Referring to Figure B-1a, by defining

$$C_1 = C_{aC}, \tag{B-1}$$

and

$$C_2 = \frac{\left(C_{aEB} + C_{aL}\right) C_{aD} C_{aC}}{\left(C_{aB} + C_{aL}\right) C_{aD} + \left(C_{aB} + C_{aL} + C_{aD}\right) C_{aC}}, \tag{B-2}$$

the coupling coefficients, which defines the ratio of the oscillating energy stored in the coupling elements to that stored in the total capacitance for each loop, are given by [34]

$$\kappa_1 = \frac{\left(\int Q_1 dt\right)^2 \big/ C_{aC}}{\left(\int Q_1 dt\right)^2 \big/ C_1} = \frac{C_1}{C_{aC}} = 1, \tag{B-3}$$

$$\kappa_2 = \frac{\left(\int Q_2 dt\right)^2 \big/ C_{aC}}{\left(\int Q_2 dt\right)^2 \big/ C_2} = \frac{C_2}{C_{aC}}, \tag{B-4}$$

where Q_i is volume velocity, as shown in Figure B-1 . Hence, the impedance of loop 1 is

$$\begin{aligned} Z_{L1} &= R_{aN} + j\left(\omega M_{aN} - \frac{1}{\omega C_{aC}}\right) \\ &= R_{aN} + j\sqrt{\frac{M_{aN}}{C_{aC}}}\left(\omega\sqrt{M_{aN} C_{aC}} - \frac{1}{\omega\sqrt{M_{aN} C_{aC}}}\right), \\ &= Z_{wL1}\left\{\frac{R_{aN}}{Z_{L1}} + j\left(\frac{\omega}{\omega_{L1}} - \frac{\omega_{L1}}{\omega}\right)\right\} \\ &= Z_{wL1}\left\{\Delta_{L1} + j\Omega_{L1}\right\} \end{aligned} \tag{B-5}$$

where the quantity

$$\omega_{L1} = 1 \big/ \sqrt{M_{aN} C_{aC}} \tag{B-6}$$

is the resonant frequency of the loop 1. Next,

$$\Delta_{L1} = R_{aN} \Big/ \sqrt{M_{aN}/C_{aC}} \tag{B-7}$$

is the dissipation factor, which is the ratio of the power dissipated to the power stored. The quantity

$$\Omega_{L1} = \omega/\omega_{L1} - \omega_{L1}/\omega \tag{B-8}$$

is the tuning factor which measures the deviation of the operating frequency of loop 1 from its resonant frequency. Finally, The quantity

$$Z_{wL1} = \sqrt{M_{aN}/C_{aC}} \tag{B-9}$$

is a weighting factor by which the magnitude of the impedance of a different system which has the same dissipation factor and the resonant frequency differs from each other.

Similarly, the impedance of the second loop is

$$Z_{L2} = Z_{wL2}\left\{\frac{R_{aDrad}}{Z_{wL2}} + j\left[\frac{\omega}{\omega_{L2}} - \frac{\omega_{L2}}{\omega}\right]\right\} = Z_{wL2}\left(\Delta_{L2} + j\Omega_{L2}\right), \tag{B-10}$$

where the definitions of the quantities ω_{L2} , Z_{wL2} , Δ_{L2} and Ω_{L2} are similar as their counterparts in loop 1

$$\omega_{L2} = 1\Big/\sqrt{\left(M_{aD} + M_{aDrad}\right)C_2}\,, \tag{B-11}$$

$$\Delta_{L2} = R_{aDrad}\Big/\sqrt{\left(M_{aD} + M_{aDrad}\right)/C_2}\,, \tag{B-12}$$

$$\Omega_{L2} = \omega/\omega_2 - \omega_2/\omega\,, \tag{B-13}$$

and

$$Z_{wL2} = \sqrt{\left(M_{aD} + M_{aDrad}\right)/C_2}\,. \tag{B-14}$$

Next, for the coupled system

$$P = Z_1 Q_1 + \frac{1}{j\omega C_{aC}} Q_2\,, \tag{B-15}$$

and

$$0 = Z_2 Q_2 + \frac{1}{j\omega C_{aC}} Q_1\,, \tag{B-16}$$

which leads to

$$Z_{aIN} = \frac{P}{Q_1} = Z_{L1} - \frac{1}{Z_{L2}}\left(\frac{1}{j\omega C_{aC}}\right)^2. \tag{B-17}$$

From Eqs. (B-5), (B-10) and (B-17), one has

$$\frac{Z_{aIN}}{Z_{wL1}} = \Delta_{L1} + j\Omega_{L1} - \frac{1}{Z_{wL1}Z_{wL2}}\left(\frac{1}{j\omega C_{aC}}\right)^2 \frac{1}{\Delta_{L2} + j\Omega_{L2}}. \tag{B-18}$$

- If the system is undamped or weak damped,

$$\Delta_{L1} = \Delta_{L2} = 0. \tag{B-19}$$

Thus, Eq. (B-18) is rewritten as

$$\begin{aligned} &\frac{Z_{aIN}}{Z_{wL1}} \\ &= j\Omega_1 - \frac{1}{Z_{wL1}Z_{wL2}}\left(\frac{1}{j\omega C_{aC}}\right)^2 \frac{1}{j\Omega_{L2}} = j\left(\frac{\omega}{\omega_{L1}} - \frac{\omega_{L1}}{\omega}\right) + \frac{\omega_{L1}\omega_{L2}}{\omega^2}\kappa^2 \frac{1}{j\left(\frac{\omega}{\omega_{L2}} - \frac{\omega_{L2}}{\omega}\right)} \end{aligned} \text{,(B-20)}$$

where $\kappa^2 = C_1 C_2 / C_{aC}^2 = \kappa_1 \kappa_2$ is the coupling factor of the system. At the resonant frequency, Eq. (B-20) equals zero, and the solution for the resonant frequencies is

$$\omega_{1,2}^2 = \frac{\left(\omega_{L1}^2 + \omega_{L2}^2\right) \pm \sqrt{\left(\omega_{L1}^2 + \omega_{L2}^2\right)^2 - 4\left(1-\kappa^2\right)\left(\omega_{L1}\omega_{L2}\right)^2}}{2}. \tag{B-21}$$

Furthermore, Eqs. (B-6) and (B-11) yields

$$\begin{aligned} &\omega_{L1}^2 + \omega_{L2}^2 \\ &= \frac{1}{M_{aN}C_{aC}} + \frac{1}{\left(M_{aD} + M_{aDrad}\right)C_2} \\ &= \left[\frac{1}{M_{aN}} + \frac{1}{M_{aD} + M_{aDrad}}\right]\frac{1}{C_{aC}} + \frac{C_{aB} + C_{aL} + C_{aD}}{\left(M_{aD} + M_{aDrad}\right)\left(C_{aB} + C_{aL}\right)C_{aD}}, \\ &= \frac{1}{M_{aN}C_{aC}}\left(1+\alpha\right) + \frac{C_{aB} + C_{aL} + C_{aD}}{\left(M_{aD} + M_{aDrad}\right)\left(C_{aB} + C_{aL}\right)C_{aD}} \\ &= \left(1+\alpha\right)\omega_{HR}^2 + \omega_D^2 \end{aligned} \tag{B-22}$$

where $\alpha = M_{aN} / \left(M_{aD} + M_{aDrad}\right)$ is the mass ratio between the neck and piezoelectric backplate. In addition,

$$\omega_{HR} = \sqrt{\frac{1}{M_{aN}C_{aC}}} \tag{B-23}$$

is the resonant frequency of the Helmholtz resonator with solid wall instead of a piezoelectric backplate, and

$$\omega_D = \sqrt{\frac{C_{aEB} + C_{aL} + C_{aD}}{\left(M_{aD} + M_{aDrad}\right)\left(C_{aB} + C_{aL}\right)C_{aD}}} \tag{B-24}$$

is the resonant frequency of the piezoelectric backplate. Similarly,

$$\omega_{L1}^2 - \omega_{L2}^2 = \left(1-\alpha\right)\omega_{HR}^2 - \omega_D^2 \tag{B-25}$$

- If the system is weakly coupled, $\kappa \to 0$, substitution of Eqs. (B-22) and (B-25) into (B-21) results in

$$\begin{aligned}\omega_{1,2} &= \sqrt{\frac{\left(1+\alpha\right)\omega_{HR}^2 + \omega_D^2 \pm \sqrt{\left[\left(1-\alpha\right)\omega_{HR}^2 - \omega_D^2\right]^2}}{2}} \\ &= \begin{cases} \omega_{HR} \\ \sqrt{\omega_D^2 + \alpha\omega_{HR}^2} \end{cases}\end{aligned}. \tag{B-26}$$

- If the mass ratio between the neck and the piezoelectric backplate is very small, $\alpha \to 0$,

$$\begin{aligned}\omega_{1,2} &= \sqrt{\frac{\omega_{HR}^2 + \omega_D^2 \pm \sqrt{\left[\omega_{HR}^2 - \omega_D^2\right]^2}}{2}} \\ &= \begin{cases} \omega_{HR} \\ \omega_D \end{cases}\end{aligned}. \tag{B-27}$$

In other words, the resonant frequencies of a lightly damped EMHR with capacitive shunts possessing weak coupling are approximately the resonant frequency of the solid-walled Helmholtz resonator and the piezoelectric backplate. As indicated by Eq.(B-24) , the resonant frequency of the piezoelectric backplate is adjusted with the change of the capacitive loads

  - Open-circuit , $C_{aL} = 0$ or $Z_{aL} = 1/sC_{aL} \to \infty$

$$\left[\omega_D\right]_{\text{open}} = \sqrt{\frac{C_{aEB} + C_{aD}}{\left(M_{aD} + M_{aDrad}\right)C_{aEB}C_{aD}}}. \tag{B-28}$$

  - Short-circuit, $C_{aL} = \infty$ or $Z_{aL} = 1/sC_{aL} \to 0$

$$\left[\omega_D\right]_{\text{short}} = \sqrt{\frac{1}{\left(M_{aD} + M_{aDrad}\right)C_{aD}}}. \tag{B-29}$$

- Capacitive load, $C_{aL} = \phi^2 / C_{eL}$

$$\left[\omega_D\right]_{\text{capacitive}} = \frac{C_{aEB} + C_{aL} + C_{aD}}{\left(M_{aD} + M_{aDrad}\right)\left(C_{aEB} + C_{aL}\right) C_{aD}} . \tag{B-30}$$

Clearly,

$$\left[\omega_D\right]_{\text{short}} < \left[\omega_D\right]_{\text{capacitive}} < \left[\omega_D\right]_{\text{open}} . \tag{B-31}$$

or by the use of Eq. (B-27)

$$\left[\omega_2\right]_{\text{short}} < \left[\omega_2\right]_{\text{capacitive}} < \left[\omega_2\right]_{\text{open}} . \tag{B-32}$$

Eq. (B-32) demonstrates how the tunable electromechanical Helmholtz resonator works with different capacitive shunts. The short and open loads define the limits of tuning using capacitive loads. The second resonant frequency shifts toward the short case when the capacitance increases. It is worthy to note that the aforementioned analysis focuses on the capacitive tuning behavior of the EMHR with weak coupling. In fact, when such coupling is not weak, the first resonant frequency of the system can be tuned *in-situ* as well, as indicated by Eq.(B-21).

Inductive tuning of the EMHR

As shown in Figure B-1c, The EMHR with inductive loads is a 3DOF system. Similarly, to simplify the problem without loss of generality, it is assumed that the EMHR with inductive shunts has negligible damping. The effective impedance of loop 3 is thus given by

$$Z_{L3} = \frac{\left[\phi^2 / \left(j\omega C_{eB}\right)\right] j\omega\phi^2 M_{eL}}{\left[\phi^2 / \left(j\omega C_{eB}\right)\right] + j\omega\phi^2 M_{eL}} \tag{B-33}$$

which can be further approximated as

$$Z_{L3} \approx j\omega\phi^2 M_{eL} \tag{B-34}$$

with the assumption

$$\omega^2 C_{eB} M_{eL} << 1 , \tag{B-35}$$

Or

$$\omega \ll \frac{1}{\sqrt{C_{eB} M_{eL}}} = \omega_E , \tag{B-36}$$

where ω_E is the resonant frequency of the loop 3. Eq. (B-36) is satisfied for the EMHR and the frequency range investigated in this project. Physically, loop 3 effectively adds a mass $\phi^2 M_{eL}$ to loop 2. Similarly, the resonant frequencies of the weakly coupled EMHR are given by

$$\omega_{1,2} \approx \sqrt{\frac{\omega_{HR}^2 + \omega_D^2 \pm \sqrt{\left[\omega_{HR}^2 - \omega_D^2\right]^2}}{2}} = \begin{cases} \omega_{HR} \\ \omega_D \end{cases}, \tag{B-37}$$

where ω_{HR} is given by Eq. (B-23), while ω_D is

$$\omega_D = \sqrt{\frac{1}{\left(M_{aD} + M_{aDrad} + \phi^2 M_{eL}\right) C_{aD}}}. \tag{B-38}$$

Clearly, $\omega_D \le \left[\omega_D\right]_{\text{short}}$ in Eq. (B-29). With increasing inductive loads, ω_D moves further away from the short-circuit resonant frequency $\left[\omega_D\right]_{\text{short}}$.

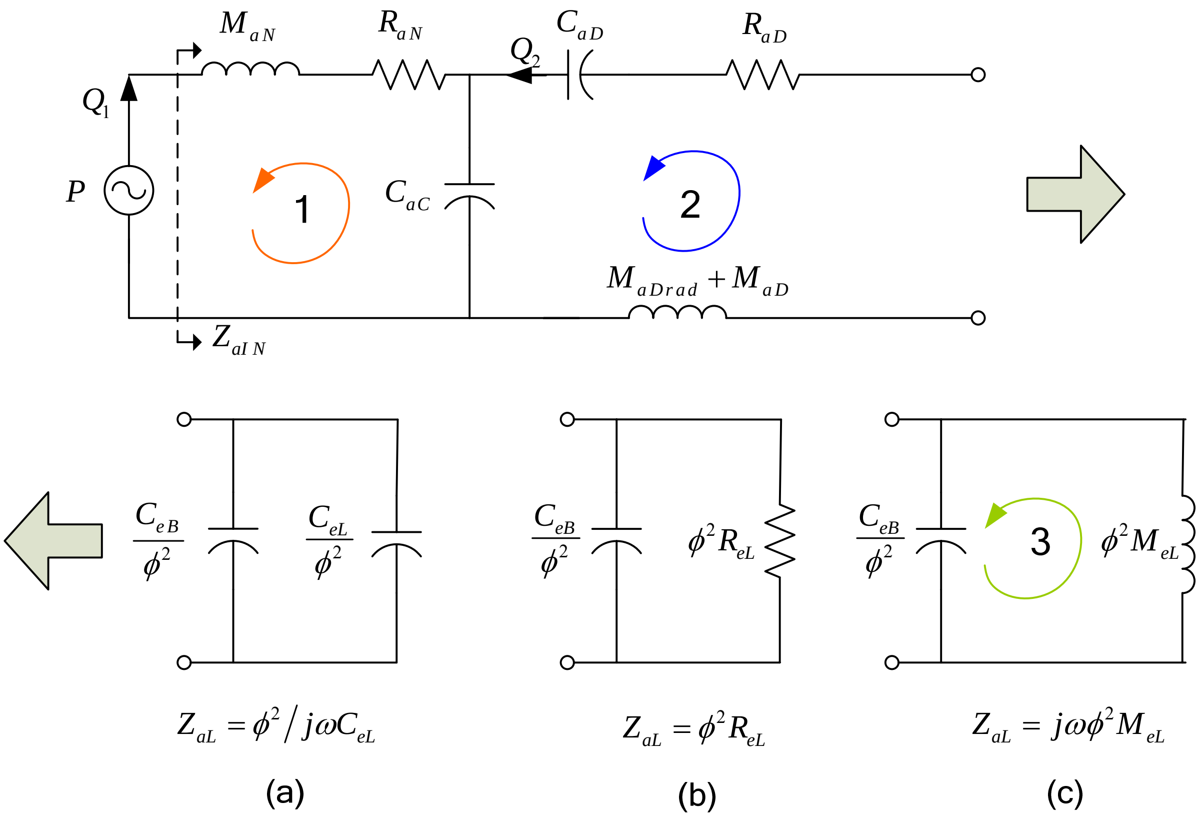

Figure B-1. EMHR with passive electrical loads is analogous to a 2DOF system for (a) capacitive and (b) resistive loads and a 3DOF system with an (c) inductive load.

Appendix C. Development of Transfer Matrix of the EMHR

Equation Section (Next)

Area contraction

The area contraction is shown in Figure C-1a. Due to abrupt change of the area, even with the planar incident wave, evanescent higher order acoustic modes will be excited in the vicinity of the discontinuity, thus the acoustic field near the discontinuity will have a transverse component. Such effect can be taken into account in terms of plane wave variables by means of an additional mass and resistance.[35, 36] Following Karal and Ingard, the relation between the acoustic variables for the area contraction is given by

$$P_5 = P_4 + \left(\rho_0 c_0 \zeta_4 / A_4\right) U_4 A_4 , \tag{C-1}$$

$$\rho_0 c_0 U_5 A_5 = \rho_0 c_0 U_4 A_4 \tag{C-2}$$

where P_4 and P_5 are the plane wave pressure component in before and after the discontinuity. Eqs. (C-1) and (C-2) represent the continuity of the pressure and the volume velocity across the discontinuity, respectively. The matrix representation for the area contraction is thus given by,

$$\begin{bmatrix} P_5 \\ \rho_0 c_0 U_5 \end{bmatrix} = \begin{bmatrix} 1 & \zeta_4 \\ 0 & A_4/A_5 \end{bmatrix} \begin{bmatrix} P_4 \\ \rho_0 c_0 U_4 \end{bmatrix}, \tag{C-3}$$

where $A_4 = \pi r^2$ is the cross-sectional area of the neck of the Helmholtz resonator, $A_5 = D_{tube}^2$ is the cross-sectional area of the tube, and ζ_4 is the normalized specific acoustic impedance, which is given by [36]

$$\zeta_4 = \frac{1}{\rho_0 c_0}\left(\sqrt{2\mu\rho_0\omega} + \frac{\rho_0 \omega^2 A_4}{2\pi c_0}\right) + \frac{j8kr}{3\pi} . \tag{C-4}$$

Thus, the transfer matrix for the area contraction is given by

$$T_{AC} = \begin{bmatrix} 1 & \zeta_4 \\ 0 & A_4/A_5 \end{bmatrix} . \tag{C-5}$$

Area expansion

Similarly, the relationship between the acoustic variables for the area expansion, shown in Figure C-1b, is given by [36]

$$P_3 = P_2 + \left(\rho_0 c_0 \zeta_3 / A_3\right) U_2 A_2 , \tag{C-6}$$

$$\rho_0 c_0 U_3 A_3 = \rho_0 c_0 U_2 A_2 , \tag{C-7}$$

or in transfer matrix form,

$$\begin{bmatrix} P_3 \\ \rho_0 c_0 U_3 \end{bmatrix} = \begin{bmatrix} 1 & (A_2/A_3)\zeta_3 \\ 0 & A_2/A_3 \end{bmatrix} \begin{bmatrix} P_2 \\ \rho_0 c_0 U_2 \end{bmatrix}, \tag{C-8}$$

where $A_3 = \pi r^2$ is the cross-sectional area of the neck of Helmholtz resonator, $A_2 = \pi R^2$ is the cross-sectional area of the cavity, and ζ_3 is the normalized specific acoustic impedance, which is given by

$$\zeta_3 = \frac{1}{\rho_0 c_0}\left(\sqrt{2\mu\rho_0\omega} + \frac{\rho_0 \omega^2 A_3}{2\pi c_0}\right) + \frac{j8kr}{3\pi} . \tag{C-9}$$

Thus, the transfer matrix for the area contraction is given by

$$T_{AE} = \begin{bmatrix} 1 & (A_2/A_3)\zeta_3 \\ 0 & A_2/A_3 \end{bmatrix} . \tag{C-10}$$

Duct element

Finding the acoustic velocity and pressure fields due to sound wave propagation in a long, round duct is a classic acoustics problem. Tijdeman reviewed this topic and showed that the solution obtained by Zwikker and Kosten has the widest range of validity.[37, 38] For plane-wave propagation in a duct with radius R, as shown in Figure C-1c, the pressure and axial velocity component are given by [37, 38]

$$P = \left(\frac{\rho_0 c_0^2}{\gamma}\right)\left(A e^{-\Gamma kx} + B e^{\Gamma kx}\right) , \tag{C-11}$$

$$U = c_0 \frac{j\Gamma}{\gamma}\left[\frac{J_0\left(j^{3/2}\eta s\right)}{J_0\left(j^{3/2} s\right)} - 1\right]\left(A e^{-\Gamma kx} - B e^{\Gamma kx}\right), \tag{C-12}$$

where Γ is the complex propagation coefficient, $k = \omega / c_0$ is the wave number, $\eta = r/R$ is dimensionless radius, $s = R\sqrt{\omega\rho/\mu}$ is the shear wave number or Stokes number, γ is the ratio of specific heats, and μ is dynamic viscosity coefficient of the air. The complex propagation coefficient is given by

$$\Gamma = \sqrt{\frac{J_0\left(j^{3/2} s\right)}{J_2\left(j^{3/2} s\right)} \frac{\gamma}{n}} , \tag{C-13}$$

where

$$n=\left(1+\frac{\gamma-1}{\gamma}\frac{J_2\left(j^{3/2}\sigma s\right)}{J_0\left(j^{3/2}\sigma s\right)}\right)^{-1}, \tag{C-14}$$

where $\sigma=\sqrt{\mu C_p/\lambda}=\sqrt{\Pr}$, Pr is Prandtl number and $J_i(\ )$ is the ith order Bessel function of first kind.

From Eq. (C-12), the mean velocity over cross-section of the duct is thus obtained by

$$\begin{aligned}\bar{U}&=\frac{1}{\pi R^2}\int_0^R U2\pi r dr\\ &=\frac{c_0\left(Ae^{-\Gamma kx}-Be^{\Gamma kx}\right)}{\pi R^2}\int_0^R\left\{\frac{j\Gamma}{\gamma}\left[\frac{J_0\left(j^{3/2}\eta s\right)}{J_0\left(j^{3/2}s\right)}-1\right]\right\}2\pi r dr\\ &=\frac{j\Gamma c_0}{\gamma}\frac{J_2\left(j^{3/2}s\right)}{J_0\left(j^{3/2}s\right)}\left(Ae^{-\Gamma kx}-Be^{\Gamma kx}\right)\\ &=\frac{c_0}{\gamma}\frac{j\gamma}{\Gamma n}\left(Ae^{-\Gamma kx}-Be^{\Gamma kx}\right)\end{aligned}, \tag{C-15}$$

where two identities of the Bessel function are used

$$J_{n-1}(z)+J_{n+1}(z)=\frac{2n}{z}J_n(z), \tag{C-16}$$

$$\int_0^a zJ_0(z)dz=aJ_1(a). \tag{C-17}$$

Thus, from Eqs. (C-11) and (C-15), one can deduce the relationship between $\left(P_2,U_2\right)$ and $\left(P_1,U_1\right)$, illustrated in Figure C-1c, as

$$\begin{bmatrix}P_2\\ \rho_0c_0\bar{U}_2\end{bmatrix}=\begin{bmatrix}\cosh(\Gamma kL) & \sinh(\Gamma kL)/G\\ G\sinh(\Gamma kL) & \cosh(\Gamma kL)\end{bmatrix}\begin{bmatrix}P_1\\ \rho_0c_0\bar{U}_1\end{bmatrix}, \tag{C-18}$$

where $G=j\gamma/\Gamma n$, Γ and n are given by Eqs. (C-13) and (C-14). The same result can be obtained for the relationship between $\left(P_2,u_2\right)$ and $\left(P_1,u_1\right)$. Thus, the transfer matrix for the duct element shown is given by

$$T_{DE}=\begin{bmatrix}\cosh(\Gamma kL) & \sinh(\Gamma kL)/G\\ G\sinh(\Gamma kL) & \cosh(\Gamma kL)\end{bmatrix}. \tag{C-19}$$

when the wave field in the duct is lossless and isentropic,

$$\Gamma = i \quad G = 1\,. \tag{C-20}$$

Eq. (C-18) can thus be simplified to

$$\begin{bmatrix} P_2 \\ \rho_0 c_0 U_2 \end{bmatrix} = \begin{bmatrix} \cos(kL) & j\sin(kL) \\ j\sin(kL) & \cos(kL) \end{bmatrix} \begin{bmatrix} P_1 \\ \rho_0 c_0 U_1 \end{bmatrix}, \tag{C-21}$$

or in the $p' - Q$ formulation

$$\begin{bmatrix} P_2 \\ Q_2 \end{bmatrix} = \begin{bmatrix} \cos(kL) & j\frac{Z_0}{S}\sin(kL) \\ j\frac{S}{Z_0}\sin(kL) & \cos(kL) \end{bmatrix} \begin{bmatrix} P_1 \\ Q_1 \end{bmatrix}. \tag{C-22}$$

The determinant of the transfer matrix of Eq. (C-22) is given by

$$\det \begin{bmatrix} \cos(kL) & j\frac{Z_0}{S}\sin(kL) \\ j\frac{S}{Z_0}\sin(kL) & \cos(kL) \end{bmatrix} = 1\,. \tag{C-23}$$

Thus the lossless isentropic duct element is a reciprocal system. Furthermore, T_{11} and T_{22} terms are real, and T_{12} and T_{21} are purely imaginary; thus this system is also conservative.

Clamped piezoelectric backplate with shunt loads

To develop the transfer matrix representation for the piezoelectric-backplate (or PZT-backplate), it is assumed that the maximum dimension of the PZT-backplate is much less than the bending wavelength of interest, and that only linear behavior of the PZT-backplate need be considered. With these assumptions, an equivalent two-port networks including a lossless transformer can be developed for the PZT-backplate, as shown in Figure C-2, where P_1 is the pressure exerting on the PZT-backplate, Q_1 is the incident volume velocity, V and I are the voltage the current at the electrical port, respectively. Associated with the two-port networks are two impedances that are measurable properties of the system

$$Z_{eB} = \left.\frac{V}{I}\right|_{Q=0} = \frac{1}{j\omega C_{eB}} : \text{ the blocked electrical impedance} \tag{C-24}$$

$$Z_{aD} = \left.\frac{P}{Q}\right|_{V=0} = R_{aD} + j\omega M_{aD} + \frac{1}{j\omega C_{aD}} \text{: the short-circuit acoustic impedance} \quad \text{(C-25)}$$

where the definition of C_{eB}, R_{aD}, M_{aD} and C_{aD} are listed in Table 1. Furthermore, the lossless transformer converts energy between the acoustical and electrical domains and obeys the transformer relations

$$I' = \phi Q_1, \quad \text{(C-26)}$$

and

$$P' = V\phi \ , \quad \text{(C-27)}$$

where ϕ is the impedance transformation factor. Hence, for two-port network shown in Figure C-2, one has

$$V = \frac{I}{j\omega C_{eB}} + \frac{\phi Q_1}{j\omega C_{eB}}, \quad \text{(C-28)}$$

$$P_1 = V\phi + Z_{aD} Q_1 . \quad \text{(C-29)}$$

Substituting Eq. (C-28) into (C-29) results in

$$P_1 = \frac{\phi I}{j\omega C_{eB}} + Z_{aD}\left(1 + \frac{\phi^2}{j\omega C_{eB}}\right) Q_1 . \quad \text{(C-30)}$$

where $Z_{aD} + \phi^2 / j\omega C_{eB}$ defines the open-circuit ($I = 0$) acoustic impedance of the PZT-backplate. One the other hand, substitution of P_1 and V for Q_1 in Eq. (C-28) from Eq. (C-29) results in

$$V = \frac{I}{j\omega C_{eB}}\left(\frac{j\omega C_{eB} Z_{aD}}{j\omega C_{eB} Z_{aD} + \phi^2}\right) + \frac{\phi P_1}{j\omega C_{eB} Z_{aD} + \phi^2}, \quad \text{(C-31)}$$

where

$$\frac{1}{C_{eB}}\left(\frac{j\omega C_{eB} Z_{aD}}{j\omega C_{eB} Z_{aD} + \phi^2}\right) = \frac{1}{C_{eB}}\left[1 - \frac{\phi^2/(j\omega C_{eB})}{Z_{aD} + \phi^2/(j\omega C_{eB})}\right] = \frac{1}{C_{eB}}\left(1 - \kappa^2\right) = \frac{1}{C_{eF}}, \quad \text{(C-32)}$$

where C_{eF} is the free electric compliance ($P_1 = 0$), and κ^2 is the coupling factor. Finally, from Eqs. (C-28) and (C-29), one has

$$P_1 = \frac{j\omega C_{eB} Z_{aD} + \phi^2}{\phi} V - \frac{Z_{aD}}{\phi} I, \quad \text{(C-33)}$$

$$Q_1 = \frac{j\omega C_{eB}}{\phi} V - \frac{1}{\phi} I \,. \tag{C-34}$$

or in the matrix form of

$$\begin{bmatrix} P_1 \\ Q_1 \end{bmatrix} = \begin{bmatrix} \dfrac{j\omega C_{eB} Z_{aD} + \phi^2}{\phi} & -\dfrac{Z_{aD}}{\phi} \\ \dfrac{j\omega C_{eB}}{\phi} & -\dfrac{1}{\phi} \end{bmatrix} \begin{bmatrix} V \\ I \end{bmatrix}. \tag{C-35}$$

Consequently, when the electrical boundary condition defined by $V/I = -Z_{eL}$ is given, the acoustic impedance, defined by P_1/Q_1, can thus be obtained for a given PZT-backplate as

$$\frac{P_1}{Q_1} = \frac{\left(j\omega C_{eB} Z_{aD} + \phi^2\right)\left(V/I\right) - Z_{aD}}{j\omega C_{eB}\left(V/I\right) - 1} = \frac{\left(j\omega C_{eB} Z_{aD} + \phi^2\right) Z_{eL} + Z_{aD}}{j\omega C_{eB} Z_{eL} + 1}. \tag{C-36}$$

The $P - \rho_0 c_0 u$ formulation of Eq. (C-35) is given by

$$\begin{bmatrix} P_1 \\ \rho_0 c_0 U_1 \end{bmatrix} = \begin{bmatrix} \dfrac{j\omega C_{eB} Z_{aD} + \phi^2}{\phi} & -\dfrac{Z_{aD}}{\phi} \\ \dfrac{j\omega \rho_0 c_0 C_{eB}}{A_D \phi} & -\dfrac{\rho_0 c_0}{A_D \phi} \end{bmatrix} \begin{bmatrix} V \\ I \end{bmatrix}, \tag{C-37}$$

where A_D is the effective area of the PZT-backplate due to the displacement of the clamped PZT-backplate is not uniform.

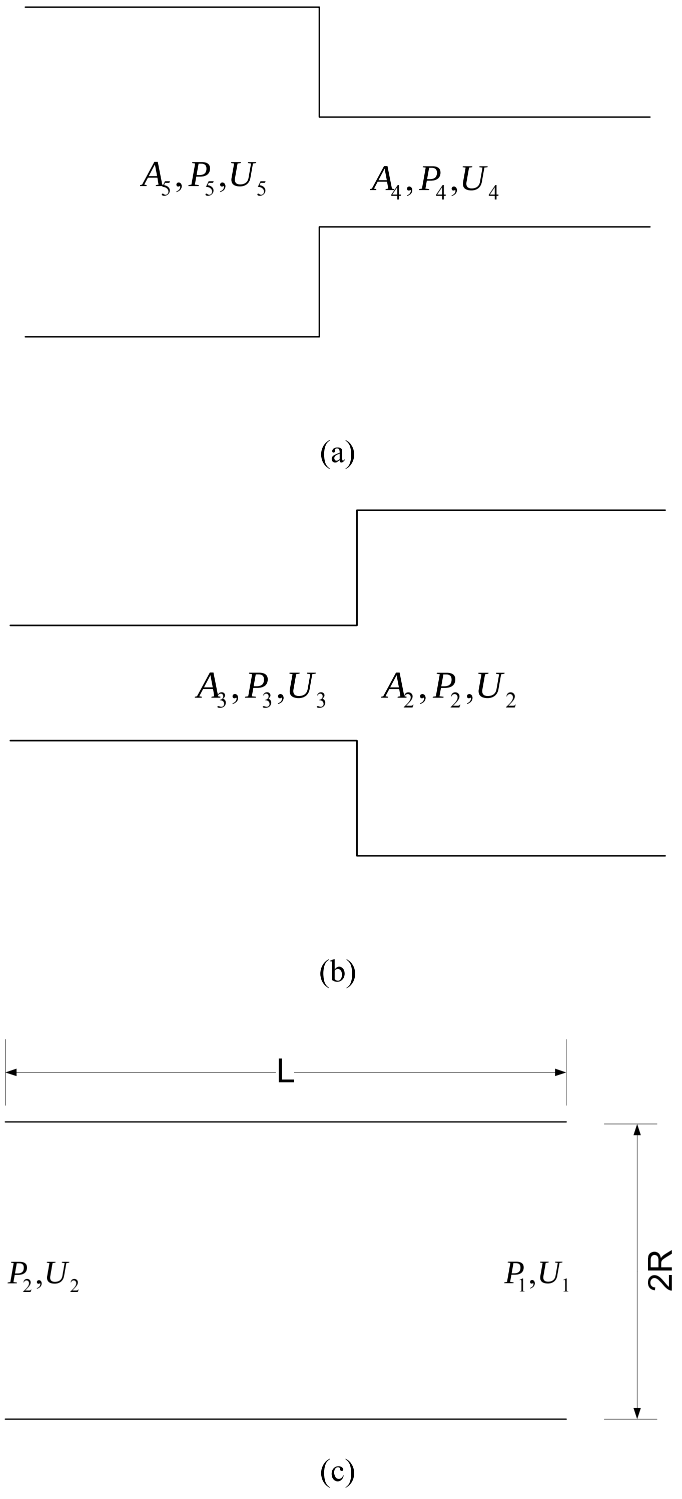

Figure C-1. (a) Schematic of an area contraction. (b) Schematic of an area expansion. (c) Schematic of an acoustic duct system.

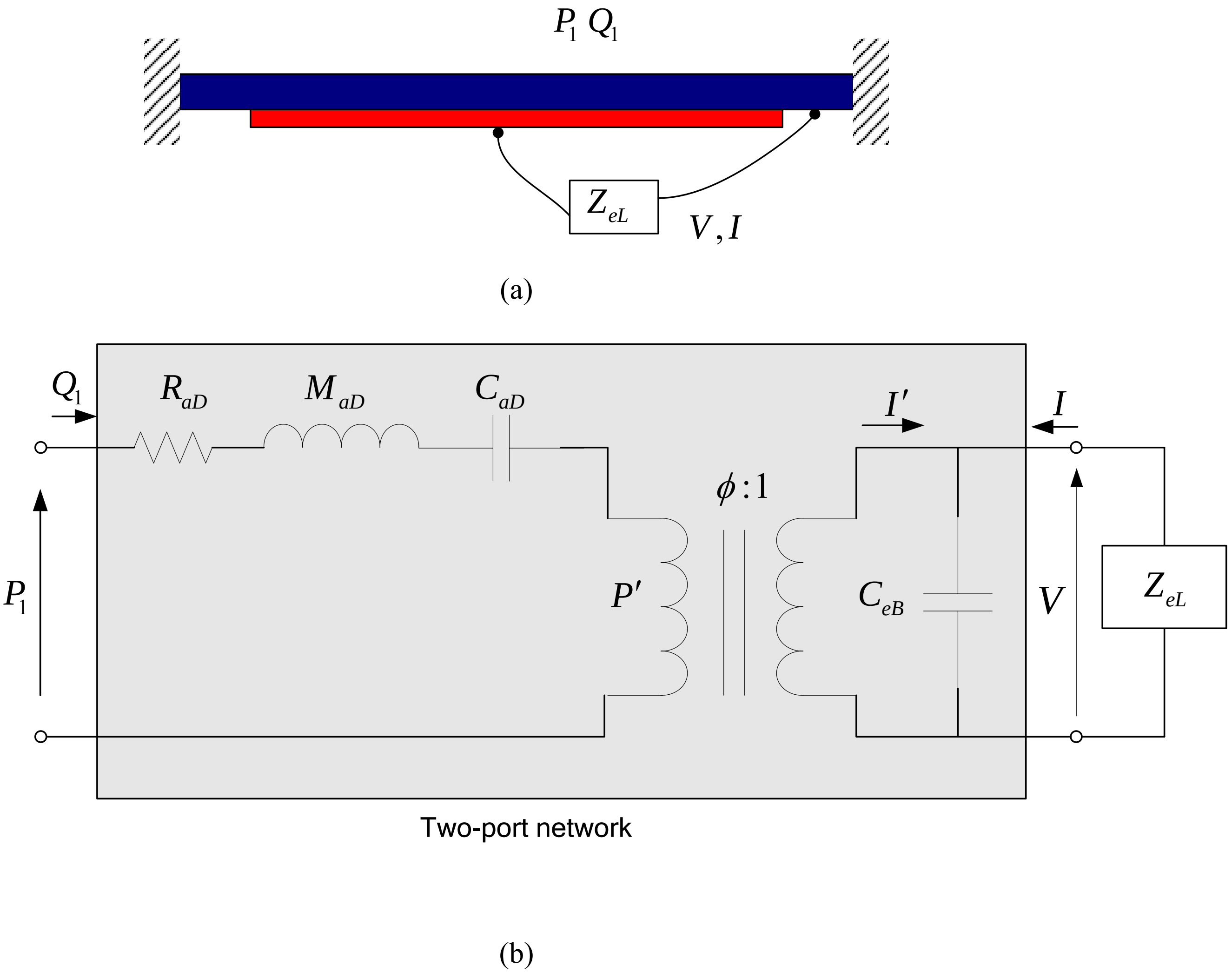

Figure C-2. (a) Schematic of a piezoelectric backplate with shunt loads. (b) The equivalent circuit representation for the piezoelectric backplate with the two-port network indicated.

Appendix D. Comparison Between TM and LEM

Equation Section (Next)

As discussed in Section 4, when the dimensions of the acoustic device are much smaller than the wavelength of interest, The device components can thus be lumped into idealized discrete circuit elements [16]. In comparison with the transfer matrix representation of the acoustic system, the LEM decouples the temporal and spatial variables associated the acoustic field, there is thus no spatial variation for a "lumped" element. Furthermore, the lumped element is two-pole system, while transfer matrix representation is four-pole network.

On the other hand, the LEM is occasionally no more than a reduced version of the transfer matrix representation when the quasi-state assumption is satisfied. For example, as shown in Figure D-1a, a duct with a sound-soft termination, it is assumed that no viscous loss is taken into account, thus from Eq.(C-21), one has

$$\frac{P_1}{Q_1} = \frac{j\rho_0 c_0 \tan kl}{S} \approx j\omega \frac{\rho_0 l}{S} \quad \text{as } kl << 1, \tag{D-1}$$

where $\rho_0 l/S$ is the lumped acoustic mass of the short tube. One more example, as shown in Figure D-1b, the duct is ended by a sound-hard termination, similarly, from Eq. (C-21), one has

$$\frac{P_1}{Q_1} = \frac{-j\rho_0 c_0 \cot kl}{S} \approx \frac{1}{j\omega \dfrac{\forall}{\rho_0 c_0^2}} \quad \text{as } kl << 1, \tag{D-2}$$

where $\forall = Sl$ is the volume of the tube, $\forall/\rho_0 c_0^2$ is the lumped acoustic compliance C_{aC}.

However, in most case, more assumptions should be satisfied for the LEM consistence with the transfer matrix representation. Shown in Figure D-1c, a duct terminated with a complex boundary Z_T, from Eq. (C-21), one has

$$\frac{P_1}{Q_1}=\frac{Z_T\cos kl+j\left(\rho_0c_0/S\right)\sin kl}{\left(j\sin kl\right)Z_T/\left(\rho_0c_0/S\right)+\cos kl}=\frac{\rho_0c_0Z_T\left(-j\cot kl\right)/S+\left(\rho_0c_0/S\right)^2}{Z_T+\rho_0c_0\left(-j\cot kl\right)/S}. \tag{D-3}$$

When $kl<<1$, Eq. (D-3) reduces to

$$\frac{P_1}{Q_1}=\frac{\rho_0c_0Z_T\left(-j\cot kl\right)/S+\left(\rho_0c_0/S\right)^2}{Z_T+\rho_0c_0\left(-j\cot kl\right)/S}\approx\frac{Z_T/(j\omega C_{aC})+\left(\rho_0c_0/S\right)^2}{Z_T+1/(j\omega C_{aC})}, \tag{D-4}$$

where $C_{aC}=\forall/\rho_0c_0^2$. Furthermore, when $Z_T/\left(j\omega C_{aC}\right)>>\left(\rho_0c_0/S\right)^2$, one has

$$\frac{P_1}{Q_1}\approx\frac{Z_T/(j\omega C_{aC})}{Z_T+1/(j\omega C_{aC})}, \tag{D-5}$$

which is the LEM of the system.

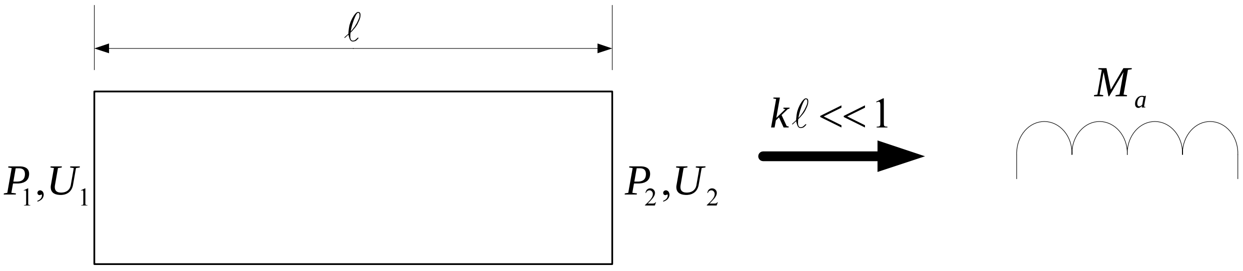

(a) $P_2/U_2 = 0$

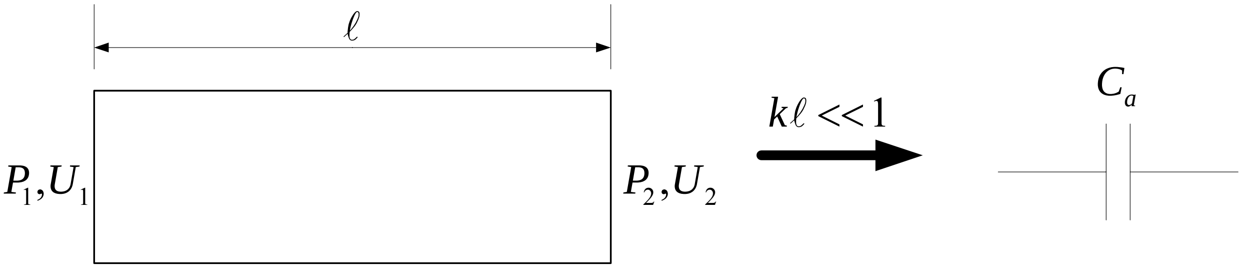

(b) $P_2/U_2 = \infty$

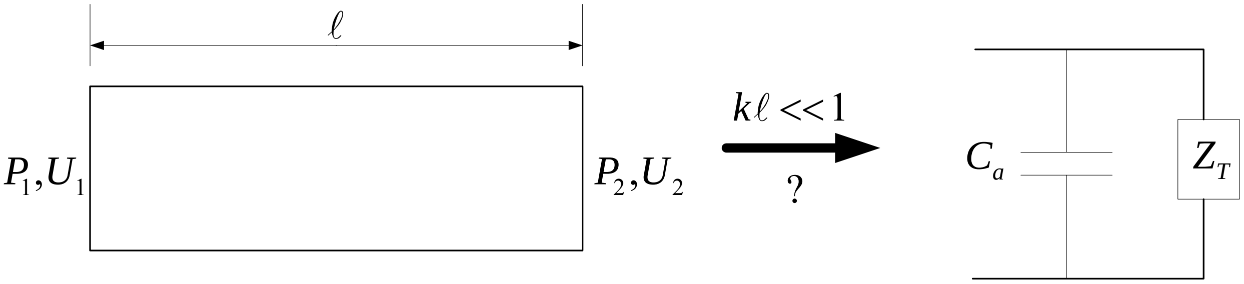

(c) $P_2/U_2 = Z_T$

Figure D-1. (a) Schematic of a duct terminated with sound-soft. (b) Schematic of a duct with sound-hard termination. (c) Schematic of a duct with complex termination

Appendix E. Summary On NASA 2DOF Liner Mimic

Equation Section (Next)

Introduction

The efforts have been made to mimic the second layer of the NASA 2DOF liner using the compliant diaphragm. The nominal specific acoustic impedance of the second layer of the NASA DDOF is shown in Figure E-1. Firstly, the mimic is performed using a clamped compliant diaphragm to match the target reactance. Proper materials are chosen accordingly. Second, a thin PVDF is attached to the compliant diaphragm. In comparison with PZT, PVDF is light-weighted and more flexible. A thin PVDF attached to the compliant diaphragm will not change it mimic behavior very much.

Lumped element modeling of a clamped compliant diaphragm

Unlike a rigid plate, the compliant diaphragm has finite acoustic compliance and mass. Next, the lumped element model of a clamped compliant diaphragm is briefly introduced.

Under a uniform pressure P, the deflection of a clamped compliant circular diaphragm with radius a and thickness h is given by

$$w(r) = w(0)\left(1-\left(\frac{r}{a}\right)^2\right)^2, \tag{E-1}$$

where $w(0)$ is the deflection of the center point of the compliant diaphragm and given by

$$w(0) = \frac{Pa^4}{64D}, \tag{E-2}$$

where D, the flexural rigidity, is defined by

$$D = \frac{Eh^3}{12\left(1-v^2\right)}, \tag{E-3}$$

where E is the elastic modulus, v is the Poisson's ratio.

It is assumed that the diaphragm is under the excitation of a harmonic signal

$$w(0,t) = w(0)e^{j\omega t} \tag{E-4}$$

the physically distributed compliant diaphragm can be lumped into equivalent mass and compliance at the center point as long as $kd \le 1$ and the excitation frequency is up to first resonant frequency of the diaphragm, where $k = \omega / c_0$ is the wave number and d is the diameter of the diaphragm. Firstly, the acoustic mass of the compliant diaphragm is determined via computing the kinetic co-energy. The incremental kinetic co-energy W_{KE^*} contained in a single ring of the transverse deflection is

$$dW_{kE^*} = \frac{1}{2}\underbrace{\left(\rho h 2\pi r dr\right)}_{\text{Mass}}\left[\underbrace{j\omega w(0)\left(1-\left(\frac{r}{a}\right)^2\right)^2}_{\text{Velocity}}\right]^2 . \qquad \text{(E-5)}$$

Thus, the total W_{KE^*} is

$$W_{KE^*} = \int_0^a dW_{KE^*} = \int_0^a \pi\rho h\left[j\omega w(0)\left(1-\left(\frac{r}{a}\right)^2\right)^2\right]^2 rdr , \qquad \text{(E-6)}$$

thus

$$W_{KE^*} = \frac{1}{2}\left[j\omega w(0)\right]^2 \rho h\left(\frac{\pi a^2}{5}\right) \qquad \text{(E-7)}$$

which must equal the lumped acoustic W_{KE^*}

$$\frac{1}{2}M_a Q^2 = W_{KE^*} = \frac{1}{2}\left[j\omega w(0)\right]^2 \rho h\left(\frac{\pi a^2}{5}\right), \qquad \text{(E-8)}$$

where M_a is acoustic mass, and Q is the volume velocity

$$Q = \int_0^a \left[j\omega w(0)\left(1-\left(\frac{r}{a}\right)^2\right)^2\right] 2\pi r dr = j\omega w(0)\left(\frac{\pi a^2}{3}\right). \qquad \text{(E-9)}$$

The acoustic mass is

$$M_a = \frac{9\rho h}{5\pi a^2} . \qquad \text{(E-10)}$$

The Eq. (E-9) also indicates that the effective area of the clamped diaphragm is

$$A_{eff} = \frac{1}{3}\pi a^2 . \qquad \text{(E-11)}$$

Then, the specific acoustic mass, M_a^s, is given by

$$M_a^s = M_a A_{eff} = \frac{3\rho h}{5}. \tag{E-12}$$

Next, the acoustic compliance is derived via lumping the total potential energy to the center point. Under the pressure P, the incremental potential energy, dW_{PE} is given by

$$dW_{PE} = PdAdw(r) = \underbrace{P(2\pi rdr)}_{\text{Force}}\underbrace{dw(r)}_{\text{Deflection}}. \tag{E-13}$$

Moreover, from Eq. (E-1)

$$dw(r) = \frac{\partial w(r)}{\partial w(0)}dw(0) = \left(1-\left(\frac{r}{a}\right)^2\right)^2 dw(0), \tag{E-14}$$

and from Eq. (E-2)

$$P = \frac{64Dw(0)}{a^4}. \tag{E-15}$$

So,

$$dW_{PE} = P2\pi rdrdw(r) = \frac{128\pi Dw(0)}{a^4}\left(1-\left(\frac{r}{a}\right)^2\right)^2 rdrdw(0), \tag{E-16}$$

and

$$W_{PE} = \int_0^q \int_0^{w(0)} \frac{128\pi Dw(0)}{a^4}\left(1-\left(\frac{r}{a}\right)^2\right)^2 rdrdw(0) = \frac{1}{2}\frac{64\pi D}{3a^2}\left[w(0)\right]^2, \tag{E-17}$$

which should equal the lumped acoustic potential energy

$$\frac{1}{2}\frac{1}{C_a}\forall^2 = W_{PE} = \frac{1}{2}\frac{64\pi D}{3a^2}\left[w(0)\right]^2, \tag{E-18}$$

where C_a is the acoustic compliance, and $\forall$ is the volume displacement

$$\forall = \int_0^q w(r)2\pi rdr = \int_0^a w(0)\left(1-\left(\frac{r}{a}\right)^2\right)^2 2\pi rdr = w(0)\left(\frac{\pi a^2}{3}\right). \tag{E-19}$$

Thus

$$C_a = \frac{\pi a^6}{192D}. \tag{E-20}$$

Then, the specific acoustic compliance is

$$C_a^s = \frac{C_a}{A_{eff}} = \frac{a^4}{64D} = \frac{3\left(1-v^2\right)a^4}{16Eh^3} \tag{E-21}$$

Eqs. (E-12) and (E-21) give the specific acoustic mass and compliance of the compliant diaphragm. Clearly, the specific acoustic mass is the function of the density and thickness of the diaphragm, while the specific acoustic compliance relates to the radius, thickness, elastic modulus and Poisson's ratio of the diaphragm.

Mimic the second layer of NASA 2DOF liner

To perform the mimic, a curve-fitting method is adopted to obtain set of the specific acoustic mass and compliance which satisfy the NASA 2DOF requirements. The curve-fitting function is set as

$$F_c = \left(j\omega M_a^s + \frac{1}{j\omega C_a^s} \right) \Big/ \left(\rho_0 c_0\right) \tag{E-22}$$

Then, adding ±10% tolerance to the target value of the curve fitting function (see Figure E-1), the curving fitting results (thus a mimic region) are obtained as shown in Figure E-2, and the range of the acoustic mass and compliance as shown in Figure E-3.

As mentioned above, the acoustic mass and compliance relate to the geometry and material properties of the diaphragm. Then, following the range of the specific acoustic mass and compliance, if the geometry parameters of the diaphragm are given, then the material properties can be determined. From Eq. (E-12),

$$\rho = \frac{5M_a^s}{3h}. \tag{E-23}$$

From Eq. (E-21),

$$E = \frac{3\left(1-v^2\right)a^4}{16h^3 C_a^s}. \tag{E-24}$$

Thus, if the range of the radius and thickness of the diaphragm are given by

$$0.04e-3 \le h \le 2e-3 \text{ [m]}, \tag{E-25}$$

and

$$2e-3 \le a \le 10e-3 \ [\text{m}], \tag{E-26}$$

The range of the density of the diaphragm is then obtained as shown in Figure E-4. Similarly, the range of the elastic modulus can also be obtained if the range of the radius and the thickness of the diaphragm are given. Then, when the range of the geometry parameters and material properties are obtained, the next step is to search materials for the diaphragm to satisfy the requirement.

Choice of the materials—Polymer

Following the guidelines set in section above, one possible polymer material is Polytheretherketone (PEEK). The PEEK has high temperature resistance, good resistance to wear, dynamic fatigue. The material properties of the PEEK are listed in Table E-1.

Table E-1. Material properties of the PEEK

Density Kg/m^3	Young's Modulus 10^9 N/m^2	Poisson's ratio
1260 - 1320	3.7 - 4	0.34

Firstly, the diaphragm is not attached with PVDF film. Then, following the range of the specific acoustic mass given in last section and Eq.(E-23), the thickness of the PEEK film is

$$0.1e-3 \le h \le 0.127e-3 \ [\text{m}]. \tag{E-27}$$

The thickness of the PEEK diaphragm is chosen as 0.125e-3 m due to the availability of the commercial product. Thus, from Eq. (E-23), one has

$$M_a^s = 0.0945 \tag{E-28}$$

with the range of the specific acoustic compliance is (shown in Figure E-3)

$$2.3e-7 \le C_a^s \le 2.9e-7\,. \tag{E-29}$$

The best mimic result happens at

$$C_a^s = 2.46e-7\,, \tag{E-30}$$

as shown in Figure E-5. From Eq. (E-21), the radius of the PEEK diaphragm is

$$a = 10.2e-3 \ [\text{m}] \tag{E-31}$$

Now assuming that the PEEK diaphragm is loaded by a uniformly distributed load of 200 N/m, the maximum stress is then given by

$$\left[\sigma_{\max}\right]_{\text{center}} = \frac{6}{h^2}\frac{200}{16}(1+\nu)a^2 = 6.69e5 \text{ [Pa]} \tag{E-32}$$

$$\left[\sigma_{\max}\right]_{\text{edge}} = \frac{6}{h^2}\frac{200}{8}a^2 = 9.99e5 \qquad \text{[Pa]} \tag{E-33}$$

which is much less than the tensile strength of the PEEK (70-100 MPa),

Next, a thin metalized PVDF is attached to the PEEK diaphragm, as shown in Figure E-6. The metalized PVDF film consists of PVDF metalized on both sides with aluminum. The thickness of the commercial metalized PVDF is 0.009e-3 m or 0.11e-3 m. Here, we choose the metalized PVDF film with the thickness of 0.009e-3 m. The material properties of the metalized PVDF are listed in Table 6. Because the density, Poisson's ratio and Young's modulus of the PVDF are similar to the PEEK, the thin PVDF film attached to the PEEK diaphragm doesn't change the mimic behavior very much. The mimic behavior of the PEEK diaphragm attached with thin PVDF film is shown in Figure E-7. The results show that one can mimic the acoustic behavior of the second layer of the NASA DDOF liner pretty well. However, further investigation find that the frequency shift between open-circuit and short-circuit of the PEEK-PVDF diaphragm is very small because the PVDF has relative weak electromechanical transduction in comparison with PZT material. Thus, work in the future will focus on the improvement of the frequency shift by increasing the thickness of the PVDF or adopting annular PVDF diaphragm (ring-like).

Choice of the materials—Metal

In comparison with Polymer materials, some light-weighted and flexible metals, such as Aluminum/Magnesium alloy, brass alloy and Titanium alloy, are more attractive in consideration of the operation temperature and fatigue. Section 6 presents the application of Titanium alloy to mimic the 2DOF liner. More metals will be taken into account in future.

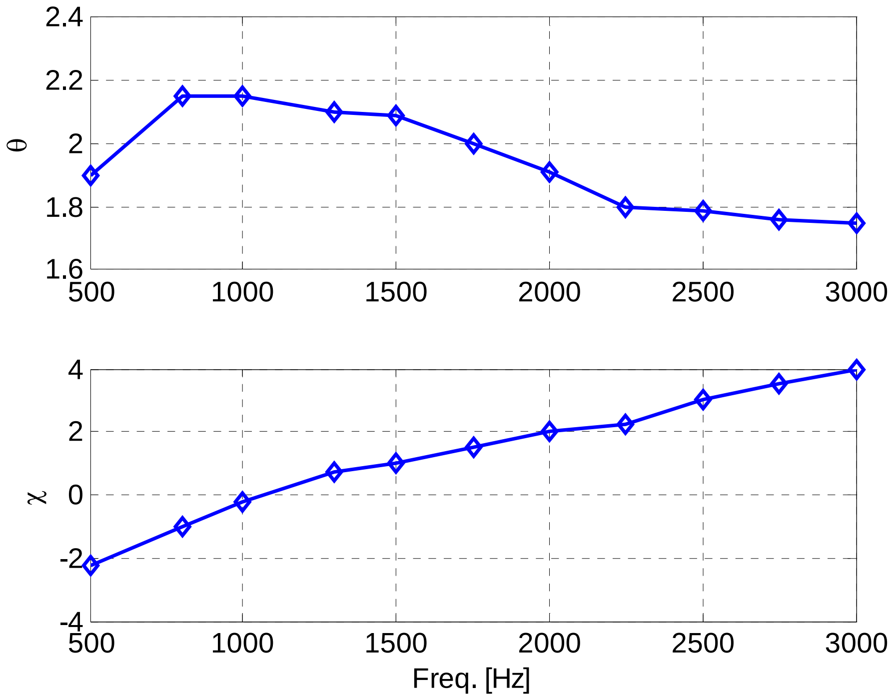

Figure E-1. Nominal specific acoustic impedance of NASA DDOF liner

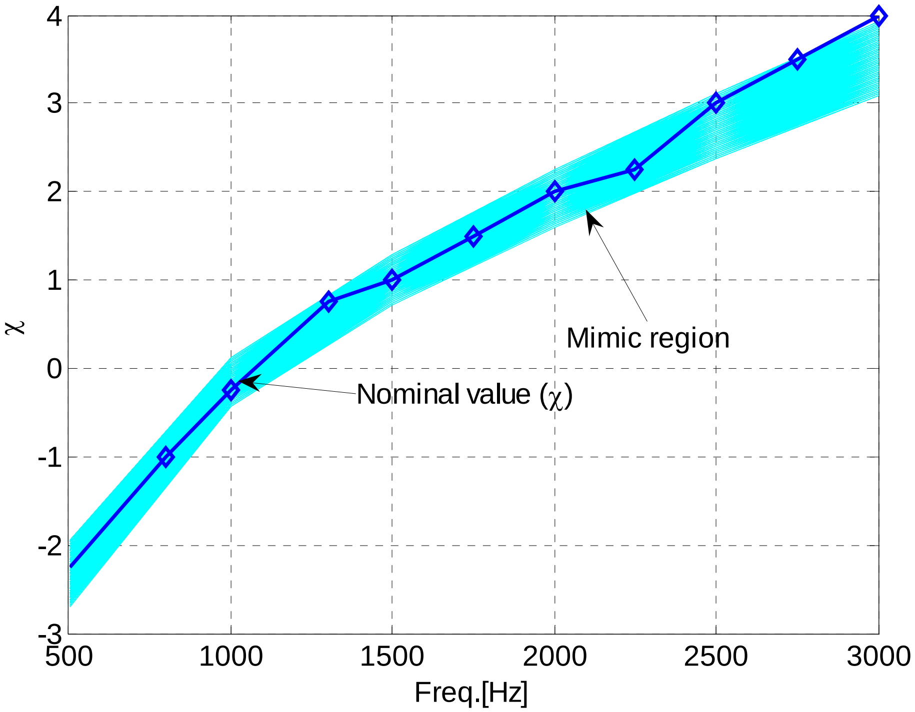

Figure E-2. Curve fitting (mimic region) for target acoustic reactance

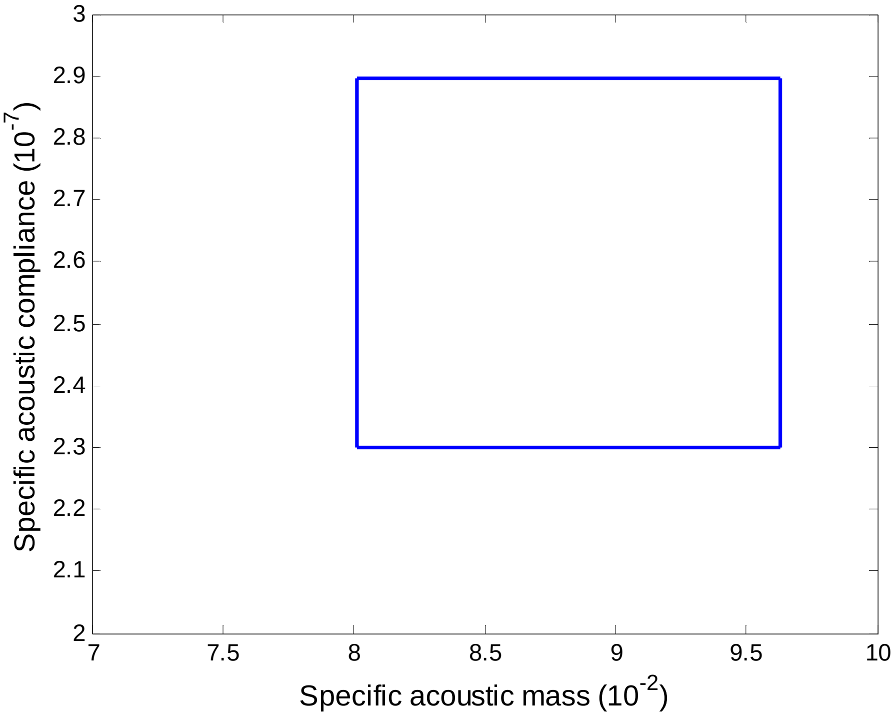

Figure E-3. Mimic range of the specific acoustic mass and compliance

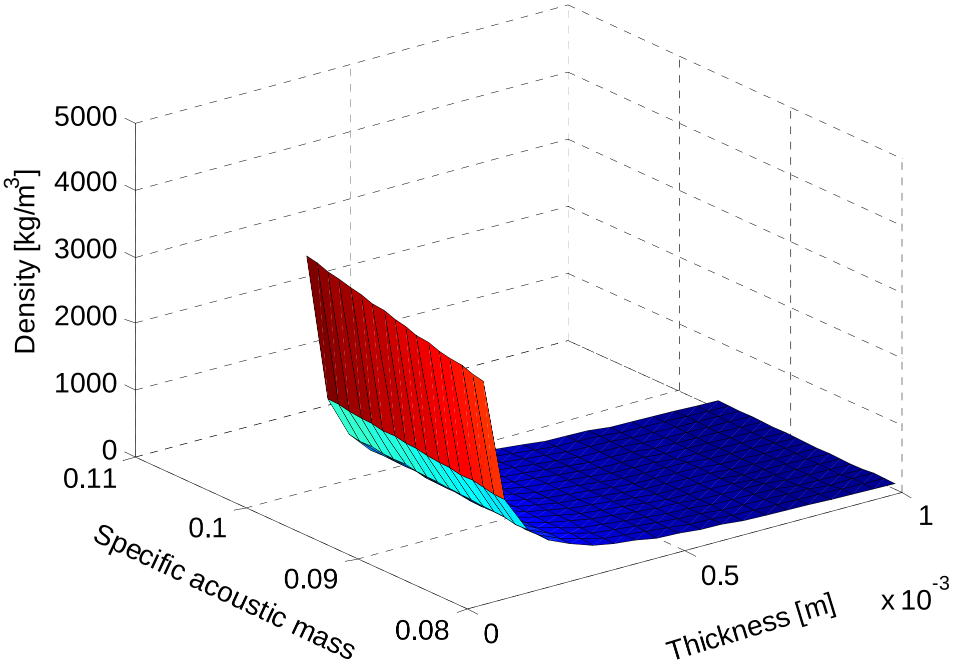

Figure E-4 Range of the density of the diaphragm corresponding to specific acoustic mass range and a given thickness range of the diaphragm.

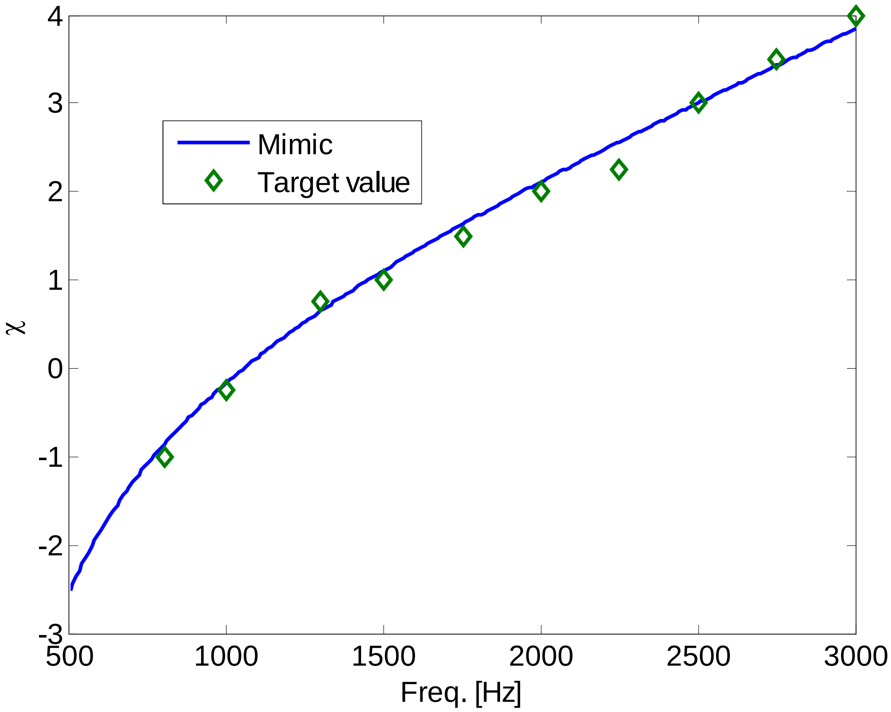

Figure E-5. Mimic behavior of the PEEK diaphragm

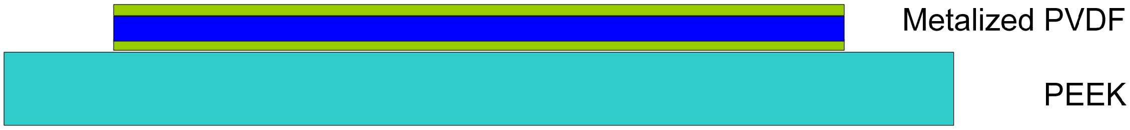

Figure E-6. Schematic of composite diaphragm

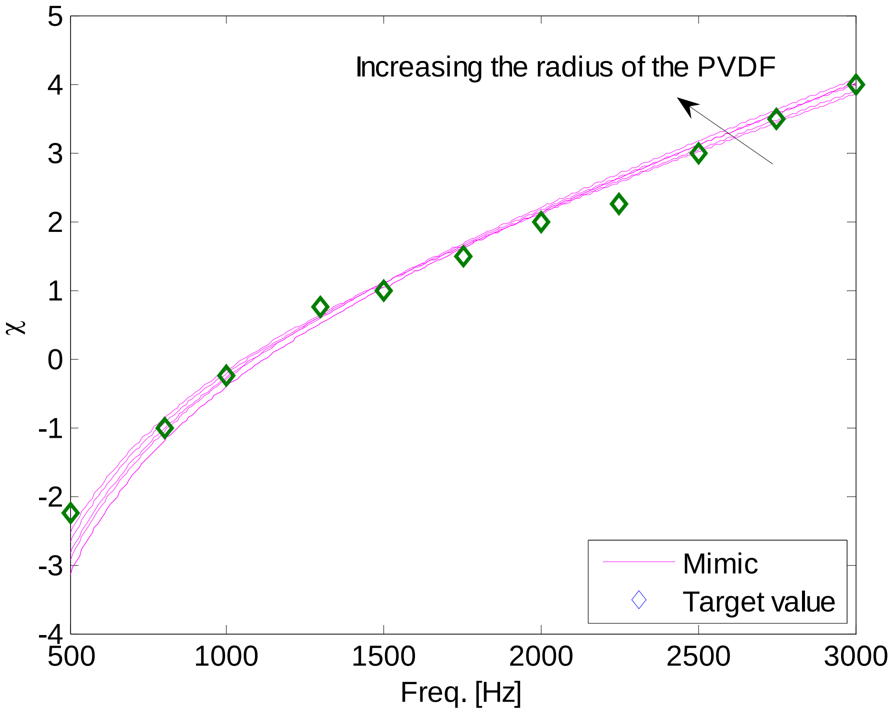

Figure E-7 Mimic behavior of the PEEK diaphragm attached with PVDF film

Appendix F. Impedance prediction code – ZKTL

This MATLAB code is rewritten based on NASA ZKTL Fortran code. The code was developed to calculate acoustic impedance for kinds of acoustic liners and the EMHR. The code consists of five subroutines listed below:

- Single channel impedance calculation (linear)—SCIC
- Single channel impedance calculation (nonlinear)—SCICNL
- Multi-channel, multi-segment, multi-layer impedance calculation (linear)—MCMSML
- Multi-channel, multi-segment, multi-layer impedance calculation (nonlinear)—MCMSMLNL
- EMHR

Main menu

Executing *zktl* on MATLAB command window results in:

```
Main Menu:
(1)Single Channel - Linear (SCIC)
(2) Single Channel - Nonlinear (SCICNL)
(3) Multi-Channel/Segment/Layer - Linear (MCMSML)
(4) Multi-Channel/Segment/Layer - Nonlinear (MCMSMLNL)
(5) EMHR – Electromechanical Helmholtz resonator
```

Entering selection (1-5) will choose related computing module for acoustic impedance calculation for acoustic liner / resonator. Each module has detailed help information.

SCIC routine

Choosing (1) on main menu will calculate single channel impedance linearly. In this routine, the acoustic impedance of a single channel is independent on the incident sound pressure level (SPL) and grazing flow speed. A single channel liner can consist of several layers. Each layer consists of one open channel, a perforated plate or foam. There are two kinds of geometry for one open channel--tube and split, shown in Figure F-1. The changes of diameter of the open channel from one layer to another layer are allowed if the channel is in the form of the tube. For perforated plate, it's assuming that the plate is infinitely thin. There are two types of input information to define the characteristics of the plate. These are:

- Flow resistance, in this case, the perforated plate only adds an acoustic resistance component to the acoustic impedance calculation.
- Pressure drop across the plate in the complex form, $dp(f) = A(f) + iB(f)$ where A and B are frequency dependent coefficients.

For a foam layer, the thickness and flow resistance should be included in the input parameters. The conclusion for input parameters for SCIC is shown in Figure F-2.

SCICNL routine

The option (2) in main menu is to nonlinearly compute the normalized acoustic impedance of a single channel liner. SCICNL takes account for the effect of SPL, grazing flow and bias flow on the acoustic impedance. In SCICNL routine, a single channel also consists of layer(s). Each layer has an open channel or perforated plate or both. The foam (layer) is not used in this case. The input information for SCICNL is almost the same as the SCIC, except for

- Grazing flow speed
- Bias flow speed
- Input file contains data to define frequency-dependent SPL
- Coefficients for the definition of changes of impedance across the perforated sheet during the nonlinear computing pass.

MCMSML routine

Choosing option (3) on main menu will execute MCMSML routine. MCMSML routine is used to calculate linearly the acoustic impedance of the liner which consists of numbers of channels, segments or layers, shown in Figure F-3. The liner can have a group of segments. It is assumed that all segments have the same span-wise width. Each segment consists of series of vertical elements. A single element includes open channel (s), perforated plate (s) or foam, as same as what described in SCIC routine. The element length distribution in each segment can be linear or on Quadratic residue series. The input logic for MCMSML is depicted in Figure F-4.

MCMSMLNL routine

The option (4) on main menu is to run MCMSMLNL module to computing acoustic impedance of multi-channels/segments/layers liner using nonlinear acoustic method. The liner geometry is the same as what is depicted in Figure F-4, except for that the foam (layer) is not used in this case. In addition to what are included in the input information for MSMSML, some extra input parameters are needed to define MSMSMLNL routine:

- Bias flow velocity
- Grazing flow velocity
- Input file which contains data to define frequency-dependent SPL
- Coefficients for the definition of changes of impedance across the perforated sheet during the nonlinear computing pass.

EMHR routine

Choosing option (5) on main menu will execute EMHR routine. The EMHR routine uses LEM or TM to predict the acoustic impedance of the EMHR. The input parameters include:

- Dimensions of the EMHR
- Material properties of the piezoelectric composite backplate

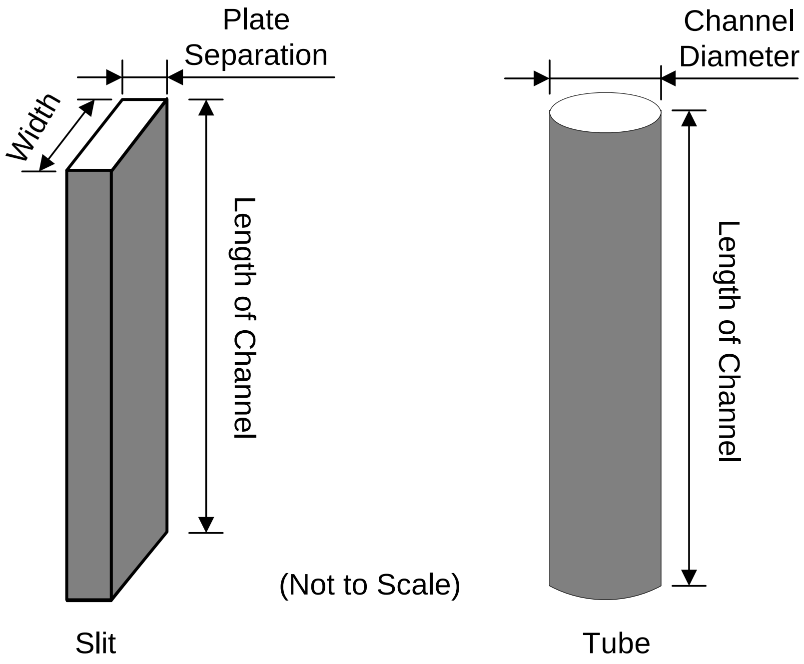

Figure F-1: Channel geometry for SCIC/SCICNL

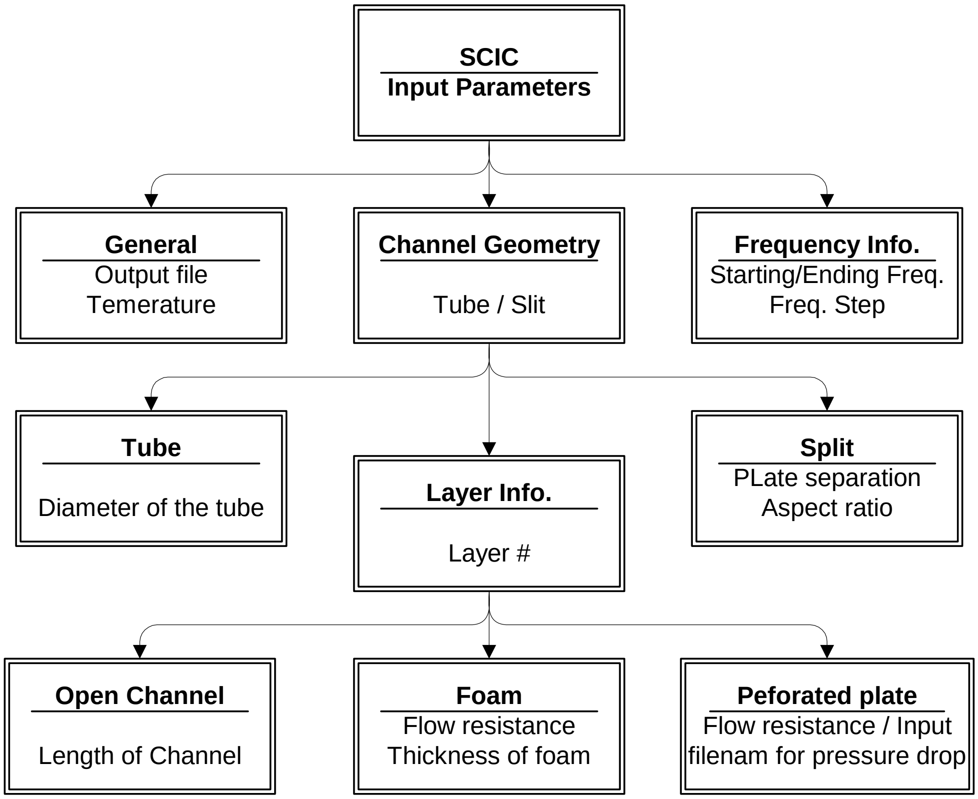

Figure F-2: Input parameters for SCIC

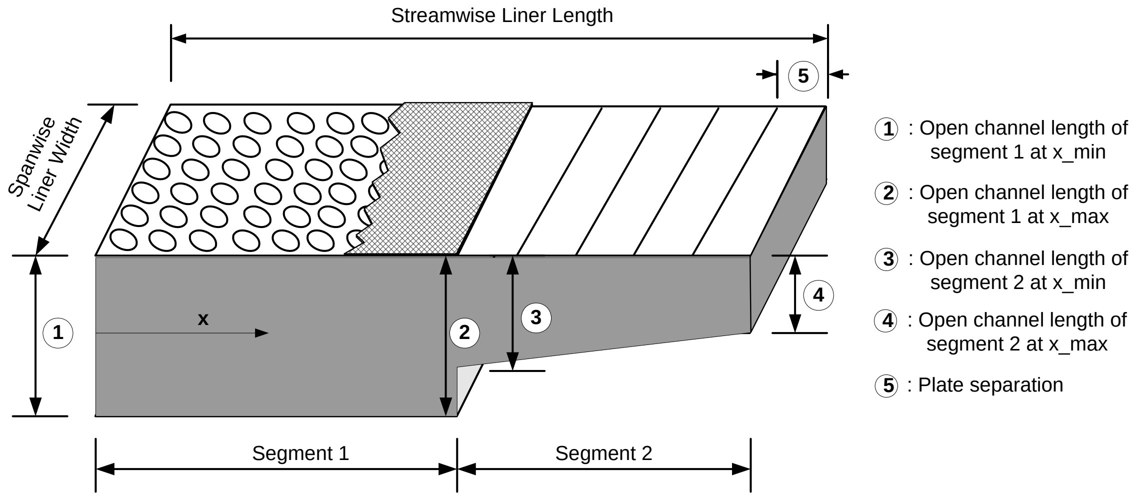

Figure F-3: Liner geometry for MCMSML/MCMSMLNL

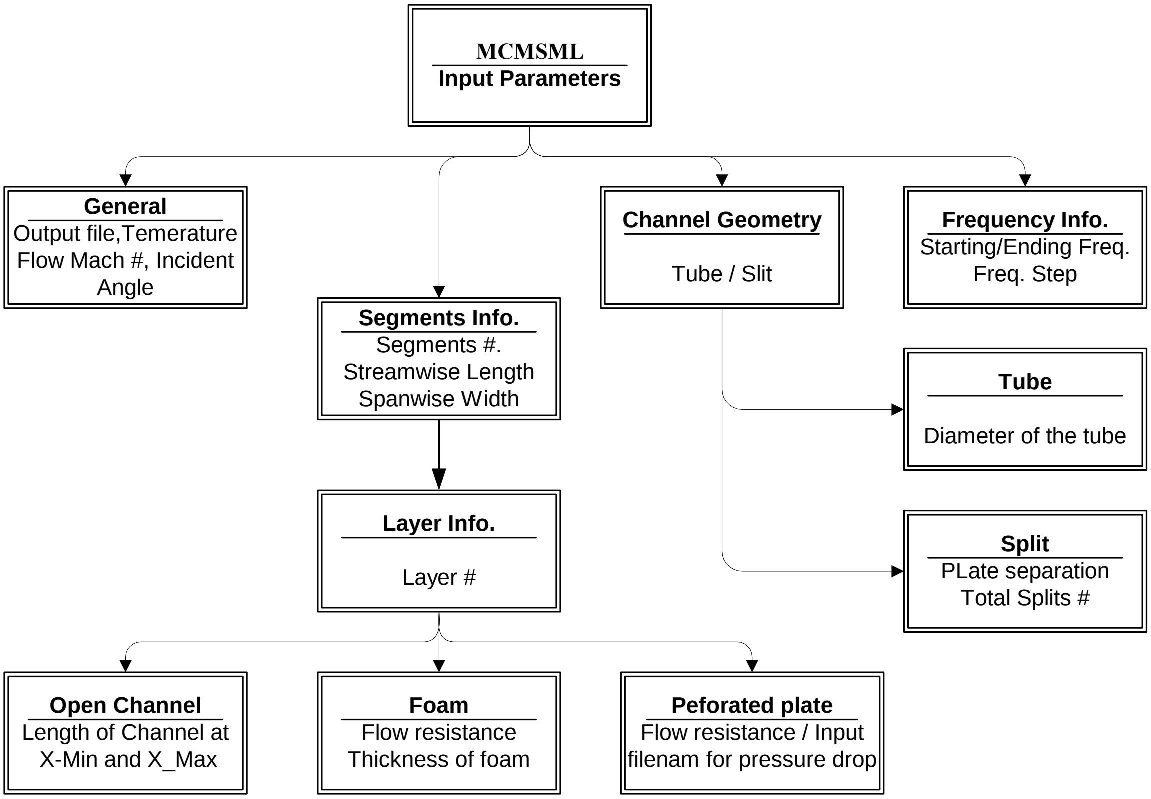

Figure F-4: Input logic for MCMSML